

**Investigation of Heterogeneously Catalyzed Reactions
using Molecular Beam Sampling Mass Spectrometry
with Threshold Ionization**

von Diplom - Chemiker
Raimund Horn
aus Schmalkalden

von der Fakultät II - Mathematik und Naturwissenschaften
der Technischen Universität Berlin
zur Erlangung des akademischen Grades

Doktor der Naturwissenschaften

- Dr. rer. nat. -

genehmigte Dissertation

Promotionsausschuß:

Vorsitzender: Prof. Dr. C. van Wüllen

Berichter: Prof. Dr. R. Schlögl

Berichter: Prof. Dr. R. Schomäcker

Tag der wissenschaftlichen Aussprache: 14. November 2003

Berlin 2003

D 83

to my parents

Science is a wonderful thing if one does not have to earn one's living at it. One should earn one's living by work of which one is sure one is capable. Only when we do not have to be accountable to anybody can we find joy in scientific endeavor.

Albert Einstein
(physicist, 1879-1955)

Kurzfassung

Ziel der vorliegenden Arbeit war es zu prüfen, ob sich die Molekularstrahl - Massenspektrometrie mit Bestimmung von Ionisations- und Aufttrittspotentialen eignet, in-situ die Gasphase über einem, unter realkatalytischen Bedingungen arbeitenden, Katalysator zu analysieren. Im Vordergrund stand der Nachweis reaktiver und daher kurzlebiger Gasphasenintermediate (z.B. Radikale) bei der Platin-katalysierten Bildung von Blausäure aus Methan und Ammoniak. Könnten solche Spezies nachgewiesen werden, wäre das ein Hinweis auf homogen ablaufende Reaktionsschritte in der Gasphase.

Dazu wurde ein Labormodell eines technischen Blausäurereaktors über ein Molekularstrahl - Interface an ein Quadrupol-Massenspektrometer gekoppelt, welches neben der massenspektrometrischen Analyse die Bestimmung von Ionisations- und Aufttrittspotentialen erlaubte. Der Reaktor bestand aus einem elektrisch beheizten, innen mit *Pt* beschichteten Keramikrohr und konnte unter Atmosphärendruck, Temperaturen bis 1300 °C und Flüssen bis 4000 ml · min⁻¹ betrieben werden. Er simulierte ein Einzelrohr des technischen Rohrbündelreaktors. Die Ankopplung an das im Hochvakuum arbeitende Massenspektrometer erfolgte über ein differentiell gepumptes Interface bestehend aus Düse, Skimmer und Kollimator. Die Probennahme mittels Molekularstrahl sollte reaktive Spezies einfrieren und einen schnellen und stoßfreien Transport in die Ionenquelle des Massenspektrometers gewährleisten. Neben der Blausäurebildung wurden mit dieser Anordnung weitere, in Bezug auf Gasphasenintermediate interessante, *Pt*-katalysierte Reaktionen untersucht. Das waren im Einzelnen die katalytische Methanverbrennung, die Ammoniakoxidation und die thermische Zersetzung von Ammoniak in die Elemente.

Zunächst wurde ein theoretisches Modell an die für Helium gemessene Ionisations-Effektivitätskurve angepaßt, um den mit den experimentell bestimmten Ionisations-

und Auftrittspotentialen verbundenen Fehler zu ermitteln. Dieser war mit 0.6 eV hinreichend klein, um alle erwarteten Intermediate eindeutig identifizieren zu können. Durch Messung der Ionisations-Effektivitätskurve auf der Massenzahl $m/z = 29\text{ amu}$ war es in der Tat möglich, Methylenimin ($\text{CH}_2=\text{NH}$) als Gasphasenintermediat bei der Bildung von Blausäure aus Methan und Ammoniak nachzuweisen. Die Identifizierung des Methylenimins erfolgte anhand seines, im Vergleich zu allen anderen überlagernden Molekülionen herausragend niedrigen Ionisationspotentials. Der experimentelle Nachweis dieses Moleküls bestätigt eine Vorhersage einer in der Literatur veröffentlichten theoretischen Arbeit, welche die Dehydrierung von Methylenimin zu Blausäure als homogenen Schlüsselschritt des Blausäurebildungsmechanismus postuliert.

Kurzlebige Intermediate wie z.B. Radikale wurden bei keiner der untersuchten Reaktionen gefunden. Die Nichtnachweisbarkeit dieser Spezies kann jedoch nicht als Beweis ihres Nichtvorhandenseins dienen, da die durchgeführten Experimente und eine eingehende Analyse des apparativen Aufbaus zeigten, dass der in-situ Charakter der Methode im Hinblick auf sehr kurzlebige Intermediate nicht gegeben war. Die Detektionsmethode an sich erwies sich zwar als geeignet, aber es gelang nicht, eine auch für sehr reaktive Moleküle repräsentative Probe der Reaktionszone zu erhalten. Im letzten Teil der Arbeit wird daher ein überarbeitetes Konzept vorgestellt, welches sich derzeit in der Realisierungsphase befindet. Der Neuaufbau übernimmt die massenspektrometrische Detektion, arbeitet aber mit einer verbesserten Probenahme. Die Gasmischung expandiert hierbei aus der Reaktionszone durch eine sich direkt in der katalytisch aktiven Wand befindende Düse in eine Niederdruckumgebung ('Fenn'-Typ Interface). Reaktive Spezies werden so unmittelbar eingefroren und die Zahl ihrer Stöße mit anderen Gasmolekülen und der Rohrwand minimiert.

Abstract

Goal of the present work was to verify if molecular beam sampling mass spectrometry with simultaneous determination of ionization- and appearance potentials can be used to study in-situ the gas phase above a catalyst, working under technical conditions. In the focus of interest was thereby the detection of reactive and consequently short-lived gas phase intermediates (e. g. radicals) in the platinum catalyzed formation of hydrocyanic acid from methane and ammonia. If such species were detected, it would be an indication of reaction steps proceeding homogeneously in the gas phase.

To reach this goal a molecular beam sampling interface has been used to connect a bench-scale model of the technical reactor with a quadrupole mass spectrometer, which allowed in addition to its normal operation the determination of ionization- and appearance potentials. The reactor consisted of an electrically heated ceramic tube, covered on the inside with platinum, and could be operated at atmospheric pressure, temperatures up to $1300\text{ }^{\circ}\text{C}$ and gas flows up to $4000\text{ ml}\cdot\text{min}^{-1}$. This configuration simulated a single tube of the technical tube bundle reactor. The connection to the mass spectrometer operating under high vacuum was accomplished by means of a differentially pumped interface consisting of nozzle, skimmer and collimator. The purpose of such a molecular beam sampling interface is to quench reactive species and to provide their collisionless transport to the ion source of the mass spectrometer. Not only the hydrocyanic acid formation but also other *Pt*-catalyzed reactions have been investigated with this setup. These were the catalytic combustion of methane, the ammonia oxidation and the ammonia decomposition into the elements.

First of all, a theoretical model has been fitted to the ionization efficiency curve of helium to determine the error connected with experimentally obtained ionization- and appearance potentials. The value of 0.6 eV was low enough to allow for unambiguous identification of all of the expected intermediates. Indeed, by measuring

the ionization-efficiency curve at the mass number $m/z = 29$ amu, it was possible to detect methylenimine ($CH_2=NH$) as gas phase intermediate in the hydrocyanic acid formation from methane and ammonia. Methylenimine was identified by its ionization potential which is lower than those of any of the interfering ions. The experimental proof of this intermediate confirms a prediction of a published theoretical work which postulated the dehydrogenation of methylenimine to hydrocyanic acid as a homogeneous key step in the reaction mechanism.

More short-lived intermediates such as radicals could not be detected in any of the investigated reactions. However, the non-detectability of these species can not prove their absence as the performed experiments and a careful investigation of the experimental setup revealed that the entire method could not be considered as in-situ with respect to real short-lived intermediates. Although the detection method proved suitable, it was not possible to draw a sample from the reaction zone that is representative even for very reactive molecules. For this reason, a revised experimental setup, which is currently under construction, is presented in the last part of this work. The new apparatus adopts the mass spectrometric detection but employs an improved sampling. Here, the gas mixture expands through a nozzle, which is integrated in the catalytically active wall, directly out of the reaction zone into a low pressure background ('Fenn'-type interface). Consequently, reactive intermediates are quenched instantaneously and the number of collisions that they perform with other gas molecules and with the tube wall is minimized.

Contents

List of Abbreviations	ix
List of Symbols	xi
List of Figures	xvii
List of Tables	xxi
1 Introduction	1
I Background	6
2 Chemical Background	7
2.1 The Concept of Heterogeneous Catalysis	8
2.2 Heterogeneous - Homogeneous Interactions	9
2.2.1 Energetical Coupling	9
2.2.2 Substantial Coupling	10
2.3 Investigated Reactions	13
2.3.1 Catalytic Combustion of Methane	13
2.3.2 Ammonia Oxidation	15
2.3.3 Ammonia Decomposition over Platinum	19
2.3.4 Hydrocyanic Acid from Methane and Ammonia	19

3	Physical Background	23
3.1	Molecular Beams	24
3.1.1	General Statements, Classification, Applications	24
3.1.2	Physical Characteristics of Supersonic Molecular Beams	26
3.2	Quadrupole Mass Spectrometry	32
3.2.1	Dynamic Sampling	33
3.2.2	Ion Generation	34
3.2.3	Mass Separation	37
3.2.4	Ion Detection	41
3.3	Threshold Ionization - Appearance Potential Measurements	43
3.3.1	Discrimination Principle - Ionization Potentials, Appearance Potentials	43
3.3.2	Ionization Efficiency Curves	45
3.3.3	Threshold Behavior - Predictions from Theory	46
3.3.4	Evaluation of Ionization Efficiency Data	52
3.3.5	Determination of the Electron Energy Spread Function	54
II	Experimental	63
4	Setup	64
4.1	Conception	64
4.2	Reactor	66
4.3	Interface	69
4.4	Mass Spectrometer	71

5 Experiments	72
5.1 Catalytic Combustion of Methane	72
5.1.1 Temperature Programmed Measurements	72
5.1.2 Mass Spectral Data	84
5.1.3 Appearance Potential Measurements	86
5.1.4 Conclusions	87
5.2 Ammonia Oxidation	89
5.2.1 Temperature Programmed Measurements	89
5.2.2 Mass Spectral Data	92
5.2.3 Conclusions	97
5.3 Ammonia Decomposition	98
5.3.1 Mass Spectral Data	98
5.3.2 Appearance Potential Measurements	100
5.3.3 Conclusions	100
5.4 Hydrocyanic Acid from Methane and Ammonia	103
5.4.1 Mass Spectral Data	103
5.4.2 Appearance Potential Measurements	107
5.4.3 Conclusions	110
6 Discussion and Assessment of the Method	112
III New Design	117
7 New Design	118
7.1 Reactor	118
7.2 Interface and Vacuum System	121

7.2.1	Interface	121
7.2.2	Vacuum System	122
7.3	Applications and Outlook	123
8	Summary	125
	Bibliography	129
	Acknowledgement	144
	Curriculum Vitae	146

List of Abbreviations

abbreviation	explanation
BMA	Blausäure aus Methan und Ammoniak
CVD	Chemical Vapor Deposition
CEM	Channel Electron Multiplier
DC	Direct Current
EPR	Electron Paramagnetic Resonance Spectroscopy
FFT	Fast Fourier Transformation
FTICR	Fourier Transform Ion Cyclotron Resonance
FWHM	Full Width at Half Maximum
GC	Gas Chromatography
IE	Ionization Efficiency
IR	Infrared Spectroscopy
LIFS	Laser Induced Fluorescence Spectroscopy
MFC	Mass Flow Controller
MIEPR	Matrix Isolation Electron Paramagnetic Resonance
MS	Mass Spectrometer, Mass Spectrometry
NMR	Nuclear Magnetic Resonance Spectroscopy
PEP	Positron Emission Profiling
(E)PIC	(Energy) Pulse Ion Counting
QMF	Quadrupol Mass Filter
RF	Radio Frequency
SEM	Secondary Electron Multiplier
SFG	Sum Frequency Generation Spectroscopy
TAP	Temporal Analysis of Products

UHV	Ultra High Vacuum
UV	Ultra Violet
UV/ Vis	Ultra Violet / Visible Spectroscopy
XAS	X-Ray Absorption Spectroscopy
XRD	X-Ray Diffraction

List of Symbols

fundamental constants

symbol	explanation	numerical value
amu	atomic mass unit	$1.66056 \cdot 10^{-27} \text{ kg}$
e	elementary charge	$1.60219 \cdot 10^{-19} \text{ C}$
h	Planck's constant	$6.62618 \cdot 10^{-34} \text{ J s}$
k	Boltzmann's constant	$1.38066 \cdot 10^{-23} \text{ J} \cdot \text{K}^{-1}$
N_A	Avogadro's number	$6.02214 \cdot 10^{23} \text{ mol}^{-1}$
R	universal gas constant	$8.31451 \text{ J} \cdot \text{mol}^{-1} \cdot \text{K}^{-1}$

mathematical notation

notation meaning

∇	Nabla operator
div	divergence of a vector field
\vec{X}, \vec{x}	vectors
$\frac{\partial}{\partial x}, \frac{\partial}{\partial y}, \frac{\partial}{\partial z}$	partial derivatives
dx	differential increment of x
Δx	increment of x
$f(x, y, \dots)$	function of x, y, \dots
x, y, z	directions in space (Cartesian coordinates)

common subscripts and superscripts

symbol	explanation	type
cc	indicates parameter in the collimator chamber	subscript
g	gas phase	subscript
max	maximum value	subscript

min	minimum value	subscript
nc	indicates parameter in the nozzle chamber	subscript
r	reaction	subscript
ref	MFC reference temperature (273.15 K)	subscript
s	surface	subscript
sc	indicates parameter in the skimmer chamber	subscript
x, y, z	indicate the direction in space	subscript
0	indicates stagnation parameters	subscript
*	critical value	superscript
\ominus	standard state (for gases $p = 101325 Pa, T = 298.15 K$)	superscript

specific symbols

symbol	explanation	unit	(equation)/[figure]/{table}
a	constant in the QMF -field equation	$[a] = V \cdot m^{-2}$	(3.25), (3.26), (3.28), (3.29)
a_μ, a	parameter in the Mathieu equation, $\mu = x$ or y	$[a_\mu] = [a] = 1$	(3.41), (3.43), (3.45), (3.46), [3.10]
A	area	$[A] = m^2$	(3.5)-(3.7), (3.9), (5.4)-(5.6), [3.2]
A	SEM amplification	$[A] = 1$	(3.47)
AP	appearance potential	$[AP] = eV$	(3.49), (3.50), (3.75), [5.27], {5.5}, {5.7}
b	constant in the QMF -field equation	$[b] = V \cdot m^{-2}$	(3.26), (3.28), (3.30)
C	constant of proportionality	$[C] = cps \cdot eV^{-\mu}$	(3.63), (3.68), (3.70)-(3.74), [3.17], [3.18], [3.19]
C_{2n}	function in the solution of the Mathieu equation	$[C_{2n}] = 1$	(3.44)
d_n	nozzle diameter	$[d_n] = m$	(3.1), (3.3), (3.21), (5.7), (6.5), (7.2), (7.4), [3.3]
d_r	reactor tube diameter	$[d_r] = m$	(6.1), (6.2), (6.4)
e^-	indicates an electron		(3.48), (3.49), (3.51), (3.52),

			(3.55)-(3.58), (3.60), (5.9), [3.6]
E	electric field strength	$[E] = V \cdot m^{-1}$	(3.24), (3.34)-(3.36)
E	energy	$[E] = eV$	(3.61)
E	total electron energy	$[E] = eV$	(3.48), (3.49), (3.51)-(3.53), (3.59), (3.62)-(3.64), (3.68)-(3.72), (3.74)
E_a	activation energy	$[E_a] = kJ \cdot mol^{-1}$	(2.1), [2.2]
E_{kin}	kinetic energy	$[E_{kin}] = eV$	(3.20), (3.22)
F	force	$[F] = N$	(3.7), (3.8), (3.24)
F_l	force on dV from the left	$[F_l] = N$	(3.5), (3.7)
F_r	force on dV from the right	$[F_r] = N$	(3.6), (3.7)
i	ion current	$[i] = counts \cdot s^{-1}$ $= cps$	(3.63), (3.68), (3.70)-(3.74), [3.14], [3.15], [3.16]
IP	ionization potential	$[IP] = eV$	(3.48), (3.50), (3.53), (3.59), (3.63), (3.64), (3.68), (3.70)-(3.75), [3.14]-[3.19], [5.27]
k	reaction rate konstant	$[k] = (l/mol)^{\nu-1} s^{-1}$	(2.1), (3.61)
k_0	preexponential factor	$[k_0] = (l/mol)^{\nu-1} s^{-1}$	(2.1)
K	equilibrium constant	$[K] = 1$	(2.44)
Kn	Knudsen number	$[Kn] = 1$	(3.1), (3.3), (3.4), {3.1}
l	length	$[l] = m$	(6.1), (6.2), (6.4)
\bar{l}	mean free path	$[\bar{l}] = m$	(3.1), (3.3)
m	ion mass	$[m] = amu$	(3.37), (3.38), (3.41), (3.42), (3.46), [3.10], {5.5}, {5.7}
m	mass	$[m] = kg$	(3.8)
$m(U) =$	electron energy	$[m(U) = m(E - V)]$	(3.63), (3.65)-(3.74)
$m(E-V)$	spread function	$= eV^{-1}$	
M	molar mass	$[M] = g \cdot mol^{-1}$	(3.13), (3.14), (3.16), (3.17), (5.6), (5.7), (6.2), (6.4), (7.4)
MN	Mach number	$[MN] = 1$	[3.4]

N	number of oscillators in the ion	$[N] = 1$	(3.61)
N_{cd}	number of conversion electrons	$[N_{cd}] = 1$	(3.47)
N_d	number of dynode electrons	$[N_d] = 1$	(3.47)
N_m	number of binary collisions	$[N_m] = 1$	(6.2), (6.3)
N_w	number of wall collisions	$[N_w] = 1$	(6.4)
n	particle density	$[n] = m^{-3}$	[3.3]
n	number of SEM dynodes	$[n] = 1$	(3.47)
p	pressure	$[p] = Pa$	(2.44), (3.2), (3.5)-(3.7), (3.9)-(3.13), (3.15)-(3.18), (3.21), (5.2), (5.5)-(5.7), (5.10), (5.11), (6.2), (6.5), (7.2)-(7.4), [3.1], [3.4], [4.7]
P_d	probability of dissociation	$[P_d] = 1$	(3.49), (3.52), (3.63)
P_i	probability of ionization	$[P_i] = 1$	(3.48), (3.51), (3.63), (3.64), (3.68), (3.70), (3.74)
q_m	mass flow through the nozzle	$[q_m] = kg \cdot s^{-1}$	(5.4)-(5.7)
q_μ, q	parameter in the Mathieu equation, $\mu = x$ or y	$[q_\mu] = [q] = 1$	(3.42), (3.43), (3.45), (3.46), [3.10]
Q	nozzle gas discharge	$[Q] = Pa \cdot m^3 \cdot s^{-1}$	(7.3)-(7.5)
$Q_i^{+(\mu+)}$	total cross section for single (μ -fold) ionization	$[Q_i^{+(\mu+)}] = m^2$	(3.53), (3.59)
r	resolution of the QMF	$[r] = 1$	(3.46), [3.10]
r_0	half distance between the quadrupole rods	$[r_0] = m$	(3.29)-(3.31), (3.33)-(3.35), (3.37), (3.38), [3.8]
s	path	$[s] = m$	(3.6)-(3.9), [3.2]
s	slope of the mass scan line	$[s] = 1$	(3.45)
S	pumpage	$[S] = m^3 \cdot s^{-1}$	(7.3), (7.5)
t	time	$[t] = s$	(3.8), (3.32)-(3.35), (3.37)-(3.40)
T	temperature	$[T] = K$	(2.1), (2.44), (3.2), (3.13) (3.14), (3.16), (3.17), (3.65), (5.6), (5.7), (5.11), (6.1), (6.2), (6.4), (7.4), [3.3],

			[3.4], [5.8], [5.11], [5.12], [5.18]-[5.27]
U	potential difference (voltage)	$[U] = V$	(3.22)
U	DC voltage applied to the quadrupole rods	$[U] = V$	(3.32)-(3.35), (3.37), (3.38), (3.41), (3.45)
U	thermal electron energy	$[U] = eV$	(3.62), (3.65)-(3.67)
v	velocity	$[v] = m \cdot s^{-1}$	(3.8)-(3.11), (3.13), (3.14), (3.19), (5.4), (5.5), [3.2], [3.3]
v_{sd}	speed of sound	$[v_{sd}] = m \cdot s^{-1}$	(3.15), (3.16)
V	volume	$[V] = m^3$	(6.1), [3.2]
\dot{V}	volume flow rate	$[\dot{V}] = m^3 \cdot s^{-1}$	(6.1), (6.2), (6.4), [5.11]-[5.16], [5.18]-[5.27]
V	RF voltage applied to the quadrupole rods	$[V] = V$	(3.32)-(3.35), (3.37), (3.38), (3.42), (3.45)
V	electron energy obtained by electric field acceleration	$[V] = eV$	(3.62), (3.63), (3.68)-(3.74), [3.14]-[3.16]
x	number of C -atoms in C_xH_y	$[x] = 1$	(2.24)
x	distance to nozzle	$[x] = m$	[3.3]
x	mole fraction	$[x] = 1$	(5.10), [5.11]-[5.15], [5.18]-[5.27]
x_M	distance nozzle - Mach disk	$[x_M] = m$	(3.21), (6.5), (7.1), (7.2)
x_s	distance nozzle - skimmer	$[x_s] = m$	(7.1)
y	number of H -atoms in C_xH_y	$[y] = 1$	(2.24)
z	ion charge	$[z] = 1$	(3.54), {5.5}, {5.7}
α', α'', β	functions in the solution of the Mathieu equation	$[\alpha'] = [\alpha''] = m$ $[\beta] = 1$	(3.44)
γ	parameter in the Mathieu equation, $\gamma = \sigma$ or λ	$[\gamma] = m^{-2}$	(3.41), (3.42)
κ	adiabatic exponent	$[\kappa] = 1$	(3.12)-(3.18), (5.6), (5.7), (5.10), (5.11), (7.4)
λ	constant in the QMF -field equation	$[\lambda] = m^{-2}$	(3.31)

μ	placeholder in the Mathieu equation, $\mu = x$ or y	$[\mu] = 1$	(3.43), (3.44)
μ	exponent in the ionization threshold law	$[\mu] = 1$	(3.53), (3.54), (3.59)
ν	sum of the stoichiometric coefficients of the reaction	$[\nu] = 1$	for the definition of k and k_0
ν	frequency	$[\nu] = s^{-1}$	(3.55), (3.61)
ν	collision frequency	$[\nu] = s^{-1}$	[3.3]
ξ	variable in the Mathieu equation	$[\xi] = 1$	(3.40), (3.43), (3.44)
ρ	density	$[\rho] = kg \cdot m^{-3}$	(3.9)-(3.12), (3.15), (5.4)
σ	collision cross section	$[\sigma] = m^{-2}$	(3.2), (6.2)
σ	constant in the QMF -field equation	$[\sigma] = m^{-2}$	(3.31)
σ	standard deviation	$[\sigma] = eV$	(3.31), (3.66), (3.74)-(3.76), [3.17], [3.18], [3.19]
ω	angular frequency of the RF -voltage	$[\omega] = s^{-1}$	(3.32)-(3.35), (3.37), (3.38), (3.40)-(3.42)
$\Delta_d H$	dissociation enthalpy	$[\Delta_d H] = eV$	(3.50)
$\Delta_r H$	heat of reaction	$[\Delta_r H] = kJ \cdot mol^{-1}$	(2.2)-(2.4), (2.25), (2.41)-(2.44), (2.74)-(2.76), (5.1), (5.12)-(5.16), [2.2]
τ	residence time	$[\tau] = s$	(6.1)
$\phi_{(mod)}$	(modified) equivalence ratio	$[\phi_{(mod)}] = 1$	(5.2), (5.3)
Φ	electric potential in-between the quadrupole rods	$[\Phi] = V$	(3.23)-(3.31), (3.33)-(3.36)
Φ_0	electric potential applied to the quadrupole rods	$[\Phi_0] = V$	(3.29)-(3.32), [3.8]
\square	oxide ion vacancy		(2.13), (2.14)

List of Figures

2.1	Elementary steps in heterogeneous catalysis	8
2.2	Potential-energy curves of homogeneous- and heterogeneous elementary reactions	8
2.3	Operation and pollutants production in conventional- and catalytic combustion	13
2.4	BMA -mechanism based on Pfeil et al.	22
2.5	BMA -mechanism based on Diefenbach et al.	22
3.1	Generation of supersonic molecular beams	26
3.2	Flow field model for a one-dimensional expansion	27
3.3	Centerline properties of a free jet expansion	30
3.4	Structure of a free jet expansion	31
3.5	Dynamic sampling of chemical reactions	34
3.6	Ion source of the HAL4 EPIC Low Energy	35
3.7	Electrodes of the HAL4 EPIC Low Energy	35
3.8	Ideal quadrupole electrode structure	37
3.9	Potential field of an ideal quadrupole	38
3.10	Stability diagram of a QMF	40
3.11	Faraday Cup as ion detector	42

3.12	SEM as ion detector	42
3.13	IE-curves of CH_4	45
3.14	Morrison's differential method for a linear threshold law	57
3.15	Morrison's differential method for Wannier's nonlinear threshold law	57
3.16	Morrison's differential method applied to IE-curves of He and Ar	58
3.17	Determination of the parameters of the spread function for helium	60
3.18	Determination of the parameters of the spread function for argon	60
3.19	Correlation of the fit parameters in Equation (3.74)	61
4.1	Schematic diagram of the experimental setup	64
4.2	Picture of the experimental setup	65
4.3	Arrangement of reaction tube and heater in the reactor	67
4.4	Drawing of the high temperature reactor	67
4.5	Arrangement for temperature profile measurements	68
4.6	Temperature profile of the reactor at 600 W heating power	69
4.7	Molecular beam sampling interface	70
5.1	Location of the thermocouple in the reactor	73
5.2	Catalytic combustion of methane: CO_2 evolution during the temperature programmed experiment (He corrected signal intensities)	74
5.3	Catalytic combustion of methane: temperature curve of the temperature programmed experiment	74
5.4	Catalytic combustion of methane: temperature programmed experiment, mass spectra in the parametric sensitive region around 434 °C	76
5.5	Catalytic combustion of methane: temperature programmed experiment, peak area vs. temperature curve for the internal standard He at $m/z = 4 amu$	78

5.6	Catalytic combustion of methane: temperature programmed experiment, peak area vs. temperature curves for CH_4 , O_2 , H_2O and CO_2 (uncorrected signal intensities)	78
5.7	Catalytic combustion of methane: temperature programmed experiment, peak area vs. temperature curves for CH_4 , O_2 , H_2O and CO_2 (He corrected signal intensities)	79
5.8	Catalytic combustion of methane: signal intensities of He , H_2O and CO_2 during the temperature programmed experiment	82
5.9	Catalytic combustion of methane: temperature programmed experiment, mass spectra around 37 amu before and after the upward jump in conversion	82
5.10	Catalytic combustion of methane: high sensitivity mass spectrum from $50 - 500\text{ amu}$ immediately after the upward jump in conversion	83
5.11	Catalytic combustion of methane: $\dot{V} = 300\text{ ml} \cdot \text{min}^{-1}$, $x_{CH_4} = 0.50$, $x_{O_2} = 0.13$, $x_{He} = 0.37$, $T_{reactor} = 438\text{ }^\circ\text{C}$, mass spectrum $0.40 - 50.00\text{ amu}$	86
5.12	Catalytic combustion of methane: $\dot{V} = 3000\text{ ml} \cdot \text{min}^{-1}$, $x_{CH_4} = 0.50$, $x_{O_2} = 0.13$, $x_{He} = 0.37$, $T_{reactor} = 450\text{ }^\circ\text{C}$, IE -curves at 15 and 17 amu	88
5.13	Ammonia oxidation: $\dot{V} = 500\text{ ml} \cdot \text{min}^{-1}$, $x_{NH_3} = 0.51$, $x_{O_2} = 0.39$, $x_{Ar} = 0.10$, N_2 evolution during the temperature programmed experiment (Ar corrected signal intensities)	90
5.14	Ammonia oxidation: $\dot{V} = 500\text{ ml} \cdot \text{min}^{-1}$, $x_{NH_3} = 0.51$, $x_{O_2} = 0.39$, $x_{Ar} = 0.10$, programmed and measured temperature curve	90
5.15	Ammonia oxidation: $\dot{V} = 500\text{ ml} \cdot \text{min}^{-1}$, $x_{NH_3} = 0.51$, $x_{O_2} = 0.39$, $x_{Ar} = 0.10$, temperature programmed experiment, mass spectra in the parametric sensitive region around $240\text{ }^\circ\text{C}$	91
5.16	Ammonia oxidation: temperature programmed experiments for $\dot{V} = 1000, 2000, 3000$ and $4000\text{ ml} \cdot \text{min}^{-1}$	92
5.17	Ammonia oxidation: experimental design for $NH_3/O_2/Ar$ mixtures	93

5.18	Ammonia oxidation: screening for intermediates, $\dot{V} = 500 \text{ ml} \cdot \text{min}^{-1}$, $T_{\text{reactor}} = 300 \text{ }^\circ\text{C}$, $x_{\text{NH}_3} = 0.45$, $x_{\text{O}_2} = 0.45$, $x_{\text{Ar}} = 0.10$	94
5.19	Ammonia oxidation: screening for intermediates, $\dot{V} = 2000 \text{ ml} \cdot \text{min}^{-1}$, $T_{\text{reactor}} = 300 \text{ }^\circ\text{C}$, $x_{\text{NH}_3} = 0.45$, $x_{\text{O}_2} = 0.45$, $x_{\text{Ar}} = 0.10$	94
5.20	Ammonia oxidation: screening for intermediates, $\dot{V} = 500 \text{ ml} \cdot \text{min}^{-1}$, $T_{\text{reactor}} = 1300 \text{ }^\circ\text{C}$, $x_{\text{NH}_3} = 0.45$, $x_{\text{O}_2} = 0.45$, $x_{\text{Ar}} = 0.10$	95
5.21	Ammonia oxidation: screening for intermediates, $\dot{V} = 2000 \text{ ml} \cdot \text{min}^{-1}$, $T_{\text{reactor}} = 1300 \text{ }^\circ\text{C}$, $x_{\text{NH}_3} = 0.45$, $x_{\text{O}_2} = 0.45$, $x_{\text{Ar}} = 0.10$	95
5.22	Ammonia decomposition: $\dot{V} = 500 \text{ ml} \cdot \text{min}^{-1}$, $x_{\text{NH}_3} = 0.80$, $x_{\text{Ar}} =$ 0.20 , mass spectra for $T_{\text{reactor}} = 20, 650$ and $1300 \text{ }^\circ\text{C}$	99
5.23	Ammonia decomposition: $\dot{V} = 500 \text{ ml} \cdot \text{min}^{-1}$, $x_{\text{NH}_3} = 0.80$, $x_{\text{Ar}} =$ 0.20 , IE -curves at 16, 15 and 14 <i>amu</i> , $T_{\text{reactor}} = 20, 650$ and $1300 \text{ }^\circ\text{C}$.	101
5.24	BMA-reaction: $\dot{V} = 500 \text{ ml} \cdot \text{min}^{-1}$, $x_{\text{NH}_3} = 0.60$, $x_{\text{CH}_4} = 0.30$, $x_{\text{He}} =$ 0.10 , mass spectrum for $T_{\text{reactor}} = 1300 \text{ }^\circ\text{C}$	106
5.25	BMA-reaction: $\dot{V} = 500 \text{ ml} \cdot \text{min}^{-1}$, $x_{\text{NH}_3} = 0.60$, $x_{\text{CH}_4} = 0.30$, $x_{\text{He}} =$ 0.10 , $T_{\text{reactor}} = 1300 \text{ }^\circ\text{C}$, high sensitivity mass spectrum from 30 – 100 <i>amu</i> , comparison with a literature spectrum of acetonitrile	107
5.26	BMA-reaction: $\dot{V} = 500 \text{ ml} \cdot \text{min}^{-1}$, $x_{\text{NH}_3} = 0.60$, $x_{\text{CH}_4} = 0.30$, $x_{\text{He}} =$ 0.10 , $T_{\text{reactor}} = 1300 \text{ }^\circ\text{C}$, IE -curves at 15, 16, 26, 27, 28, 29, 30, 41 and 44 <i>amu</i>	108
5.27	BMA-reaction: $\dot{V} = 500 \text{ ml} \cdot \text{min}^{-1}$, $x_{\text{NH}_3} = 0.60$, $x_{\text{CH}_4} = 0.30$, $x_{\text{He}} =$ 0.10 , $T_{\text{reactor}} = 1300 \text{ }^\circ\text{C}$, IE -curve at 29 <i>amu</i>	110
6.1	Sampling of the tubular reactor by means of an external nozzle	113
7.1	Sampling of the tubular reactor by means of an internal nozzle	118
7.2	New design: reactor - three-dimensional cut view	120
7.3	New design: reactor - enlarged nozzle section	120
7.4	New design: core features - vacuum system and interface	124

List of Tables

3.1	Gas flow regimes	25
4.1	Gases used for the experiments	66
5.1	Peak assignment table to Figure 5.11	85
5.2	Assignment of the measured threshold values from Figure 5.12	88
5.3	Peak assignment table to the Figures 5.18 - 5.21	96
5.4	Peak assignment table to Figure 5.22	99
5.5	Assignment of the measured threshold values from Figure 5.23	101
5.6	Assignment table to Figure 5.24	105
5.7	Assignment of the measured threshold values from Figure 5.26	109

Chapter 1

Introduction

Heterogeneously catalyzed reactions are of paramount importance for mankind. Fuels, fertilizers, pharmaceuticals, polymers, coatings, in fact all performance products that our modern life is based on, are made using a few basic substances. These chemicals like for instance sulfuric acid, ammonia, nitric acid, methanol etc. are produced in enormous amounts taking advantage of heterogeneous catalysis [1, 2, 3, 4]. Sulfuric acid as an example has a production capacity of more than 135 million t/a [1]. Beside producing chemicals, heterogeneous catalysis is also very important for supplying fuels to ensure the energy production for industry, traffic and households [5]. Closely related to this field are environmental issues to control and minimize emissions of mobile and stationary sources [6]. Most of the applied reactions are known for decades and technically implemented in a very sophisticated way. But for all that, the reaction mechanisms of the majority of them are still subject of speculation.

The only way to obtain absolutely unbiased information about a real catalytic system would be to study it without any perturbation. Metaphorically speaking that would mean to elucidate the reaction mechanism just by having a look at the industrial reactor. This, as a matter of fact impossible approach would be perfectly ‘**in-situ**’. Any experimental method, independent of its underlying principle, disturbs the system under investigation to a certain extent and supplies more or less biased information with respect to the undisturbed case.

The traditional way to get insight into heterogeneous catalysis as surface phenomenon is to apply surface science techniques [7, 8] to model and real catalytic systems. This approach has been very successful and contributed in an excellent

manner to numerous questions, last but not least because of the unambiguous character of the obtained data. A serious drawback is the constriction of many surface science techniques to **UHV**-conditions and well defined samples leading to the frequently complained pressure- or material gap respectively. On the in-situ scale, these methods are far away from the ideal point and it is debated to which extent the results can be transferred to the technical process.

In consequence of these difficulties a more recent trend has been developed in catalysis research, namely to study the catalytic systems under conditions as close to the industrial application as possible. Methods allowing this are commonly referred to as ‘**in-situ**’-methods, notwithstanding the philosophical considerations above.

A rigorous classification of the multitude of these techniques and their modifications is difficult. A rough classification might be obtained by dividing them into spectroscopic and non-spectroscopic techniques. Spectroscopic techniques are in widespread use and scan a part of the electromagnetic spectrum to obtain information about the sample [9]. They will be considered in more detail in the following paragraphs. Less common but at least as meaningful are time-resolved and position-resolved techniques like for example **TAP** (**T**emporal **A**nalysis of **P**roducts) [10] and **PEP** (**P**ositron **E**mission **P**rofilng) [11].

If one takes for example heterogeneously catalyzed gas reactions, the catalytic system comprises here the catalyst and the surrounding gas phase. Most researchers focus on the in-situ investigation of bulk and surface properties of the catalyst including chemical composition, phase transitions, surface rearrangements, adsorbed reactants, intermediates, products and spectator species. Methods like **XRD** [12, 13], **XAS** [14], Mössbauer-spectroscopy [15], **IR** [16, 17], **NMR** [17], **EPR** [17], **UV/Vis** [17], Raman-spectroscopy [18], **SFG** (**S**um **F**requency **G**eneration) [19] etc. are well established for that purpose.

Compared to the innumerable number of papers focussing on bulk and surface studies, gas phase contributions to the mechanism of a heterogeneously catalyzed reaction are usually neglected. This might be even warrantable in many cases as homogeneous reactions are mostly unselective and are tried to be suppressed by using an appropriate catalyst performing the reaction under mild and selective conditions. However, there are numerous examples of reactions where homogeneous steps play a

remarkable role in the overall mechanism [20, 21, 22, 23, 24].

Also this work was motivated by the question about the role of surface-generated gas phase intermediates in heterogeneous catalysis. The goal was to adapt a method which allows an ‘in situ’ investigation of the gas phase above a working catalyst surface. In the focus of interest was the platinum catalyzed formation of hydrocyanic acid from methane and ammonia but also other platinum catalyzed reactions like the catalytic combustion of methane, the ammonia oxidation and the ammonia decomposition have been investigated. As will be discussed in more detail in Section 2.3, all of these technically important reactions are promising to be studied, as they are speculated to involve a variety of gas-phase intermediates in their mechanisms. Among the postulated species are radicals like $H\cdot$, $\cdot O\cdot$, $OH\cdot$, $HO_2\cdot$, $CH_3\cdot$, $CH_3OO\cdot$, $NH_2\cdot$, $\cdot NH\cdot$, $N\cdot$ but also non-radicals like $HCHO$, CH_3OH , H_2O_2 , HNO , NH_2OH , HNO_2 , HNO_3 , N_2H_2 , CH_2NH .

The task to probe the gas phase above a working catalyst surface with respect to transient species is in principle not new and has been tackled severalfold in former times using suitable spectroscopic techniques [22, 25, 26, 27, 28, 29]. Especially surface-generated gas phase radicals were found to be important intermediates during heterogeneous catalytic reactions [30]. It stands to reason that such highly reactive molecules are preferably studied at low pressure conditions and indeed, nearly all of the investigations found in the literature were performed at pressures below 1 *Torr*. Moreover, most of the reactors used comply rather with the analytical method than with the technical process. As this is in disagreement with the in-situ idea, the present work aimed to study the hydrocyanic acid formation under technical operating conditions (1013 *mbar*, 1300 °C) using a bench-scale model of the industrial reactor. The other reactions were studied using the same setup. Two fundamental problems are inherent in this intention. Firstly one needs an analytical method which allows the specific detection of low concentrations of intermediates in presence of high concentrations of interfering compounds and secondly one needs a sample which is representative for the chemical composition of the reaction zone.

The choice of the method was stimulated by experiences from the literature. According to the expectations, it should allow the detection of both radical and non-radical species, but due to the explorative stage of the project, with a moderate instrumental expenditure. Essentially three spectroscopic techniques are published

to be applicable for the detection of gas phase radicals in heterogeneous catalysis. Well known from flame- and plasma investigations, **L**aser **I**nduced **F**luorescence **S**pectroscopy (**LIFS**) is a prominent technique for the qualitative and quantitative detection of radicals like for example $OH\cdot$, $\cdot NH$ or $NH_2\cdot$ even under ambient pressure conditions [31]. The identification is based on the specific fluorescence of the molecules from an excited electronic state after absorbing a laser photon matching the transition frequency [26, 32]. As a consequence thereof the nature of the radical of interest must be known beforehand or an expensive tunable dye laser is needed to scan the entire spectrum. Even in the latter case important species like $H\cdot$ or $\cdot O$ can not be measured as their first absorption transitions lie far in the vacuum **UV**. Other radicals like for instance $CH_3\cdot$ elude a detection too, as they do not fluoresce. Even though **LIFS** could in principle be used to detect intermediates independent if radical or non-radical, it is here not applicable as a pool of species come into question. Non-fluorescent species would be missed and the probing of all the others would require a disproportionate experimental effort.

Applicable to all kinds of radicals is the **M**atrix **I**solation **E**lectron **P**aramagnetic **R**esonance (**MIEPR**) technique. Paramagnetic radicals are trapped here downstream of a reactor on a cold finger in a solid matrix, usually argon at about 12 K. After a defined collection time, the cold finger is transferred into a microwave cavity of a conventional **EPR** spectrometer and the spectrum is recorded [22]. This laborious procedure prevents continuous working, requires an elaborate and expensive instrumentation and is restricted to paramagnetic species. The big advantage of the technique is, that it is easy to quantify as it counts the absolute number of spins. It was for example successfully applied to reveal the role of surface generated gas phase radicals in the oxidative coupling of methane to higher hydrocarbons [33]. Nevertheless, also this method is not suited for our purpose as it would fail to detect potential diamagnetic intermediates.

A much more versatile method frequently applied to detect free radicals is mass spectrometry. The stimulation to its use has been twofold [34]. Firstly, there is a fundamental aspect for the study of structures and energetics of radicals [35] and secondly an analytical aspect for the study of species emanating from plasmas [36], flames [37] or chemical reactions [38]. The discrimination between radical ions and corresponding fragments of heavier molecules is based upon the difference in their

ionization- and appearance potentials respectively [34]. The first experiments have been conducted using classical electron impact ionization. This method is experimentally straightforward but thermally generated low energy electrons bring along a considerable energy spread. Hence, the approach proved only successful for species having a difference between their ionization- and appearance potentials larger than the energy spread of the ion source [39]. A better solution is to use monochromatized electrons [40, 41] or, if procurable, photoionization [39]. This in turn requires much more instrumentation than a commercially available mass spectrometer equipped with a conventional electron impact ion source. However, taking all ionization methods together, a wide variety of both organic and inorganic radicals have been studied to date sometimes under perspective of the fundamental and sometimes of the analytical focus [42]. Mass spectrometry with threshold ionization was also selected for this work as it offers the possibility to detect both, radical and non-radical species either by means of the threshold ionization technique or just by analysis of the mass spectrum. Conventional electron impact ionization was sufficient here, as all expected species have ionization potentials considerably lower than the appearance potentials of the corresponding fragment ions. As a mass spectrometer can only be operated in high vacuum a molecular beam sampling interface was used to draw a sample from the catalytic reactor. Molecular beam sampling offers the advantage that the beam constituents are quenched immediately preventing reactive species from further reactions.

The work is divided into three parts. Part I is a disquisition on the chemical and the physical background of this work (Chapter 2 and 3). The chemical background comprises the principle of heterogeneous catalysis (Section 2.1), possible surface - gas phase interactions (Section 2.2) and a brief introduction of the investigated reactions (Section 2.3). To introduce to the sampling and detection method, the physical background summarizes important features of the molecular beam interface (Section 3.1) and the mass spectrometer (Section 3.2) and describes fundamentals of the threshold ionization technique (Section 3.3). Part II is devoted to the experimental setup (Chapter 4), presents the results obtained for the four investigated reactions (Chapter 5) and a conclusive assessment of the method in reference to the background part (Chapter 6). Part III is essentially an outlook and describes the design of a second generation experimental setup which shall be realized in the near future.

Part I

Background

Chapter 2

Chemical Background

The emphasis of this work was on the development of an in-situ mass spectrometric method to study the gas phase chemistry during heterogeneously catalyzed reactions. The focus of interest was thereby on the investigation of the oxygen free formation of hydrocyanic acid from methane and ammonia (German: **B**lausäure aus **M**ethan und **A**mmoniak, **BMA**-process) with respect to potential gas phase intermediates. According to the technical process, a catalytic tubular wall reactor was used, consisting of an externally heated sintered corundum pipe covered inside with a thin layer of platinum as catalyst. Before studying the *HCN* formation, it was necessary to investigate test reactions that are known for involving gas phase chemistry and use CH_4 and NH_3 as reactants and *Pt* as catalyst. Two prominent exothermic examples namely the catalytic combustion of methane and the ammonia oxidation were found to fulfill these requirements. Both reactions are mechanistically well studied and numerous intermediates have been proposed and experimentally verified. The third reaction carried out was the platinum catalyzed decomposition of ammonia into the elements to build a bridge from the highly exothermic oxidation reactions to the highly endothermic hydrocyanic acid formation. The intent of this chapter is to present exemplarily the interplay between catalyst and gas phase and to introduce the investigated reactions with respect to the knowledge about their mechanisms.

2.1 The Concept of Heterogeneous Catalysis

The behavior of a chemical system that is not in equilibrium is the result of its thermodynamics and kinetics. A mixture of hydrogen and oxygen can be stored in a vessel for hundred years without any change although the reaction to water is thermodynamically favored. However, insertion of only a trace of platinum serving as a catalyst would cause a vigorous explosion. This example illustrates the principle of catalysis as a kinetic phenomenon. Figure 2.1 shows in a schematic way the different steps taking place on a catalytic active surface:

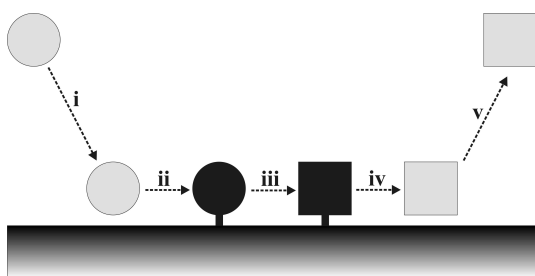


Figure 2.1: *Elementary steps in heterogeneous catalysis: i) educt diffusion to the surface ii) adsorption iii) chemical transformation iv) desorption v) product diffusion from the surface*

If one follows now the chemical transformation step along a selected reaction coordinate one obtains a potential energy-curve qualitatively reproduced in Figure 2.2 :

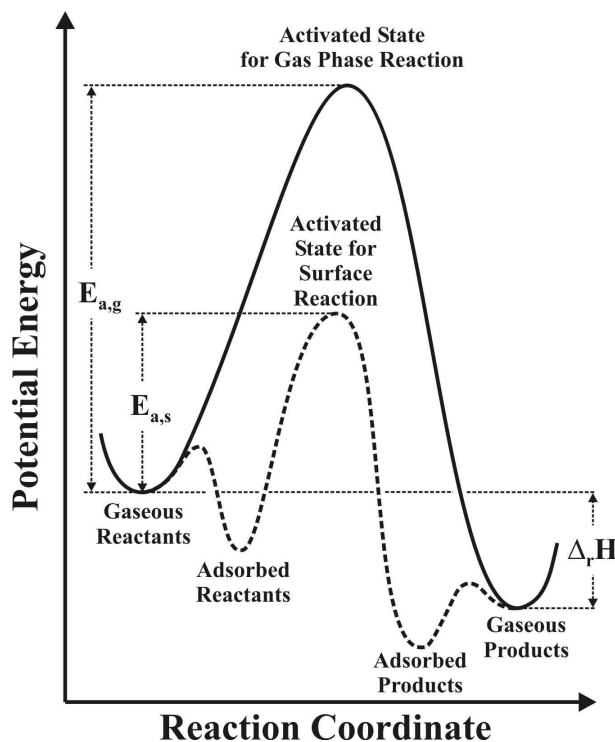


Figure 2.2: *Potential-energy curves for a reaction proceeding homogeneously in the gas phase (full curve, index g) and heterogeneously on the surface (dotted curve, index s)*

As indicated by $\Delta_r H$, there is no difference between the thermodynamics of the homogeneous reaction in the gas phase and the same reaction proceeding heterogeneously on the catalyst surface. According to the temperature dependence of the rate constant [2.1], the same reaction rate might be attained heterogeneously catalyzed at much lower temperature than in the corresponding homogeneous reaction.

$$k = k_0 e^{-\frac{E_a}{RT}} \quad (2.1)$$

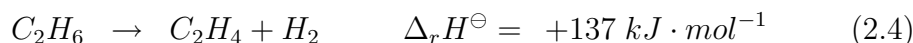
This makes catalyzed reactions superior with respect to selectivity, economy and environmental friendliness.

2.2 Heterogeneous - Homogeneous Interactions

Heterogeneously catalyzed reactions are often insufficiently described by surface reaction steps only. There can be a distinct coupling between heterogenous and homogeneous steps as outlined in the following:

2.2.1 Energetical Coupling

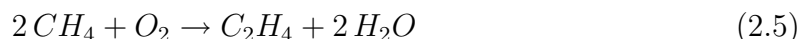
Energetical coupling emerges from exothermic surface reactions and is frequently observed in partial oxidations. If the heat of reaction can not be dissipated properly, the resulting temperature increase can be high enough to open up desired or undesired heterogeneous and homogeneous reaction pathways. In the most inauspicious case, the homogeneous reactions are in turn exothermic, leading at the worst to flames and explosions [43]. An example for a desired homogeneous contribution is the oxidative dehydrogenation of ethane to ethene over *Pt*. The dehydrogenation itself proceeds in the gas phase using heat originating from surface oxidation of a fraction of ethene to CO_x [44].



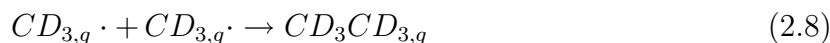
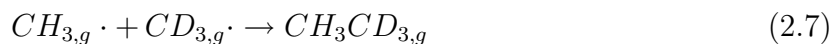
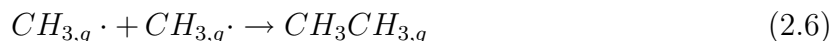
The homogeneous dehydrogenation is appreciated here, because ethene that is formed on the *Pt*-surface can not desorb fast enough and is further dehydrogenated to completely stripped *C*-atoms which are then immediately oxidized to CO_x .

2.2.2 Substantial Coupling

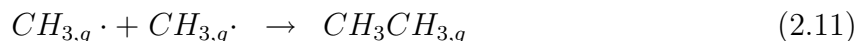
Beyond the energetical coupling which can be controlled by careful reactor design [43], a substantial coupling between surface and gas phase is also possible. Substantial coupling means that a reactive intermediate which is formed heterogeneously desorbs into the gas phase and causes subsequent homogeneous reactions. A prime example is the oxidative coupling of methane to ethylene and water:



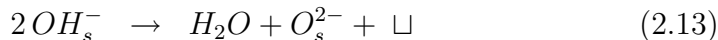
Using matrix isolation electron spin resonance, Lunsford [21] detected $CH_3\cdot$ radicals over alkali doped strong basic oxides (e.g. *Li/MgO*) commonly used as coupling catalysts. The observation of $CH_3\cdot$ radicals and the nearly exclusive formation of C_2H_6 lead him to the hypothesis that ethane is formed by the coupling of two $CH_3\cdot$ radicals in the gas phase and that ethene is formed in a consecutive dehydrogenation. Nelson et al. [45] supported this assumption by conducting the reaction with a mixture of CH_4 and CD_4 . He obtained CH_3CH_3 , CH_3CD_3 and CD_3CD_3 as the main coupling products:



A coupling at the catalyst surface would probably lead to a scrambling of the deuterium atoms. Actually, the role of the catalyst in this reactions is to produce $CH_3\cdot$ radicals emanating into the gas phase with subsequent coupling to C_2H_6 :

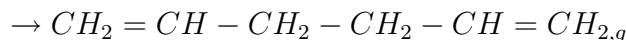
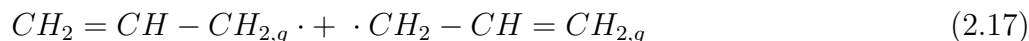
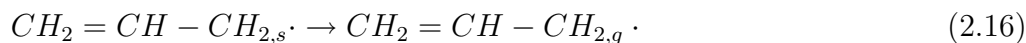
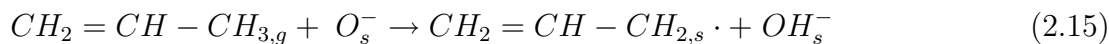


Ethene is then formed from ethane by subsequent oxidative dehydrogenation, proceeding again primarily in the gas-phase [46]. The catalytic cycle is closed via re-oxidation of the catalyst, with \square denoting an oxide ion vacancy:



In a further work on this reaction, Mimes et al. investigated the extensive gas-phase radical network initiated by the methyl radical desorption using both experimental and computational methods [47]. Their work illustrates very well that secondary reactions limit the yield of the desired product ethene and give rise to unwanted side products like CO_x and higher hydrocarbons.

Another example closely related to the one just described is the formation of gas-phase π -allyl radicals from propylene over bismuth oxide and γ -bismuth molybdate catalysts [22]. 1,5-hexadiene was formed by post-catalytic recombination of two such radicals:

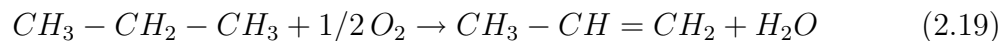


The number of gas-phase π -allyl radicals that were measured using matrix isolation **EPR**-spectroscopy correlated nicely with the number of 1,5-hexadiene molecules supporting the gas phase recombination mechanism. Further on it was found that the reaction with gas phase oxygen led to the formation of allyl peroxy radicals:

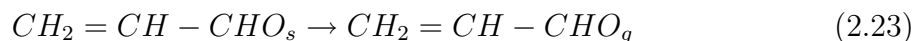
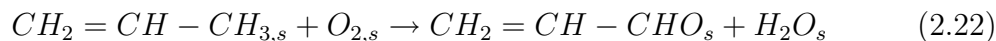
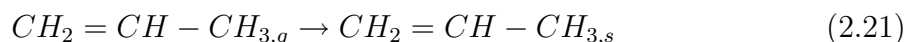
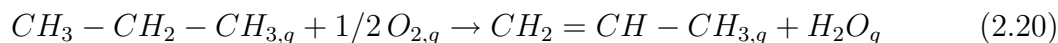


There was no indication that acrolein was formed via allyl peroxy radicals as their concentration satisfied the calculated equilibrium value of (2.18). Neither propylene oxide nor other oxygenated products could be detected. It is generally accepted that acrolein formation is purely heterogeneous on these catalysts [48]. That means, in contrast to the oxidative coupling of methane homogeneous reactions lead here exclusively to unwanted side products and have to be minimized.

Substantial coupling may work also vice versa in that reactive intermediates which are formed initially in the gas phase adsorb and react afterwards on the catalyst surface. Burch et al. investigated the oxidative dehydrogenation of propane on *MgO*-supported vanadium oxides and compared these results with propene yields obtained without catalyst [23]:



They found that with these catalysts, the maximum selectivity to propene at a specific conversion of propane was never higher than in the absence of a catalyst. This result is consistent with an earlier work of Kim et al. [24], who studied the selective oxidation of propane to acrolein on bismuth vanadomolybdate catalysts at temperatures around 500 °C. They used a packed bed reactor with a varying pre-catalytic volume. When this volume was minimized, no reactions occurred at all. Consequently, the following mechanism was proposed:



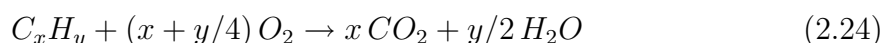
As a result, excellent catalysts for the oxidation of propane require activity for the oxidation of propene at a temperature, where the dehydrogenation of propane to propene proceeds efficiently in the gas phase.

These examples stress the importance to study bulk and surface as well as the gas phase in-situ to get a comprehensive view of the mechanism of a catalytic reaction. This knowledge embedded in a detailed macro-kinetic description improves existing technological processes and extends the understanding of heterogeneous catalysis.

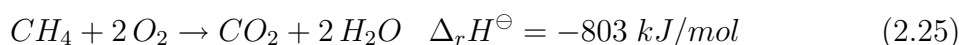
2.3 Investigated Reactions

2.3.1 Catalytic Combustion of Methane

The term ‘combustion’ is used for the reaction of a fuel with oxygen to CO_2 and H_2O :



Accordingly, methane combustion is presented by the following stoichiometric equation:



If the oxidation is not as deep one refers to it as ‘partial oxidation’. Conventional combustion is a self-sustaining exothermic process accompanied by formation of a flame. For stable gas phase (homogeneous) combustion, flame temperatures must generally exceed $1400^\circ C$ and range typically between $1500^\circ C$ and $1900^\circ C$, sometimes even more [49]. Due to such high temperatures and the fact that air is usually used as oxidant, numerous toxic pollutants like NO_x or polycyclic aromatic hydrocarbons are formed. Catalytic combustion represents an attractive alternative technology as schematically shown in figure [2.3]:

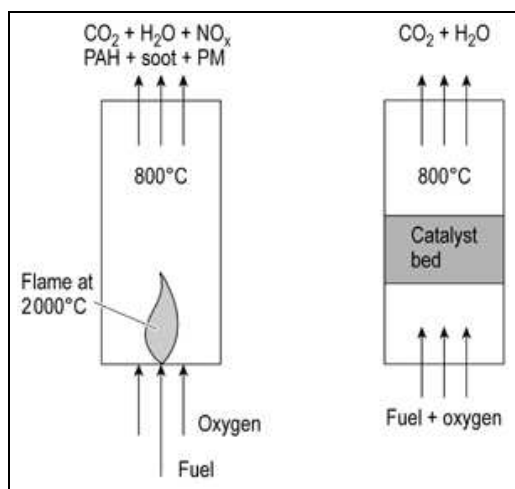


Figure 2.3: *Operation and pollutants production in conventional- and catalytic combustion (adopted from [49])*

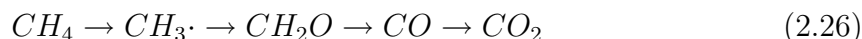
Fuel oxidation is achieved through participation of a solid catalyst as for instance Pt on a high surface area ceramic substrate, such as Al_2O_3 . In comparison to flames, catalytic combustion offers a set of advantages:

- higher degree of completion

- lower combustion temperature ($< 1000\text{ }^\circ\text{C}$)
- reduced pollutant formation
- stable operation at extremely fuel lean conditions

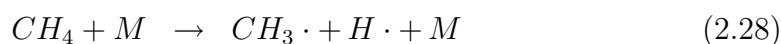
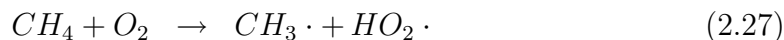
A comprehensive review on catalytic combustion is given by Prasad, Kennedy and Ruckenstein [50].

From a chemical point of view, combustion processes are known to proceed via radical chain reactions. It is known from literature [51, 52] that depending on the reaction conditions radicals like $OH\cdot$, $HO_2\cdot$, $CH_3\cdot$, $CH_3OO\cdot$ and saturated molecules like $HCHO$, CH_3OH or H_2O_2 have been found as intermediates in homogeneous methane combustion. A combustion mechanism is a complex network of chain initiation-, branching-, progress- and termination reactions each having different importance depending on flame temperature and composition. There is a low temperature regime (hundreds of K) where $CH_3OO\cdot$ and $OH\cdot$ radicals are the important chain carriers and there is a high temperature regime ($> 1000\text{ }K$) where $HO_2\cdot$ radicals replace $CH_3OO\cdot$ as peroxy species are unstable under these conditions. As an example, the general sequence of processes for CH_4 oxidation at high temperatures is:



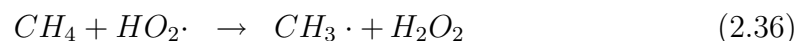
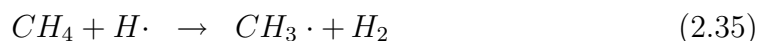
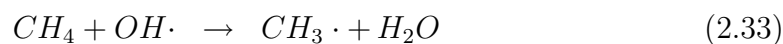
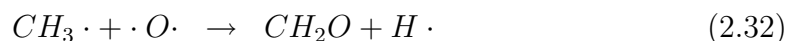
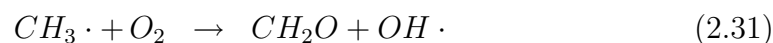
The radical chains connecting different oxidation stages interact with one another such that, for instance, radicals produced during CH_2O oxidation accelerate CH_4 oxidation. The following list shows exemplarily the different steps of a combustion chain with methane as feed gas [52]. The symbol M denotes an inert collision partner which is often required for a reactive collision to take up excessive kinetic energy:

- chain initiation

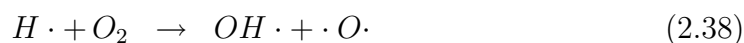
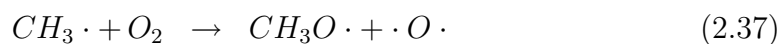


- chain progress

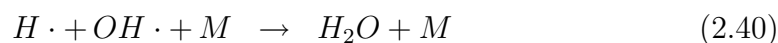




- chain branching



- chain termination



Especially laser-based diagnostic techniques proved extremely valuable to measure species concentrations, temperature profiles, even reaction dynamics of simple elementary steps [31, 53]. There might be a significant difference to heterogeneous systems and only few investigations have been published in this context, but at least $OH\cdot$ radicals have been detected as well using laser induced fluorescence spectroscopy [25]. This gave reason to use the catalytic combustion of methane as a test reaction for our apparatus system.

2.3.2 Ammonia Oxidation

Another Pt -catalyzed high temperature reaction suspected to involve gas phase intermediates is the ammonia oxidation [3, section 2.2]. Depending on feed composition, temperature, pressure and residence time one obtains three different oxidation products, N_2 , N_2O and NO . The formation of NO is of immense economical importance as it is the first step of the Ostwald process to nitric acid:



The industrial reactor employs knitted platinum-rhodium gauzes with a contact time in the sub-millisecond range. Regardless of the short contact time NO -yields of up to 98 % are obtained. Nitrogen monoxide formation commences at about 500 °C. At lower temperatures, the process proceeds in the kinetically controlled region and gives exclusively N_2O and N_2 :

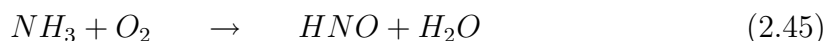


Reaction (2.41) exhibits the smallest enthalpy of reaction and is, according to van't Hoff's law (2.44), least influenced by temperature, resulting in enhanced NO formation with increasing T .

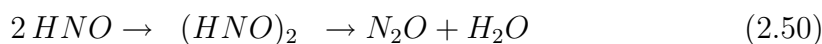
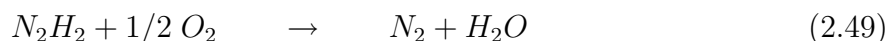
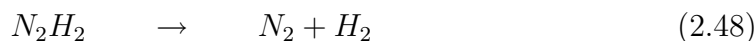
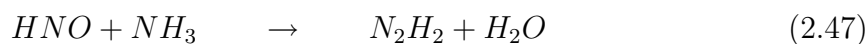
$$\left(\frac{\partial \ln K}{\partial T} \right)_p = \frac{\Delta_r H^\ominus}{RT^2} \quad (2.44)$$

The opposing influence of thermal NO decomposition starting at about 450 °C results finally in an optimal temperature range of 800 - 950 °C where all industrial reactors operate. Most ammonia burners apply higher pressures to increase the ammonia throughput, whereby the bad influence of pressure to equilibrium position of (2.41) is accepted.

The extraordinary high reaction rate of ammonia oxidation is probably the reason, that its mechanism is largely unknown [54]. Several theories have been proposed and discussed without any experimental proof under realistic conditions. The first proposal concerning a mechanism was made by Andrussow in 1926 [55]. He postulated nitroxyl HNO as an intermediate according to the following reaction scheme:



In a later publication [56] he speculated on side reactions to explain the N_2 and N_2O formation:

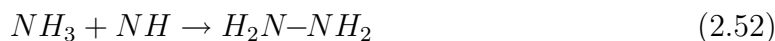


Neither HNO nor any other proposed intermediate could be observed experimentally.

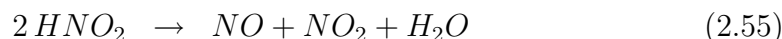
Raschig in 1927 [57], Hofman and Korpiun in 1929 [58] and later Zawadzki [59] reported Imid NH as the prime oxidation product:



They based their assumption on the detection of N_2H_4 in an NH_3/O_2 flame burning above a water surface. It was detected in solution using benzaldehyde as a reagent. The hydrazine formation was attributed to the following reaction, which was cited as evidence for imide as intermediate in the ammonia flame and hence in the catalytic ammonia oxidation as well:



The following reactions were then quoted to give NO :



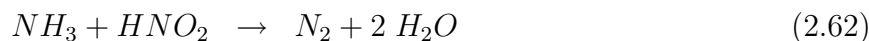
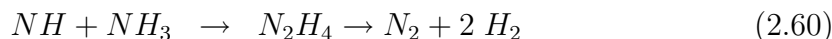
The catalytic cycle to reaction (2.51) is finally closed by:



As in Andrussov's mechanism, nitroxyl is likewise an intermediate here but with N_2O formation attributed to it:

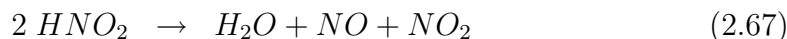
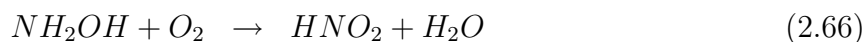


Numerous reactions are accounted to explain the formation of nitrogen:

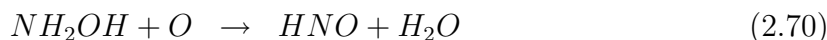
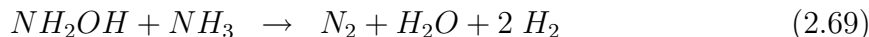


Without exception, all of these reactions were considered to occur on the catalyst surface. Although the flame experiment militates in favor of the imid-theory it is questionable to what extent these results are transferable to real catalytic conditions.

One step in this direction was made by Bodenstein who studied the Pt-catalyzed reaction [60] at pressures of about 10^{-2} Torr on a resistively heated platinum foil. The off-gas was frozen out on a glass wall cooled with liquid air. He found hydroxylamine NH_2OH , nitrous acid HNO_2 and nitric acid HNO_3 leading him to the following reaction mechanism:



Side reactions involving again nitroxyl lead to N_2 and N_2O :



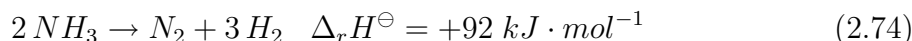
In agreement with Zawadzki, Bodenstein considered the reactions to run on the platinum surface.

None of these theories could ever be confirmed or rejected for realistic reaction conditions [61]. A surface science approach to check up on the different theories was to investigate the catalyst surface after reaction using secondary ion mass spectrometry [62]. It was not possible to detect neither HNO nor NH_2OH nor NH . One publication was found in which **LIFS** was used to get insight into the reaction mechanism, at least for pressures in the *mbar* range. Selwyn et. al. [27] probed a pool of transient species ($\cdot NH\cdot$, $NH_2\cdot$, $OH\cdot$, HNO and NO_2) above the platinum catalyst, among which only the diatomic species $\cdot NH\cdot$ and $OH\cdot$ were detected. This result in turn suggests strongly, that the oxidation reaction proceeds primarily via atomic and radical pathways.

The ammonia oxidation reaction has been investigated extensively in this work (Section 5.2). It seems particularly favorable that numerous potential intermediates show up at masses in the mass spectrum not superimposed by peaks of reactants and products (NH_2OH at 33 *amu*, HNO at 31 *amu*, HNO_2 at 47 *amu*, NO_2 at 46 *amu*). Superimposed signals like for $\cdot NH\cdot$ at 15 *amu* and $OH\cdot$ at 17 *amu* might be investigated using the threshold ionization technique.

2.3.3 Ammonia Decomposition over Platinum

To make the transition from the exothermic oxidation reactions to the oxygen free endothermic HCN formation, the *Pt*-catalyzed ammonia decomposition has been chosen as another test reaction:



Contrary to any other reaction investigated within this work, it has been studied previously using threshold ionization mass spectrometry [28]. A special mass spectrometer was designed for that purpose with a platinum wire placed inside the ion source just above the electron beam [29]. This arrangement reduced both the number of secondary reactions and the time between production and observation. Off course, handling electrons restricts the method with respect to the highest allowable pressure to about 1 *mbar*. Three free radicals, $N\cdot$, $\cdot NH\cdot$, $NH_2\cdot$, have been observed in the gas phase and, hence, must have desorbed from the surface of the catalyst. The results exemplify that platinum is very effective in splitting $N-H$ bonds and that the radicals exist long enough on the surface to desorb. These observations made the reaction worth investigating before the binary CH_4/NH_3 system has been tackled.

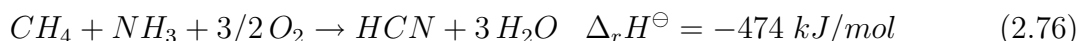
2.3.4 Hydrocyanic Acid from Methane and Ammonia

The primary goal of this work was to study the high temperature formation of hydrocyanic acid from methane and ammonia over platinum:



This highly endothermic reaction, frequently abbreviated as **BMA**-process (**B**lausäure aus **M**ethan und **A**mmoniak) is one of the two major industrial production routes

to HCN [63]. It is performed in externally heated alumina tube bundles, which are coated with a thin layer of a special platinum catalyst. Several of these bundles are fixed in a reaction furnace unit. A mixture of ammonia and methane is passed through the tubes which are kept at about 1300 °C. The reaction is conducted under normal pressure. Carbon formation is prevented using a slight excess of ammonia ($1.01 < p_{NH_3}/p_{CH_4} < 1.08$). The competition process, named after his inventor L. Andrussow [56], uses internal heat generation by adding extra oxygen (air) to the feed making the entire reaction exothermic:



The process management is closely related to the ammonia oxidation, using likewise platinum-rhodium gauzes as a catalyst. Hydrocyanic acid is an important intermediate for the chemical industry with a world production capacity of approx. $1.5 \cdot 10^6 \text{ t/a}$ [64]. It is a basic feedstock for the production of metal cyanides, methyl methacrylate, adiponitrile, cyanuric chloride and methionine. Beyond it, a wide variety of organic intermediates can also be made from HCN, which have a diversified chemistry on their own.

In spite of the successful application of the **BMA**-process since nearly half a century, little is known about its mechanism. Pfeil and Hoffmann [65] studied the kinetics of the HCN formation over platinum and found an agreement between the apparent activation energy of this reaction and of the ammonia decomposition. Furthermore the rate law for the HCN formation is first order in the partial pressure of ammonia. They concluded the rate limiting step to be the dehydrogenation of ammonia to $\cdot NH\cdot$, which reacts further with methane to methylamine. Dehydrogenation via methylenimine leads finally to HCN. Important side reactions are the ammonia decomposition to N_2 and H_2 and soot formation, as they decrease the HCN-yield or poison the catalyst respectively. Figure 2.4 shows the mechanism as suggested by Pfeil and Hoffmann.

It stays to mention that the proposed intermediates CH_3-NH_2 and $CH_2=NH$ have not been observed experimentally. A more recent and theoretically well-founded investigation was performed by Diefenbach et al. using **FTICR** -mass spectrometry supported by quantumchemical calculations [66]. Using a Pt^+ -cation as a model catalyst they suggest two possible formation routes to HCN, one exclusively hetero-

geneous and the other with the dehydrogenation of methylenimine as a homogeneous step. Figure 2.5 shows their results. The proof of the homogeneous participation is again missing.

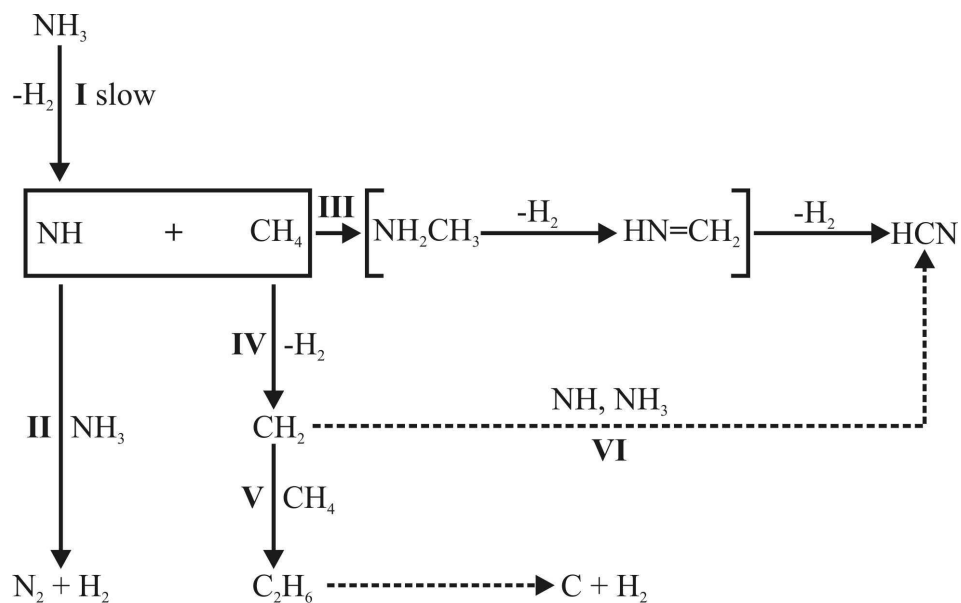


Figure 2.4: *BMA* -mechanism based on Pfeil et al., I) dissociative ammonia adsorption - rate determining step II) nitrogen formation III) hydrocyanic acid formation via methylamine and methylenimine IV,V) methane pyrolysis VI) alternative route to HCN, adopted from [65], changed

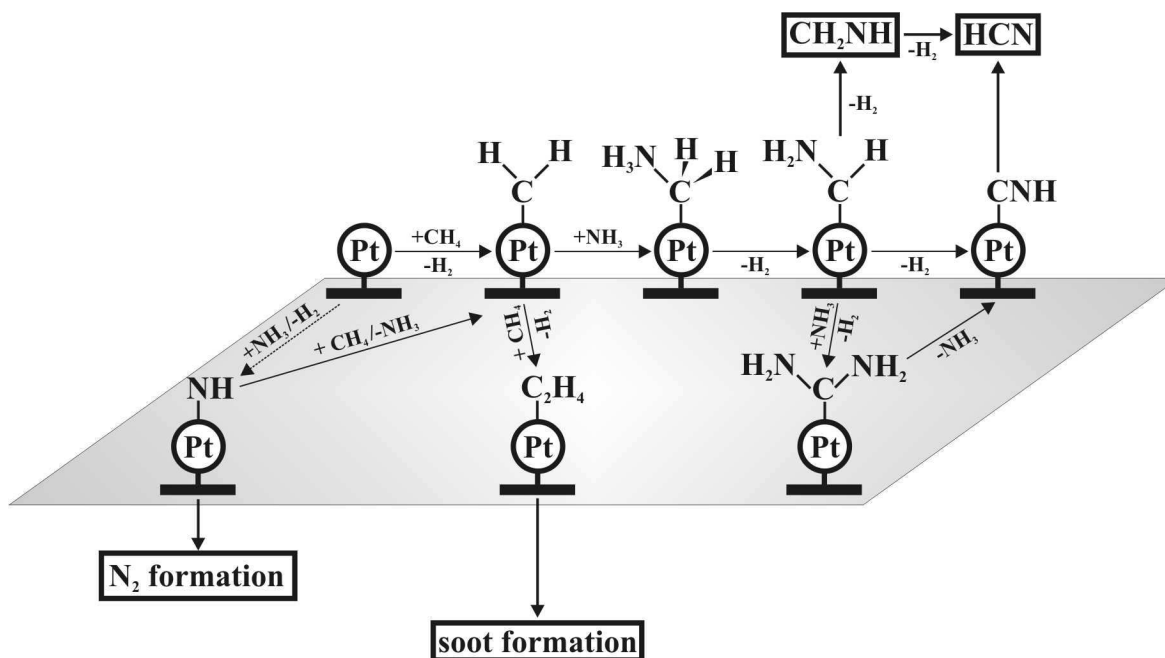


Figure 2.5: *BMA* -mechanism based on Diefenbach et al., adopted from [66], changed

Chapter 3

Physical Background

The goal of the present work is to measure and interpret chemical data. However, before this can be done satisfactorily, emphasis has to be placed on the method itself, making a thorough exploration of its physical background necessary. Besides helping to interpret the measured data, a fundamental understanding permits an apparatus check in terms of fulfilling basic requirements.

Generally speaking, the experiment contains two physical main focuses. First of all, the reacting species have to be sampled and stabilized for the detection, bearing the in-situ idea in mind. This is preferably done using a molecular beam sampling interface. The physics behind such an interface is really challenging and demands therefore an elaborate design paying special attention to the nonlinear nature of a supersonic expansion. For this reason the chapter starts with a presentation of fundamentals of molecular beams and how to exploit these principles in dynamic sampling (Section 3.1).

Provided a successful probing, the specific detection of the species of interest is the second demanding problem. Because of the diversity of potential gas phase species, a versatile detection method has to be used. Quadrupole mass spectrometry allows a highly sensitive detection of each molecular species in the mass range of interest. Section 3.2 outlines the physical background of mass spectrometry with a focus on mass separation using a quadrupole mass filter. The disadvantage of the method is its inherent lack of selectivity due to a limited spectral resolution restricted to integer mass numbers. Expanding the spectra by another dimension by measuring the near

threshold ionization behavior is an attempt to discriminate between different species at the same nominal mass. This technique, in plasma physics known as appearance potential mass spectrometry, is presented in Section 3.3. In the first instance, the question for homogeneous contributions should be answered on a qualitative level. That is why physical characteristics of the tubular wall reactor are not discussed in this chapter. They become highly important if the measurements need to be analyzed quantitatively.

3.1 Molecular Beams

3.1.1 General Statements, Classification, Applications

A molecular beam can be defined as a collimated stream of molecules moving under essentially collision-free conditions through a vacuum. Molecular beams are versatile tools to study the physics and chemistry of matter [67, chapter 1]. Typical applications are for instance collision experiments in molecular physics, investigations on chemical reaction dynamics, spectroscopy on jet cooled molecules, surface science studies or as in the present case continuous sampling of dynamic systems. To characterize the molecular beam experiment done in this work it is necessary to contemplate the flow regime of the molecules leaving the sampling orifice.

If their mean free path is small compared to the diameter of the orifice, the flow is determined by collisions of the beam particles among themselves. In this case, the gas can be treated as a continuum and the flow is described by gas dynamics. Under such conditions, a continuous, viscous beam flow will be established. If the gas is expanded from a high pressure (a few *bar*) side through a nozzle in a low pressure (a few *mbar* or less) background, the source is referred to as ‘free jet’- or ‘supersonic’ source [67, chapter 2]. In the way the source is operated, beam energies between thermal energy and approximately 20 *eV* are possible. Because dissociation energies of chemical bonds and activation energies lie in this range, supersonic beams are often used to study chemical reactions. In addition, the expansion causes a narrowing of the energy spread of the beam molecules perpendicular to the beam axis, making such beams suitable for spectroscopic experiments.

If the mean free path of the gas particles is larger than the orifice diameter, wall collisions are more frequent than collisions among the particles. There is no flow work dp/ρ that forces the molecules to expand through the orifice, it is rather accidentally if a molecule hits the wall in place where the hole is. Therefore, the gas needs to be considered microscopically using the laws of gas kinetics and the molecular beam is of an effusive type [67, chapter 4]. As collisions between particles and source walls are more frequent than among the particles themselves, the atoms or molecules can at best equilibrate to the temperature of the source walls. As a result, the beam particles have only thermal energy of a few tenths of an electron volt with a broad energy distribution. There are source materials available allowing up to 3000 K restricting the maximum energy of an effusive source to about 1 eV. Effusive beams are frequently used to deposit atoms or molecules homogeneously on surfaces.

A criterion to distinguish between the different beam types is the Knudsen number of the beam source defined as the ratio of the mean free path \bar{l} of the source particles to the orifice diameter d_n :

$$Kn = \frac{\bar{l}}{d_n} \quad (3.1)$$

The flow regimes are classified as follows [68, page 76 et seq.]:

Table 3.1: *Gas flow regimes*

Knudsen number	flow regime	described by	beam type
$Kn < 10^{-2}$	continuous flow	gas dynamics	supersonic
$10^{-2} < Kn < 0.5$	Knudsen flow	interpolation	rarely used
$Kn > 0.5$	molecular flow	gas kinetics	effusive

The diameter of the sampling orifice used in this work was $d_n = 125 \mu m$. The stagnation parameters (parameters inside the source, T_0, p_0) are predetermined by the reaction conditions. The reactions were conducted under ambient pressure ($p_0 = 101325 Pa$) and the sampled gases had a temperature varying between $T_{0,min} = 293 K$ and $T_{0,max} = 1573 K$. Using for example the collision cross section for nitrogen $\sigma = 1.4 \cdot 10^{-19} m^2$ [69, page 6-47], one can calculate the mean free path and out of it the Knudsen number of the source according to:

$$\frac{kT_{0,min}}{\pi\sqrt{2}p_0\sigma} < \bar{l} < \frac{kT_{0,max}}{\pi\sqrt{2}p_0\sigma} \quad (3.2)$$

$$\frac{\bar{l}_{min}}{d_n} < Kn < \frac{\bar{l}_{max}}{d_n} \quad (3.3)$$

$$5 \cdot 10^{-4} < Kn < 3 \cdot 10^{-3} \quad (3.4)$$

The result shows, that the beam type is supersonic for all experimental conditions. Contrary to effusive expansions, supersonic expansions show involved phenomena like shock wave formation and mass separation. The origin of these features and their consequences are presented in the following section.

3.1.2 Physical Characteristics of Supersonic Molecular Beams

Supersonic molecular beams are neutral beams extracted from a continuum expansion from a high pressure gas source into a low pressure background [70, 71]. Most widespread for extraction are axisymmetric arrangements of cones as shown schematically in Figure 3.1:

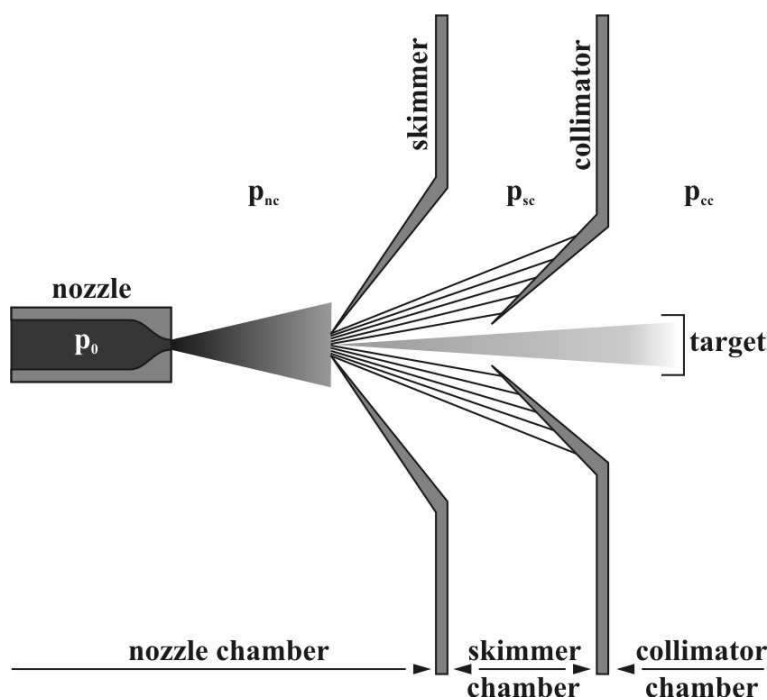


Figure 3.1: Generation of supersonic beams using a differentially pumped arrangement of nozzle, skimmer and collimator: p_0 = stagnation pressure, p_{nc} = pressure in nozzle chamber, p_{sc} = pressure in skimmer chamber, p_{cc} = pressure in collimator chamber

To understand the supersonic nature of the expansion it is necessary to analyze it using the equations of fluid dynamics [72]. A thorough treatment of the three-dimensional case is difficult, but a simplified consideration of an one-dimensional adiabatic expansion helps to illustrate the principle as well [68, page 45 et seqq.]. Figure 3.2 shows the corresponding model:

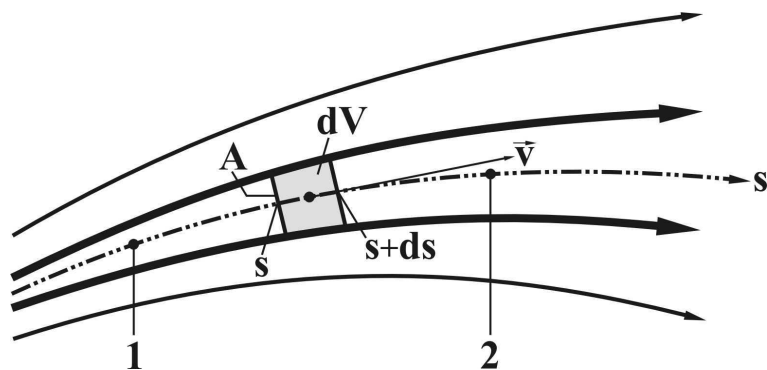


Figure 3.2: *Flow field model for an one-dimensional continuous expansion, adopted from [68, page 45 et seqq.]*

Considered is a volume element $dV = A ds$ that moves along a streamline s . The forces acting on the volume element of the mass $dm = \rho dV$ from the left F_l and from the right F_r are different because of the pressure gradient dp/ds :

$$F_l = pA \quad (3.5)$$

$$F_r = \left(p + \left(\frac{dp}{ds} \right) ds \right) A \quad (3.6)$$

The net force dF that accelerates the volume element is given as the difference between F_l and F_r :

$$dF = F_l - F_r = -A \left(\frac{dp}{ds} \right) ds \quad (3.7)$$

The movement caused by dF is described by Newton's law according to:

$$dF = dm \left(\frac{dv}{dt} \right) = dm \left(\frac{dv}{ds} \right) \left(\frac{ds}{dt} \right) = dm \cdot v \left(\frac{dv}{ds} \right) \quad (3.8)$$

Equation (3.7) can be equated with (3.8):

$$-A \left(\frac{dp}{ds} \right) ds = \rho \cdot A \cdot ds \cdot v \left(\frac{dv}{ds} \right) \quad (3.9)$$

Rearranging (3.9) leads to Bernoulli's law in its differential form:

$$-\left(\frac{dp}{\rho} \right) = \frac{1}{2} dv^2 \quad (3.10)$$

Integration of (3.10) along the streamline s from position 1 to position 2 gives an integral relating the flow velocities at these points. If point 1 is chosen to lie upstream the nozzle (v_0, ρ_0, p_0) and point 2 is downstream the nozzle in the nozzle chamber

(v_{nc} , ρ_{nc} , p_{nc}) one can calculate the speed of the beam particles at any point in the expansion provided that the flow is still continuous:

$$\frac{1}{2} (v_{nc}^2 - v_0^2) = - \int_{p_0}^{p_{nc}} \frac{dp}{\rho} \quad (3.11)$$

To calculate the integral (3.11) one needs an equation of state that relates ρ and p . As the expansion is in good approximation adiabatic it is possible to use Poisson's law:

$$\left(\frac{p}{p_0}\right) = \left(\frac{\rho}{\rho_0}\right)^\kappa \rightarrow \frac{1}{\rho} = \frac{1}{\rho_0} \left(\frac{p_0}{p}\right)^{\frac{1}{\kappa}} \quad (3.12)$$

The gas upstream the nozzle can be considered to be at rest ($v_0 \approx 0$) and p_0/ρ_0 can be substituted by RT_0/M . Integration leads then to the following important relationship:

$$v_{nc} = \left(\frac{2\kappa}{\kappa - 1} \frac{RT_0}{M} \left[1 - \left(\frac{p_{nc}}{p_0} \right)^{\frac{\kappa-1}{\kappa}} \right] \right)^{\frac{1}{2}} \quad (3.13)$$

Equation (3.13) states that the velocity v_{nc} , reached by the beam particles during the expansion into the nozzle chamber depends on the source temperature T_0 and on the expansion ratio p_{nc}/p_0 . The highest possible speed v_{max} is reached at maximum expansion, that means if the background pressure p_{nc} is 0:

$$v_{max} = \sqrt{\frac{2R}{M} \left(\frac{\kappa}{\kappa - 1} \right) T_0} \quad (3.14)$$

The speed of sound v_{sd} in an ideal gas of pressure p and density ρ is given by:

$$v_{sd} = \left(\frac{p}{\rho} \cdot \kappa \right)^{\frac{1}{2}} \quad (3.15)$$

By using again Poisson's law one can relate the speed of sound to the conditions in the source:

$$\left(\frac{p}{p_0}\right) = \left(\frac{T}{T_0}\right)^{\frac{\kappa}{\kappa-1}} \rightarrow v_{sd} = \left(\frac{RT}{M} \cdot \kappa\right)^{\frac{1}{2}} = \left(\frac{RT_0}{M} \cdot \kappa \left(\frac{p}{p_0}\right)^{\frac{\kappa-1}{\kappa}}\right)^{\frac{1}{2}} \quad (3.16)$$

The beam particles reach speed of sound if the pressure in the nozzle chamber is equal to a critical value p_{nc}^* so that $v_{nc}^* = v_{sd}$:

$$\left(\frac{2\kappa}{\kappa-1} \frac{RT_0}{M} \left[1 - \left(\frac{p_{nc}^*}{p_0} \right)^{\frac{\kappa-1}{\kappa}} \right] \right)^{\frac{1}{2}} = \left(\frac{RT_0}{M} \cdot \kappa \left(\frac{p_{nc}^*}{p_0} \right)^{\frac{\kappa-1}{\kappa}} \right)^{\frac{1}{2}} \quad (3.17)$$

Rearranging (3.17) leads to a simple relationship for the critical pressure in the nozzle chamber:

$$p_{nc}^* = p_0 \cdot \left(\frac{2}{\kappa+1} \right)^{\frac{\kappa}{\kappa-1}} \quad (3.18)$$

With the help of these equations it is now possible to assess the flow characteristics of the molecular beam interface used in our machine. The reactor was always operated at atmospheric pressure ($p_0 = 1013 \text{ mbar}$). Using Equation (3.18) and again nitrogen as example ($\kappa = 7/5$), supersonic flow would have occurred if the pressure in the nozzle chamber had been lower than 535 mbar . The nozzle chamber was evacuated by two rotary vane pumps supplying a pressure in the range of ($p_{nc} = 1 \text{ mbar}$). As a result, the flow was well in the supersonic range. The sampled gases had a temperature varying between $T_{min} = 293 \text{ K}$ and $T_{max} = 1573 \text{ K}$. This leads (again for nitrogen) to the following values for the speed v_{nc} and the kinetic energy of the beam molecules E_{kin} :

$$724 \text{ m/s} < v_{nc} < 1678 \text{ m/s} \quad (3.19)$$

$$0.2 \text{ eV} < E_{kin} < 1.0 \text{ eV} \quad (3.20)$$

These results are important for the experiments as they make clear, that the energy of the beam particles with which they enter the mass spectrometer depends on the temperature of the reactor. Furthermore, there is a dependence on the molar mass of the gas. Lighter molecules reach higher velocities than heavier ones. It follows that heavier molecules can be accelerated by diluting them with a light gas like helium or hydrogen and vice versa (seeded beam technique). The settings of the ion source and of the quadrupole mass filter have to be adjusted to E_{kin} [q.v. section 3.2].

During the expansion, the increase of the mean velocity goes along with a decrease in particle density and collision frequency [Fig. 3.3]. At some point in the expansion the collision frequency becomes too low to maintain continuum flow conditions leading to a transition into free molecular flow. From that point on the relaxation of vibrational, rotational and translational degrees of freedom is frozen because further collisions are absent. Because of their different relaxation rates the freezing occurs in

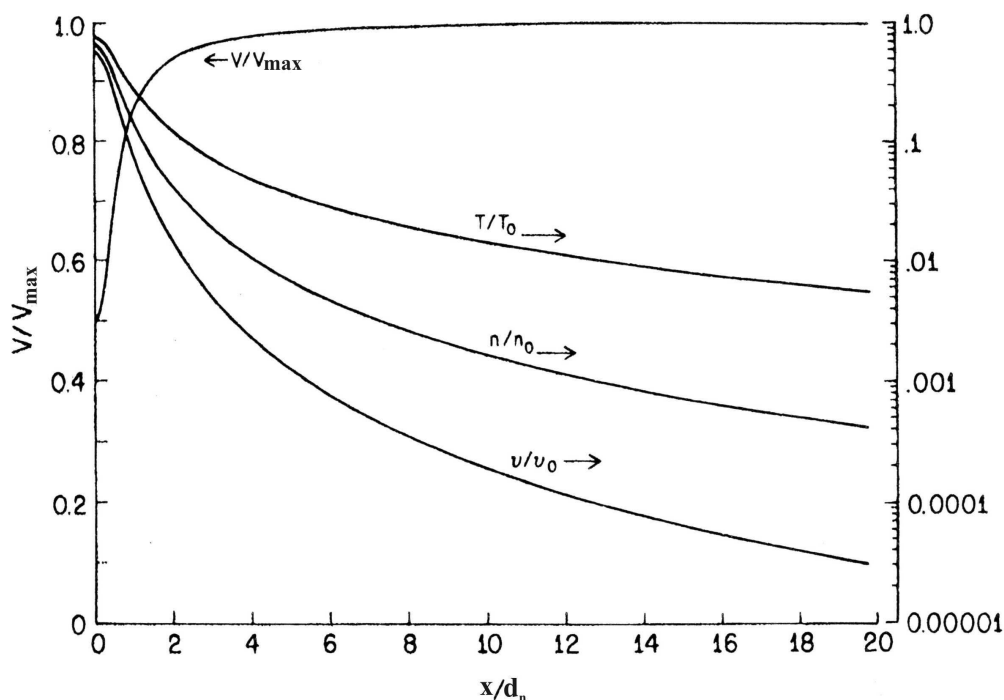


Figure 3.3: Free jet centerline properties versus distance x in source diameters d_n , $\kappa = 5/3$, temperature - T , particle density - n , binary hard sphere collision frequency - ν , normalized by source stagnation values T_0 , n_0 , ν_0 , adopted from [67, p. 18], changed

the order $T_{vibration} > T_{rotation} > T_{translation}$. This makes a molecular beam an outstanding tool for molecular spectroscopy. Furthermore, the ceasing of collisions protects reactive species against further reactions, which is the most prominent feature for the present work.

Despite the advantages offered by supersonic beams they bring along numerous pitfalls for the operator due to their nonlinear nature. Because a pressure information can only move with sound speed, the beam molecules do not sense the downstream conditions in the nozzle chamber. This results in the formation of shock waves, being the most suspicious phenomenon in supersonic expansions.

Contrary to shock waves, sound waves are small disturbances in a medium propagating with a definite speed. Sound waves are linear in nature meaning that the discontinuities in pressure, temperature and flow velocity are comparably small and propagate without being changed. However, in the case of an immense disturbance like for instance a detonation or even an abrupt pressure reduction the resulting

discontinuity is propagated through shock fronts advancing not at sonic but at supersonic speed relative to the medium ahead of them. Laws of superposition, reflection and refraction are no longer valid. From a mathematical point of view nonlinear waves are described by nonlinear partial differential equations that do not admit continuously extended solutions. A thorough mathematical treatment of supersonic flow and shock waves is given in [73]. For an axisymmetric expansion as used in this work there are shock waves with rotational symmetry around the centerline axis called barrel shocks and the so called mach disk perpendicular to it [74, 75]. Figure [3.4] shows the structure of a continuum free jet expansion:

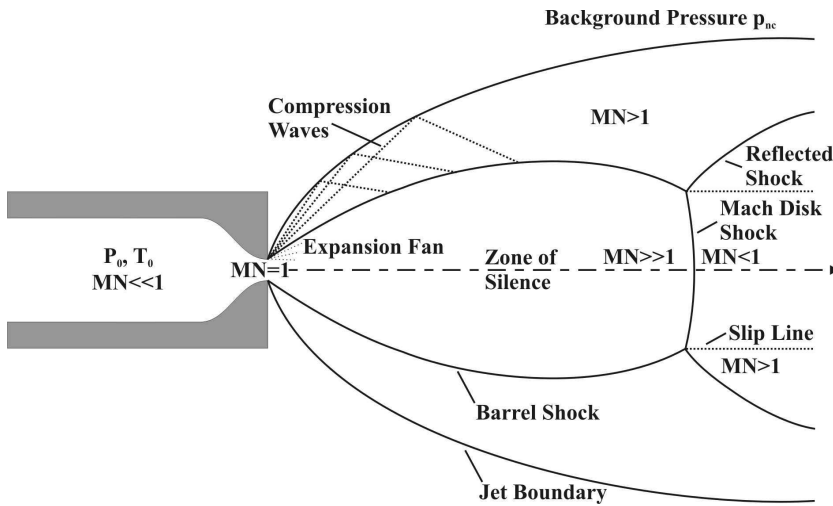


Figure 3.4: Continuum free-jet expansion, adopted from [67, p. 15], changed

The mach disk location x_M is remarkably insensitive to κ and can be calculated in multiples of the source diameter d_n according to:

$$\left(\frac{x_M}{d_n}\right) = 0.67 \cdot \sqrt{\frac{p_0}{p_{nc}}} \quad (3.21)$$

To reach stable conditions, the skimmer tip must not be placed inside or downstream of a shock wave rather it has to be positioned upstream the mach disk in the isentropic zone of silence. This requirement separates supersonic beam sources into two groups [76]. If mechanical pumps are used that offer the advantage of a small nozzle chamber and vacuum pipe connections, the background pressure downstream the nozzle (p_{nc}) is merely in the *mbar*-range. This leads to a very small zone of silence with a mach disk shock close behind the nozzle exit. This type of source, commonly referred to as ‘Campargue’-type requires an elaborate mechanics to adjust the skimmer properly [77]. To avoid these difficulties, most supersonic sources apply strong diffusion pumps to reach a sufficient low background pressure with a

shock wave structure beyond the dimensions of the machine. These sources are called ‘Fenn’-type sources.

The last point addressed in this chapter is the problem of mass separation during the expansion and the skimmer extraction. Four mechanisms were proposed to explain the separation phenomenon of gas mixtures in molecular beam sampling [78]:

- pressure separation
- free molecular diffusion
- skimmer induced separation
- background penetration

Pressure separation occurs within the first nozzle diameters of flow where the pressure gradients are high and streamline curvature is severe. The lighter species are stronger accelerated laterally. Molecular diffusion separation arises in the free molecular region of the beam. The thermal velocity spread of heavier particles perpendicular to the center line is less than of lighter ones. This causes again an enrichment of heavier molecules in the central beam. Skimmer induced separation is caused by a shock wave rising up in front of the skimmer tip if it is placed in the continuum region. The shock wave decelerates the molecules, the lighter more than the heavier ones. The inclined skimmer shock causes finally a mass separation by passing heavy molecules and deflecting lighter ones. This effect can be minimized by an elaborate skimmer design and by placing it downstream the transition to molecular flow. At progressed expansion the background pressure approaches that of the jet center. Light molecules have a higher diffusivity and can diffuse into the jet leading to an enrichment. Mass separation becomes important if one needs a quantitative interpretation of the measured data or for a calibration with a reference method.

3.2 Quadrupole Mass Spectrometry

Mass spectrometers are instruments that separate and analyze molecules or atoms of the sample under investigation according to their mass to charge ratio m/z . As the

huge diversity of physical operating principles makes a comprehensive presentation impossible, this basic section describes a quadrupole mass spectrometer equipped with an electron impact ionization source and a channeltron detector as it was used within this work.

3.2.1 Dynamic Sampling

The first step in a mass spectrometric analysis is the step of sampling. As founded in Section 3.1.2, supersonic beams have proved as a valuable sampling tool for mass spectrometry [79, 80]. A matter of particular interest is the sampling of dynamic systems like flames [81], chemical reactions [82], discharges [83], CVD-processes [84], plasmas [36], that is all systems in which the chemical composition as well as fluid dynamic variables are time variant. There are four major objectives in dynamic sampling:

- identification of stable, transient and excited species [85, 86]
- quantitative determination of the species present
- determination of fluxes and reaction rates [87]
- spatial resolution in terms of species concentrations [88]

At the early stage of this work the focus was on the identification of transient species in heterogeneously catalyzed reactions. The basic problem here is to take a representative sample with a minimal disturbance to the system (in-situ) followed by a rapid quenching of all reactions and relaxations within the molecular beam. With conventional nozzle diameters (typically 50–200 μm) the quenching is achieved within 1 to 3 μs , fast enough to sample reactive species like radicals or even excited molecules. Basically two types of arrangements proved valuable for dynamic sampling of chemical reactions [Fig. 3.5]:

From a technical point of view, the use of an external nozzle is more straightforward, as it can easily be aligned with the rest of the sampling system. With regard to the ‘in-situ’ character, an external nozzle is unfavorable as the nozzle has to be placed directly in the reaction zone to take a representative gas portion. Beside changing

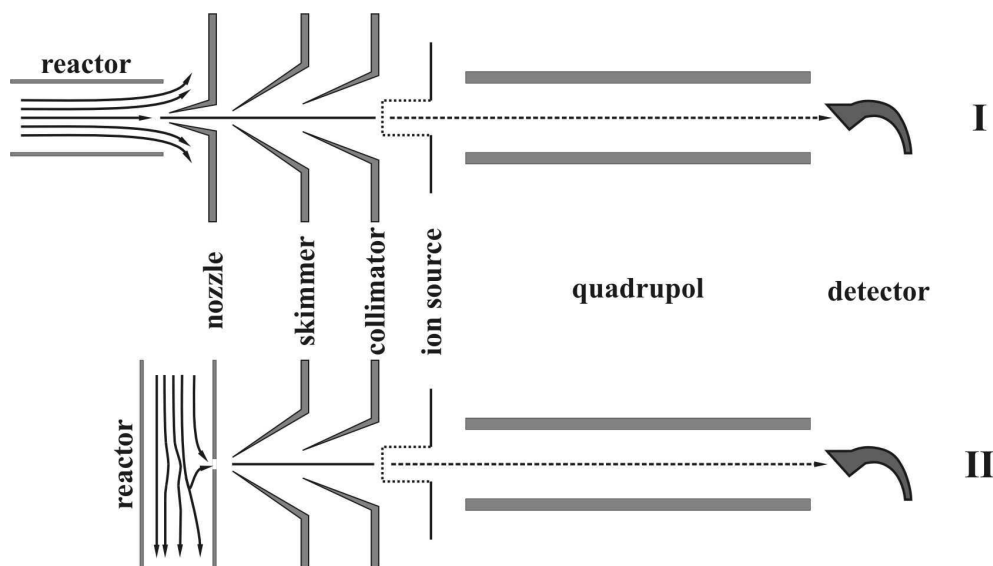


Figure 3.5: Arrangements for dynamic sampling of chemical reactions: I) arrangement with external nozzle [82] II) arrangement with internal nozzle [89]

flow conditions, the nozzle material itself can serve as a catalyst leading to undesired reactions. To minimize this effect the nozzle needs to be cooled especially at high temperatures. More elaborate is the use of an internal nozzle, which means that the sampling orifice is drilled in the reactor wall. As a result, the whole reactor needs to be placed inside a vacuum chamber maintaining its adjustability. The higher effort pays off by disturbing the reaction to a lesser extent apart from a marginal change of the flow conditions. Realization and consequences of the sampling process within this work are discussed in Section 4.3, in Section 5.1.1 and in Chapter 6.

3.2.2 Ion Generation

Mass spectrometric instruments of any type such as e.g. quadrupole, sector field, fourier transform or time of flight devices use electromagnetic forces on charged particles for a mass specific analysis. Therefore the second step after sampling is the generation of, in the majority of cases, positively charged ions [90]. Electron impact ionization is widely used for that purpose. Figure 3.6 shows the ion source used in our MS, the HAL4 EPIC Low Energy spectrometer from Hiden Analytical Limited:

This source is a so called ‘Cross Beam’ source with the molecular beam and the electron beam perpendicular to each other. This special design prevents condensation

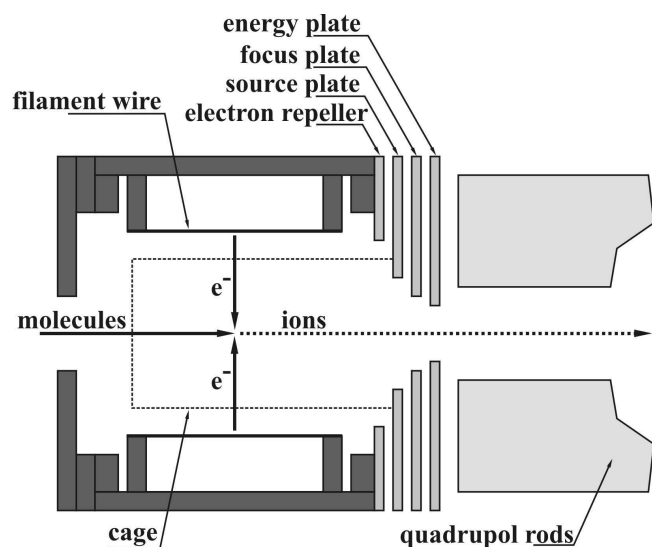


Figure 3.6: *Cross beam ion source of the HAL4 EPIC Low Energy, adopted from [91], changed*

of beam molecules on source components. Substitutional for others the mode of operation of an electron impact source is illustrated on that example. The potential diagram, necessary for an understanding, is given in Figure [3.7]:

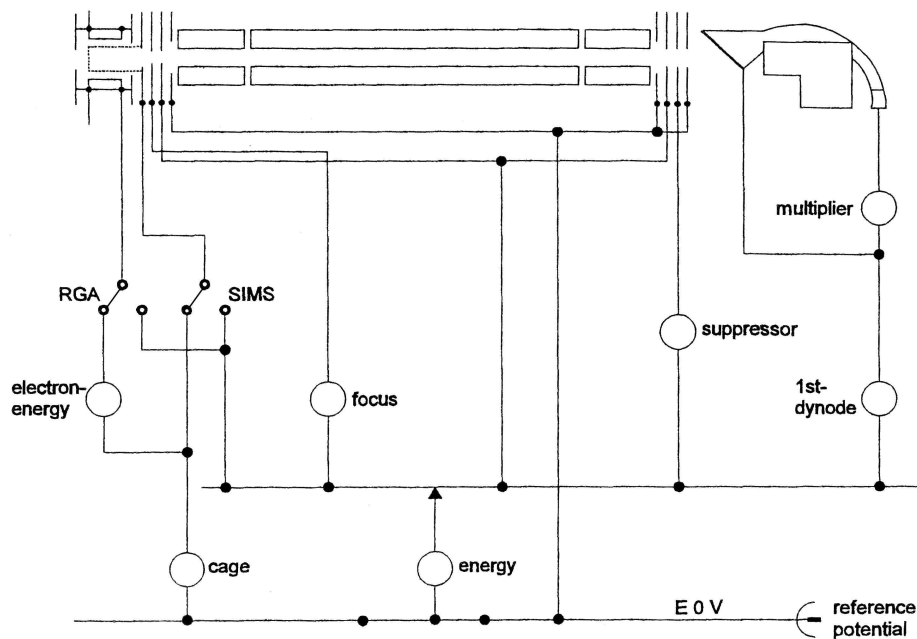


Figure 3.7: *Electrodes of the HAL4 EPIC Low Energy mass spectrometer, open circles denote voltage sources, adopted from [92, page 74], changed*

The electrons are emitted from a heated filament (cathode) and accelerated towards a wire cage (anode) in which the ionization takes place. Typical cathode materials are tungsten, rhenium or thoriated iridium. The electrons obtain a kinetic

energy E_{kin} that equals the potential difference U between the two electrodes:

$$E_{kin} = e \cdot U \quad (3.22)$$

Because the total ionization cross section of most of the atoms and molecules has a broad maximum between 50 and 150 eV, the ion source is frequently operated at 70–80 eV. Appearance potential measurements are done by scanning the voltage between filament and cage and hence the electron energy according to Equation (3.22). The cathode, the cathode housing and the anode are set to a potential well above ground minimizing electron losses through the repulsion by the mass potential of the surroundings. Since the ionization occurs in an almost field free region, the energy spread in the ion beam is small. In the Hiden spectrometer, thoriated iridium is used as cathode material. ThO_2 withstands severe thermal stress, has a low work function (2.96 eV [93]) and dissipates heat better and more homogeneously than other materials do [94]. These features are very important for operation at low electron energies (threshold ionization experiments). In such an experiment, the emission has to be constant over the entire energy range. Lowering the electron energy at constant emission goes along with an increase of filament temperature and energy spread. Therefore, the lower the work function of the cathode is, the lower is the filament temperature and the higher is the energetic resolution. After ionization the positively charged ions are drawn out of the source and imaged on the quadrupole entrance by means of a focus electrode. The focus potential is about 250 V lower than the cage potential leading to a fast extraction that minimizes undesired ion reactions within the source. Behind the focus electrode is the so called energy plate. Its potential is slightly higher than the reference potential and decelerates the focused ions to an energy adapted for mass separation. The interplay between cage-, focus- and energy potential determines the speed with which the ions pass the quadrupole filter. If they travel too fast they can not perform enough **RF**-cycles (q.v. Section 3.2.3) leading to high signal intensities but poor mass resolution. Vice versa, well resolved peaks are obtained if the ions travel with a low speed downwards the quadrupole and perform many **RF**-cycles but than at the expense of signal intensity. Beside intensity and spectral resolution the source settings affect the nature of ions reaching the quadrupole. It is possible to suppress any signals of directly ionized beam molecules but to let pass ions formed by fragmentation within the source. This is due to their different kinetic energies (Franck-Condon-principle, q.v. Section 3.3.3).

As a consequence, any quantitative interpretation of mass spectral data particularly by using tabulated fragmentation patterns has to be done with care as the patterns depend sensitively on source parameters.

3.2.3 Mass Separation

After focussing the ion beam to the entrance of the quadrupole mass filter (**QMF**), mass separation occurs. As the name already implies, the quadrupole acts like a filter letting pass only ions of a chosen mass-to-charge (m/z) ratio and rejecting all others. This mode of action can be explained by looking at the geometry of the electrodes and their electric potential [95, 96]. Figure 3.8 shows the arrangement for ideal electrodes having hyperbolic cross-sections:

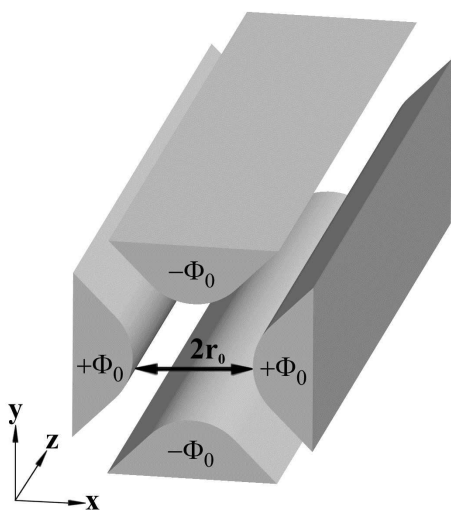


Figure 3.8: *Ideal quadrupole electrode structure with hyperbolic cross-sections, adopted from [96, page 10], changed*

In Cartesian coordinates the potential at any point inside an ideal quadrupole field can be expressed as sum of its perpendicular potentials:

$$\Phi(x, y, z) = \Phi(x) + \Phi(y) + \Phi(z) \quad (3.23)$$

The origin of the $x-y$ plane of the **QMF** is the center of the inscribed circle of radius r_0 within the electrode geometry and is chosen as the zero of the potential. It can be shown mathematically that the force acting on a charged particle in this field is proportional to its distance from the origin, e.g. $F_x \propto x$. The force in the x-direction is given by:

$$F_x = eE_x = -e \frac{\partial \Phi(x)}{\partial x} \quad (3.24)$$

As $\Phi(0) = 0$, the x-potential needs to have the form (3.25) with a being a constant of proportionality:

$$\Phi(x) = ax^2 \quad (3.25)$$

Due to the symmetry, the same holds for the y coordinate. There is no applied potential in z-direction so that:

$$\Phi(x, y) = ax^2 + by^2 \quad (3.26)$$

As long as there is no charge within the electrode arrangement, the field acts neither as a source nor as a sink and the Laplace equation has to be satisfied:

$$\text{div}\vec{\mathbf{E}} = \nabla \cdot \vec{\mathbf{E}} = \nabla \cdot \nabla\Phi = - \left(\frac{\partial^2\Phi}{\partial x^2} + \frac{\partial^2\Phi}{\partial y^2} \right) = 0 \quad (3.27)$$

Applying (3.27) to (3.26) leads to the following condition:

$$\nabla^2\Phi(x, y) = 2a + 2b = 0 \Rightarrow a = -b \quad (3.28)$$

The field boundaries supply expressions for the constants of proportionality:

$$\Phi(r_0, 0) = \Phi_0 = ar_0^2 \Rightarrow a = \frac{\Phi_0}{r_0^2} \quad (3.29)$$

$$\Phi(0, r_0) = -\Phi_0 = br_0^2 \Rightarrow b = -\frac{\Phi_0}{r_0^2} \quad (3.30)$$

Therefore, the **QMF** field equation is given by (3.31) with $\sigma = -\lambda = 1/r_0^2$

$$\Phi(x, y) = \Phi_0(\sigma x^2 + \lambda y^2) = \frac{\Phi_0}{r_0^2}(x^2 - y^2) \quad (3.31)$$

Figure 3.9 shows the equipotential lines obtained using Equation (3.31):

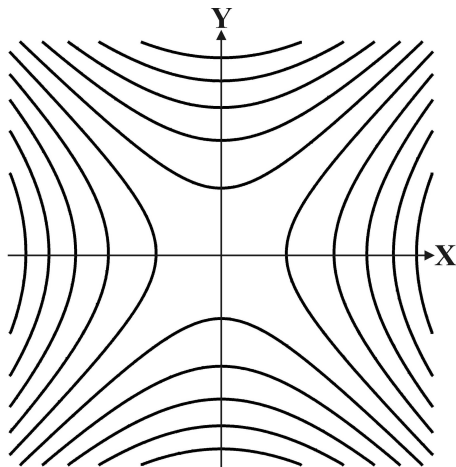


Figure 3.9: *Potential field of an ideal quadrupole, adopted from [96, page 10], changed*

The quadrupole is operated applying a **DC** voltage U and a **RF** voltage V to the rods:

$$\Phi_0 = U + V \cos(\omega t) \quad (3.32)$$

With ω being the angular frequency $2\pi f$ and t the time, the expression for the **QMF** field potential is:

$$\Phi(x, y) = \frac{(U + V \cos(\omega t))}{r_0^2} (x^2 - y^2) \quad (3.33)$$

The electric field components are the partial derivatives of Φ :

$$E_x = \frac{-\partial\Phi(x, y)}{\partial x} = \frac{-2}{r_0^2} (U + V \cos(\omega t)) x \quad (3.34)$$

$$E_y = \frac{-\partial\Phi(x, y)}{\partial y} = \frac{2}{r_0^2} (U + V \cos(\omega t)) y \quad (3.35)$$

$$E_z = \frac{-\partial\Phi(x, y)}{\partial z} = 0 \quad (3.36)$$

Newton's second law, e.g. $F_x = eE_x = m \frac{d^2x}{dt^2}$ provides the equations of motion:

$$\frac{d^2x}{dt^2} + \frac{2e}{mr_0^2} (U + V \cos(\omega t)) x = 0 \quad (3.37)$$

$$\frac{d^2y}{dt^2} - \frac{2e}{mr_0^2} (U + V \cos(\omega t)) y = 0 \quad (3.38)$$

$$\frac{d^2z}{dt^2} = 0 \quad (3.39)$$

Relationship (3.39) supports the statement of section 3.2.2, namely that there is no further acceleration along the quadrupole axis. Only the kinetic energy of the molecule entering the ion source and the setting of the energy electrode determine finally the velocity of the ion passing the quadrupole. The following dimensionless substitutions bring the differential equations (3.37 and 3.38) in an analytically well investigated form:

$$\xi = \frac{\omega t}{2} \quad (3.40)$$

$$a_\mu = \frac{8eU}{m\omega^2} \cdot \gamma \quad (3.41)$$

$$q_\mu = \frac{4eV}{m\omega^2} \cdot \gamma \quad (3.42)$$

The placeholder μ represents either x or y , and γ stands for σ and λ respectively. The parameter a_μ scales linearly with the impressed **DC** voltage U and q_μ with the **RF** voltage V . Substitution of these expressions into (3.37 and 3.38) leads to a

special type of linear second-order differential equation that is known as the Mathieu equation:

$$\frac{d^2\mu}{d\xi^2} + (a_\mu + 2q_\mu \cos 2\xi)\mu = 0 \quad (3.43)$$

The Mathieu equation is the fundamental equation for the quadrupole operation. It has stable solutions, i.e. $|\mu|$ does not exceed r_0 for any ξ and it has unstable solutions where the opposite happens. Stable solutions can be expressed as [96, page 67]:

$$\mu(\xi) = \alpha' e^{i\beta\xi} \sum_{n=-\infty}^{\infty} C_{2n} e^{2in\xi} + \alpha'' e^{-i\beta\xi} \sum_{n=-\infty}^{\infty} C_{2n} e^{-2in\xi} \quad (3.44)$$

α' and α'' are integration constants and depend on the initial conditions μ (entrance position of the ion), $d\mu/dt$ (entrance velocity of the ion perpendicular to z) and the **RF** phase angle ωt_0 . C_{2n} and β are functions of a and q . Equation (3.44) states, that the ion performs a periodical motion which leads together with the motion along z to a helical flight path through the quadrupole. The performance of a quadrupole mass filter is usually illustrated by a stability diagram as shown in Figure 3.10:

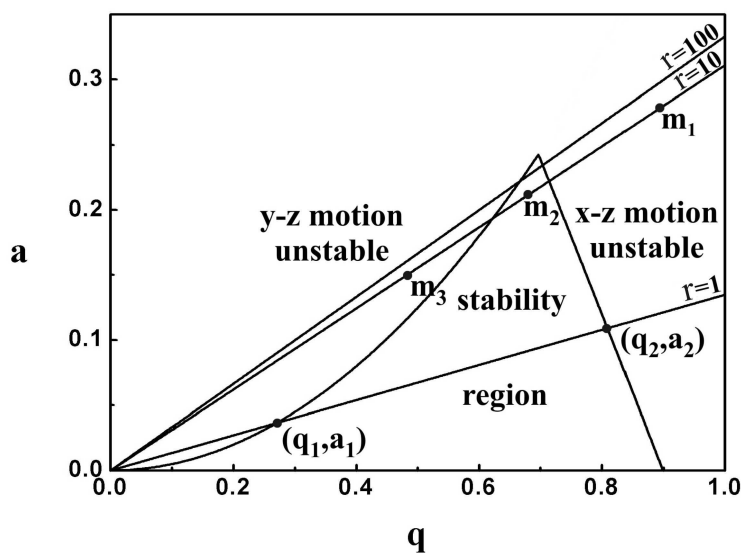


Figure 3.10: The (a, q) stability diagram of a quadrupole mass filter and mass-scan lines for different resolutions, adopted from [95], changed

There is a region in a, q space where the ion performs a stable $x - z$ motion but an unstable $y - z$ motion and vice versa. Both motions are stable within the triangular region. A straight line crossing the origin and the stability region is called a mass scan line. The slope s of this line depends on the ratio between the **DC** and **RF** voltage:

$$s = \frac{2U}{V} = \frac{a}{q} = \frac{\Delta a}{\Delta q} = \frac{(a_2 - a_1)}{(q_2 - q_1)} \quad (3.45)$$

The values Δa and Δq represent the differences between the points of intersection, (q_1, a_1) and (q_2, a_2) , of the mass scan line and the stability region. The values a and q are the respective mean values between the stability limits. As a result, the mass resolution r can be calculated as follows:

$$r = \frac{m}{\Delta m} = \frac{a}{\Delta a} = \frac{q}{\Delta q} \quad (3.46)$$

Equation (3.46) implies that the maximum mass resolution is realized near the apex of the stability region. A mass spectrum at the desired resolution is obtained by scanning the absolute values of U and V in such a manner that their ratio remains constant. Higher-mass ions are brought into the stability region from left to right, that is $m_3 > m_2 > m_1$.

The foregoing discussion is valid for an ideal quadrupole consisting of infinitely long hyperbolic electrodes generating a perfect field. Under these conditions, any ion in the stability region has a stable flight path through the quadrupole independent from its incident angle and velocity. In practice, hyperbolic electrodes are frequently approached by round rods of finite length that lead to field imperfections and impose certain limitations. More precisely, a real quadrupole shows a dependence of peak profile and peak maximum on the entrance conditions of the ion. These dependencies are of special importance if a molecular beam interface is used for injection.

3.2.4 Ion Detection

The ion current that has to be detected is in the range of 10^{-8} to $10^{-16} A$ [97]. These small currents make special detection devices necessary. Currents at the upper end of the given range can be measured by direct collection of the ions without pre-amplification. This current causes a voltage drop on a high ohmic resistance that can be amplified and registered. To prevent any ion loss and escaping of secondary electrons the collecting electrode has a cup-like shape, leading to the denotation ‘Faraday Cup’ for this kind of detector [Figure 3.11]:

The big advantage of this comparably simple detector is its temporal stability and lack of mass discrimination. Disadvantageous are its slowness and poor sensitivity.

Highly sensitive and fast measurements require pre-amplification of the ion current before detection. This can be achieved with a **S**econdary **E**lectron **M**ultiplier (**SEM**)

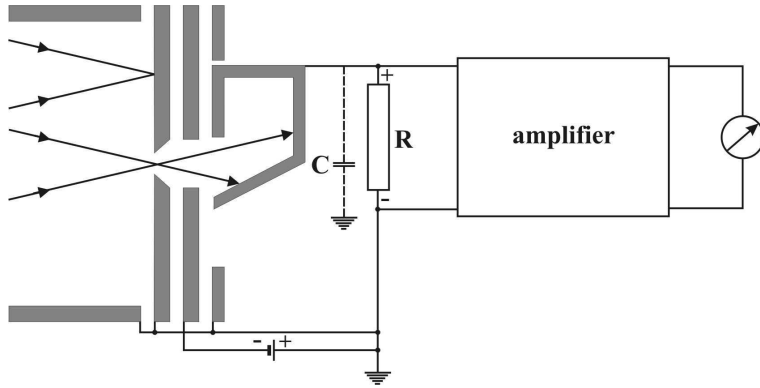


Figure 3.11: Schematic diagram of a Faraday Cup, adopted from [97, page 113]

[Fig. 3.12]. After passing an accelerating potential, the ions hit the first dynode and

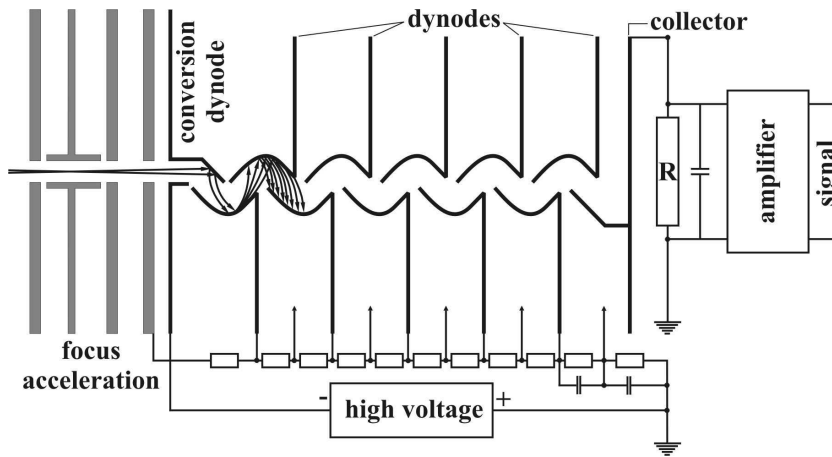


Figure 3.12: Schematic diagram of a SEM, adopted from [97, page 120], changed

excite a number of secondary electrons. As this dynode converts an ion current into an electron current it is named ‘conversion dynode’. Due to the potential drop between the conversion dynode and the following ones the formed electrons are accelerated at a time towards the next dynode each releasing off new secondary electrons. The amplification A of a **SEM** can be calculated according to:

$$A = N_{cd} \cdot N_d^n \quad (3.47)$$

N_{cd} is the number of electrons released by an ion striking the conversion dynode. N_d is the number of electrons released by an electron hitting the next dynode in the potential cascade of altogether n dynodes. Depending on the electrode material (typically CuBe or Al) and the length of the cascade, amplifications of 10^7 are easily reached. The amplified current makes a high input resistance dispensable which facilitates a small time constant and hence very fast measurements. The yield of conversion electrons per impinging ion depends on the ion’s mass, charge, energy and

electronic configuration. The mass discrimination caused by these effects is a decisive drawback of the **SEM** as it complicates any quantification. However, qualitative and relative measurements are possible, absolute quantification can only be done after calibration with pure components. The amplification of electrons within the dynode cascade is a very fast process compared to the emission from the conversion dynode. Hence, each impinging ion causes a voltage pulse whose height differs significantly from a noise pulse. Electronic counting of pulses above a certain level facilitates measurements of extremely small currents ($< 10^{-16} A$). The mass spectrometer used here allows measurements in this so called 'Pulse Ion Counting = **PIC**'- mode.

For mass spectrometric use, continuous dynode multipliers are more widely spread than discrete ones [98]. These so called **Channel Electron Multipliers (CEM)** consist of a special lead silicate glass tube frequently in form of a horn. Treatment of this glass in a hydrogen atmosphere leads to the formation of a multilayer surface combining a secondary electron emissive layer with a resistive one that is used to apply the pole bias. Their mode of operation is analog to the **SEM** but they are not as sensitive to frequent atmosphere exposure.

3.3 Threshold Ionization - Appearance Potential Measurements

3.3.1 Discrimination Principle - Ionization Potentials, Appearance Potentials

The question of intermediates is of particular importance for any mechanistic interpretation of a chemical reaction. As molecular beam sampling mass spectrometry allows an in-situ investigation of the gas phase in a heterogeneously catalyzed reaction the question arises if this technique can be used to identify short-lived gas phase intermediates which can not be observed by conventional ex-situ **MS** or **GC** monitoring. As reviewed briefly in the introduction the detection of radicals tested indeed possible (at least for low pressures) using the threshold ionization technique to discriminate between radicals and fragments of stable molecules. This discrimination principle is as follows:

If an electron (e^-) possesses the energy E and hits a molecule (XY), ionization and dissociation takes place with a certain probability P according to equations (3.48) and (3.49) respectively:



$$P_i(E < IP(XY)) = 0, P_i(E \geq IP(XY)) = f_i(E)$$



$$P_d(E < AP(X^+)) = 0, P_d(E \geq AP(X^+)) = f_d(E)$$

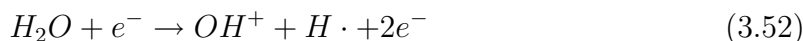
IP means here the ionization potential of the molecule XY and AP is the appearance potential of the fragment X^+ . If one wants to detect the radical $X\cdot$ in presence of the molecule XY one has to make use of its lower ionization energy compared to the appearance potential of X^+ from XY . It can be shown by means of thermodynamics, that the ionization potential of $X\cdot$ is always lower than the appearance potential of X^+ from XY by an amount equal to the dissociation enthalpy of the $X-Y$ bond [34]:

$$AP(X^+/XY) = \Delta_d H(X-Y) + IP(X\cdot) \quad (3.50)$$

As an example, $OH\cdot$ radicals ($=X\cdot$) need to be detected besides H_2O molecules ($=XY$):



$$P_i(E < 13.18 \text{ eV}) = 0, P_i(E \geq 13.18 \text{ eV}) = f_i(E)$$



$$P_d(E < 18.2 \text{ eV}) = 0, P_d(E \geq 18.2 \text{ eV}) = f_d(E)$$

A mass spectrum of such a mixture recorded at an electron energy between 13.18 eV [99] and 18.2 eV [100] shows a peak at 17 amu only if $OH\cdot$ radicals are present. At higher energies OH^+ fragments contribute to the signal governing finally the intensity as the concentration of H_2O is orders of magnitude higher than the concentration of the reactive $OH\cdot$ radicals.

Any comparison with literature data on ionization and appearance potentials has to be done with caution as the values depend on how they have been determined. The formal definitions of both potentials include that all involved entities are in their ground states. Due to the Franck-Condon principle, electron impact ionization leads

frequently to excited molecular ions and neutral fragments so that the measured ‘vertical’ IP and AP values might differ from the ‘adiabatic’ ones. They are usually somewhat higher than those found using optical spectroscopy [101, chapter 3].

3.3.2 Ionization Efficiency Curves

If one measures the variation of the intensity of an ion as a function of the energy of the ionizing electrons one obtains a so called ‘ionization efficiency curve’. Figure 3.13 shows measured Ionization Efficiency (**IE**)-curves for methane and its fragments.

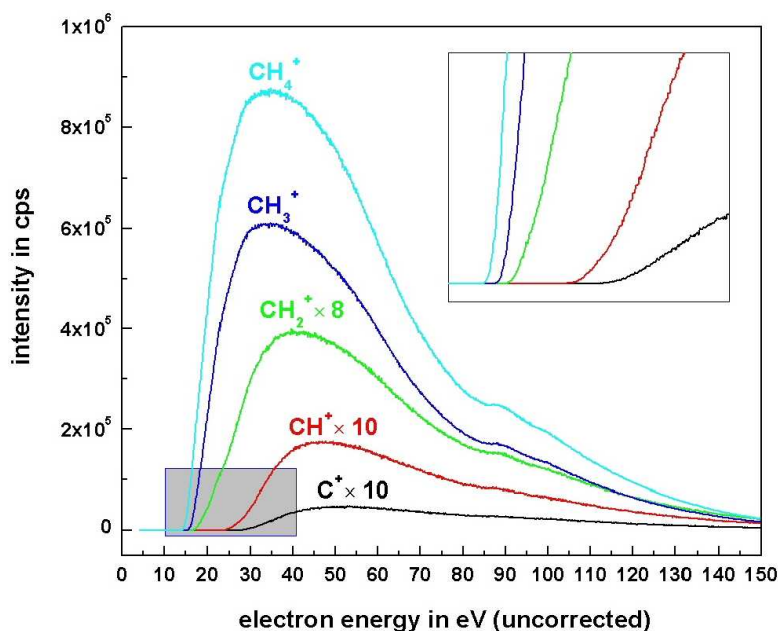


Figure 3.13: **IE**-curves of CH_4^+ at 16amu, CH_3^+ at 15amu, CH_2^+ at 14amu, CH^+ at 13amu and C^+ at 12amu

IE-curves of different molecules resemble each other. They start with a curved portion for the first volts above the ionization- or fragmentation threshold. Attached is a variably extended linear part that meets in a broad maximum between 30 and 100 eV. This is the reason why most of the conventional ion sources work at about 70 eV. Increasing the electron energy further leads to a monotonic decrease in signal intensity. The different processes leading to this frequently observed shape can qualitatively understood as follows [101, chapter 2].

If the electron does not possess sufficient energy, collision does not lead to an ionization. Just at the threshold, ionization can occur only if the electron strikes the atom (molecule) exactly at its center. In this case, both the expelled electron as well as the impinging electron do not have excess kinetic energy and the capture of one of the electrons is very likely. Not until the electron energy exceeds the threshold

value the escape process of the electrons from the coulomb field of the ion becomes feasible leading to a measurable degree of ionization. It is the probability of the escape process that scales nearly linearly with the excess energy causing the linear portion of the **IE**-curve as will be outlined in Section 3.3.3. The curvature observed in case of a sharp onset is at least for the single ionization process due to the spread within the electron energy distribution. An experimental verification of the size of this effect is given in Section 3.3.4. As one can see in Figure 3.13, the extent of the curvature increases and the linear portion of the **IE**-curve decreases if the ion results from the more complicated fragmentation process.

If the electron energy increases above the threshold the total ionization cross section increases as henceforth not only exact but also aslant collisions succeed. This holds true as long as there is a frequency in the Fourier spectrum of the electron wave packet that can excite the electron by resonance. If the electron energy becomes higher and higher the spread of the corresponding wave packet becomes smaller and contains more and more high frequency oscillations not suitable to interact with the electron wave function. This finally causes the gradual decline of the ionization efficiency after the maximum.

Additionally to these more general features, processes like vertical transitions to electronically and vibrationally excited states, auto-ionization, ion pair formation and fragmentation onsets cause a fine structure in the **IE**-curve. Most of the literature on electron impact ionization is on measuring and assigning of this fine structure. As this was not the objective of the present work the considerations in the following sections are restricted to threshold behavior.

3.3.3 Threshold Behavior - Predictions from Theory

Ionization of Atoms

The theoretical treatment of electron impact ionization is exceedingly demanding as it is a many body problem. The quantum mechanical treatment of two continuum electrons in the field of an ionized atom has not yet been satisfactorily accomplished [102]. Fortunately Wigner [103] formulated as early as in 1948 the idea, that the cross section behavior of a two body interaction near the threshold depends only on the long range interaction between the involved particles and not on the reaction mechanism

itself. He applied his theory to processes like particle scattering or capture. These statements led Wannier [104] to apply this concept to electron impact ionization, even though this is in fact a three particle process. It turned out that the final escape of the two outgoing electrons might be separated from the reaction itself which is confined to a small ‘reaction zone’. The threshold behavior is the result of the escape process, namely, lack of kinetic energy for complete escape. This feature is amenable to calculation even when the reaction itself is not. To do so, he described the ionization event by means of three different regions. Adjacent to the reaction zone itself which is not further considered is the so called Coulomb zone within which the small excess energy just makes up for the negative potential energy due to Coulomb attraction. Attached to that is the free region in which the excess energy is still the kinetic energy of the electrons. The ion is sufficiently heavy and is considered stationary during the reaction. Such a simplified model can be treated classically solving the corresponding equations of motion. The analysis showed that the escape process is only possible if the electrons depart at equal distances in opposite directions. For single ionization Wannier obtained the following threshold law:

$$Q_i^+ \sim (E - IP)^{\left(\frac{1}{2}\mu - \frac{1}{4}\right)} \quad (3.53)$$

Q_i^+ is the total cross section for single ionization. The exponent μ scales with the charge of the remaining ion z according to:

$$\mu = \frac{1}{2} \left[\frac{(100z - 9)}{(4z - 1)} \right]^{\frac{1}{2}} \quad (3.54)$$

Inserting Equation (3.54) in (3.53) supplies $\mu = 1.127$, 1.056 or 1.036 as exponent for a singly, doubly or triply positively charged ion respectively. The departure from linearity results from the electron-electron interaction. As one can see, the exponent approaches unity with increasing charge as the core Coulomb forces surpass the Coulomb interaction between the electrons.

The two-electron photoionization of H^- ions (Eqn. 3.55) can be considered the simplest system to check up on Wannier’s theory. This has been done by Donahue and coworkers [105, 106].



They obtained an exponent of $\mu = 1.15 \pm 0.04$ which is in agreement with the Wannier law. A real electron impact experiment on $H\cdot$ has been conducted by McGowan and

Clarke [107]:



Again in agreement with Wannier, they found a power law with an exponent of $\mu = 1.13 \pm 0.03$ fitting their experimental data best up to 0.4 eV above the threshold. This result gives a first impression on the energy range in which the Wannier law is applicable. At higher energies a linear law was in better agreement with the data. Within reference [107] considerable effort had been made to determine shape and width of the energy distribution of the ionizing electrons. They found a Gaussian distribution with a **FWHM** = 0.04 eV. This value, typical for apparatus designed to perform ionization- and appearance potential measurements is cited here as it shall be compared in the next section with the value determined in this work. Of more practical importance for the present work are results for helium (3.57) and argon (3.58):



These gases were used in this work to calibrate the energy axis and to determine the convolution function of the spectrometer. Helium is particularly suited as a reference because the single charged He^{+} ion has no energy levels within some 40 eV above the ionization potential [108, page 7]. Numerous investigations have been published on the threshold behavior of the rare gases. In the case of helium most of them describe a nonlinear behavior near threshold sometimes in agreement [109, 110, 111], sometimes in disagreement [112] with the Wannier law. Other studies find a linear law fitting better than a power law [113, 114]. Likewise to helium, argon is suited for calibration and determination of the energy spread function. The first excited state (${}^2P_{1/2}$) of the Ar^{+} ion is just 0.18 eV above the ground state (${}^2P_{3/2}$) and can not be resolved with the machine available. The second excited state (${}^2S_{1/2}$) lies 13.48 eV above the ground state [108, page 216] and provides thus the opportunity to fit the threshold curvature to a proper spread function as described in Section 3.3.4.

Not only singly but also doubly positively charged ions were observed in the recorded mass spectra. Also the process of double ionization has been tackled theoretically [115, 116, 117, 118]. Neglecting electron-electron interactions, references [115] and [116] predict consistently a threshold law according to Equation (3.59). The

exponent μ equals here the number of expelled electrons ($\mu = 1, 2, \dots$):

$$Q_i^{\mu+} \sim (E - IP)^\mu \quad (3.59)$$

In reference [117] and [118], electron-electron interactions were taken into account and the exponent for double ionization was found to be $\mu = 2.270$ for $z = 2$ after ionization. The experimental verification of the theory for μ -fold ionization is a highly challenging task as the experiments suffer from the extremely small cross sections. In addition Equation (3.59) applies for each ionic state of the atom or molecule populated in the process of ionization. Larger ions and molecules possess many of such states already a few *eV* above the threshold value. As an example, Ar^{++} has four of them ($^3P_1, ^3P_0, ^1D_2, ^1S_0$) with the highest just 4 *eV* above the ground state (3P_2) [108, page 216]. All these states open new ionization channels leading to a gradual increase of the ionization cross section [119, 120]. In conclusion, the number of possible states and the convolution with the electron energy distribution lead to a very broad curvature providing at best an averaged power law [121]. The ideal system to verify on the theoretical predictions is the double ionization of helium:



There is only one state of He^{++} and complications due to overlapping processes would be avoided. Unfortunately it proved impossible to measure a satisfactory **IE**-curve because the absolute probability for double ionization is low and there is a severe interference from the process $H_2 + e^- \rightarrow H_2^+ + 2e^-$. The conclusion for this work is, that doubly charged ions can not be exploited neither to determine the convolution function nor to calibrate the energy axis.

Ionization of Molecules

As mentioned several times, the aim of the appearance potential technique is to discriminate between molecular ions according to their different ionization- or appearance potentials. To identify the chemical species that has the lowest ionization- or appearance potential on a given mass, it is sufficient to determine the onset value of the respective **IE**-curve. High energetic intermediates like radicals and unstable molecules fulfill this condition in the majority of cases, making their identification

straightforward. Any other interpretation requires the analysis of the fine structure within the curve, a challenging task for atoms but even more difficult for ions.

Electron impact ionization leads to vertical transitions to vibrational levels of the molecular ion according to the Franck-Condon principle. This together with Wannier's law led to the expectation that a series of straight line segments should be observed in the threshold region with the onset of each new segment representing a transition to a new vibrational level [122]. The successive slope increases were interpreted as relative Franck-Condon factors. As discussed extensively in a review on measurement of ionization and appearance potentials [39] this works only in exceptional cases by using monochromatized electrons. In the majority of cases, processes like direct ionization, ion pair formation and auto-ionization, each having its own threshold law, occur successively or in parallel and cause more complex features in the **IE**-curve. This is already the case for simple molecules like N_2 , O_2 or CO [123]. The number of accessible electronically and vibrationally excited states increases rapidly as the molecule becomes more complex, making the consistent interpretation of its **IE**-curve finally impossible.

Fragmentation of Molecular Ions

The situation is similarly intricate if fragmentation comes into play. As will be discussed in Section 3.3.4, most of the methods employed to analyze **IE**-curves rely on linear or power threshold laws for the ionization probability [124]. Application of these laws to fragmentation processes has not been successful as the relationship between fragmentation probability and electron energy is by far more complex and not representable in a simple form like (3.59).

For diatomic molecular ions it is again the Franck-Condon principle that helps to describe the fragmentation behavior [125]. The idea is that ionization produces vertical transitions from the molecule ground state to the various ion electronic states and that, depending on the electron energy and the shape and location of each of the ion potential curves, one would observe characteristic yields of fragment ions with characteristic kinetic energy distributions [126, 127]. The exact knowledge of the electronic and vibrational states that is required to apply this method can be derived from quantum mechanical calculations or spectroscopic measurements. In

principle, the mass spectrometer used for this work allows the measurement of ion kinetic energy distributions. As a direct ionization of a radical does not increase its kinetic energy such measurements could corroborate the classical appearance potential measurements. This possibility has not been exploited up to now but will be in the future.

For small symmetrical molecules like CH_4 or NH_3 the Wigner-Witmer rules [128] have been applied successfully to correlate the electronic states of parent ion and fragments [129]. For manageable cases such correlations are useful to interpret appearance potential measurements. The fragmentation behavior of more complex molecules like for example small hydrocarbons can be anticipated on the bases of a statistical approach, the so called ‘quasi-equilibrium’ theory of Rosenstock, Wallenstein, Wahrhaftig, and Eyring [130]. According to this theory, which is build on principles of statistical mechanics, the fragmentation processes can be considered separately from the ionization. The molecular ion, possessing a certain amount of electronic and vibrational energy, may not dissociate within the time of one vibration, but instead it can rapidly and randomly distribute this energy among the various vibrational and rotational modes (‘quasi-equilibrium’). It may undergo unimolecular decomposition along energetically available paths if it can attain certain configurations with sufficient vibrational energy concentrated in the proper modes. A fragmentation chain is than described as a series of competing, consecutive unimolecular reactions. The rate constants for these unimolecular reactions and hence the fragmentation pattern and its energy dependence can be calculated by means of activated complex theory. With a mass spectrometer, fragmentation products are analyzable if the dissociation takes place within several microseconds (residence time in the ion source). The ‘quasi-equilibrium’ theory provides the result that the excess energy necessary to reduce the lifetime in the order of a microsecond increases with the number of internal degrees of freedom of the molecular ion. The mathematics behind this theory is quite demanding but by making several simplifying assumptions, the following equation (3.61) is derived for the rate constant k of a particular decomposition:

$$k = \left[\frac{(E - E_{min})}{E} \right]^{N-1} \frac{\prod_{i=1}^N \nu_i}{\prod_{j=1}^{N-1} \nu_j^\ddagger} \quad (3.61)$$

E is the total energy minus the zero-point energy of the molecular ion, E_{min} the minimum energy required for the decomposition, N the number of oscillators in the molecular ion, and ν_i and ν_j^\ddagger the vibrational frequencies of the molecular ion and of the activated complex, respectively. Rotation terms are neglected in this formula. The success of the statistical theory in predicting mass spectra varies from case to case [131]. It turned out that the theory is qualitatively correct for numerous dissociative processes well above the threshold but quantitatively often inadequate in the energy range near the threshold. Notwithstanding these deficiencies, the important information for the present work is, that ionization efficiency curves for a fragment ion approach the energy axis with curvature, quite apart from any effect resulting from energy spread in the electron beam. This is confirmed looking at Figure 3.13 for CH_4 fragmentation. Stripping off the hydrogen atoms is a series of consecutive unimolecular reactions and the curvature becomes more and more pronounced for higher fragments. As a conclusion it would be pointless to fit a threshold power law to appearance potential data. This can only be done for single or multiple ionization as in the next section for helium, which was used to determine the energy spread function.

3.3.4 Evaluation of Ionization Efficiency Data

The aim of the preceding section was to describe the threshold behavior of ionization and dissociation processes. The conclusion was that any interpretation of **IE**-curves beyond the determination of the corresponding threshold values requires both, high quality ionization efficiency data and considerable background from theory. As already mentioned, radicals and instable molecules have mostly lower IP's and AP's than the interfering species, allowing for an identification by comparison with tabulated values. Nevertheless, the determination of threshold potentials by electron impact is anything but simple. Reasons for that are [40]:

- energy spread of the ionizing electrons
- small cross sections at threshold energies
- overlapping ionization processes

- no universally valid threshold law

Various methods are described in literature to determine threshold values from **IE**-curves measured using energetically inhomogeneous electrons [132]. All methods operate with pure substances and in presence of an internal standard with known ionization potential to correct the energy axis for instrumental effects. The standard, usually helium or argon is introduced into the ion source together with the gas under investigation. The methods differ in the way they treat the curvature at the onset of the **IE**-curve. In the ‘linear extrapolation method’ [133], the straight line portion of the curve is extrapolated to the energy axis and the point of intersection is taken as ionization or appearance potential respectively. As discussed in the previous section, the extent of curvature varies considerably according to the underlying process, which leads often to values that are appreciably higher (some eV) than the adiabatic one. Another widespread method proposed originally by Honig [134], is the so called ‘critical slope method’. This approach tries to obviate the difficulties inherent in the linear extrapolation method. Assuming a quadratic power threshold law, Honig showed mathematically that a plot of the logarithm of the ion current against the electron energy is a curve that approximates a straight line for small excess energies and has a slope of $2/(3kT_{filament})$ at the ionization potential. This method provides ionization potentials that are generally in good agreement with spectroscopical ones [135], but it does not work for appearance potentials. The method is not applicable here as the filament temperature is not accessible. Likewise good results for both ionization and appearance potentials are obtainable using the ‘vanishing current method’ [136]. Here, the ionization efficiency curve for the ion under investigation is examined, and the electron voltage corresponding to the first formation of ions is taken to be the threshold value. The great asset of the vanishing current method is that the critical potentials approach the ‘true’ adiabatic values best, particularly if an appreciable curvature is the result of the nature of the ionization process. The main objection against the method is, that the choice of the onset value is quite subjective and depends somewhat on the sensitivity used in obtaining the curve. The vanishing current method has been applied throughout this work and the values found were in good agreement to literature values within the accuracy of the measurements. This leads over to the last section in the background part, the estimation of the experimental error involved in a threshold value determination.

3.3.5 Determination of the Electron Energy Spread Function

The HAL4 EPIC Low Energy mass spectrometer is equipped with an ion source which supplies energetically inhomogeneous electrons. The energy spread is caused by different reasons:

- heated filament \rightarrow thermal energy spread
- potential drop along the filament
- potential gradients inside the source
- filament contaminations
- contact potential between filament and source chamber

Being U the thermal energy of an electron and V the energy it gains by acceleration in the electric field, its total energy E can be expressed as a sum of both:

$$E = U + V \quad (3.62)$$

If one now subsumes all the ill-defined contributions (potential drops etc.) in the thermal energy term leaving V to be the applied potential, one can define an energy spread function $m(U)$ in eV^{-1} describing the energy distribution of the ionizing electrons. Now, $m(U)dU$ is the number of electrons with energy between $V + U$ and $V + U + dU$. This number multiplied with the ionization (fragmentation) probability $P_{i,(d)}(E)$ is proportional to the measured ion current according to Equation (3.63), with C being the constant of proportionality:

$$i(V) = C \cdot \int_{IP}^{\infty} m(E - V) P_{i,(d)}(E) dE \quad (3.63)$$

$i(V)$ is the ion current at a certain m/z ratio measured if the voltage V is applied between filament and cage. If one restricts to single ionization, $P_i(E)$ is given by Wannier's threshold law:

$$P_i(E) = (E - IP)^{1.127} \quad (3.64)$$

In the first instance, the exact form of $m(E - V) = m(U)$ is unknown as the filament temperature and the potential gradients inside the ion source are unknown. Due to

the thermal nature of the electrons a Maxwellian energy spread function might be a reasonable choice ($m(U)$ in eV^{-1} , U in eV , k in J/K , T in K):

$$m(U) = 1.6 \cdot 10^{-19} \cdot \frac{2}{\sqrt{\pi}} \cdot \left(\frac{1}{kT}\right)^{\frac{3}{2}} \cdot \sqrt{1.6 \cdot 10^{-19} \cdot U} \cdot e^{-\left(\frac{1.6 \cdot 10^{-19} \cdot U}{kT}\right)} \quad (3.65)$$

On the other hand, potential gradients inside the source may be more prominent than the thermal spread causing a different spread function, possibly of Gaussian type ($m(U)$ in eV^{-1} , U in eV , σ in eV):

$$m(U) = \frac{1}{\sigma \cdot \sqrt{2\pi}} \cdot e^{-\frac{U^2}{2\sigma^2}} \quad (3.66)$$

The width of the Maxwellian distribution depends on the temperature T , that of the Gaussian on the standard deviation σ . Independent of the shape, any chosen spread function has to fulfill Equation (3.67):

$$\int_{-\infty}^{+\infty} m(U) dU = 1 \quad (3.67)$$

The following attempt to obtain the underlying spread function bases on the work of Morrison [137]. Differentiation of the convolution integral (3.63) with respect to the nominal energy V results in:

$$\frac{di(V)}{dV} = C \int_{IP}^{+\infty} \frac{\partial m(E - V)}{\partial V} P_i(E) dE = -C \int_{IP}^{+\infty} \frac{\partial m(E - V)}{\partial E} P_i(E) dE \quad (3.68)$$

The substitution of ∂V by $-\partial E$ is based on the following relationship:

$$\frac{\partial m(E - V)}{\partial V} = -\frac{\partial m(E - V)}{\partial E} \quad (3.69)$$

Integration by parts yields:

$$\frac{di(V)}{dV} = -C \cdot m(E - V) P_i(E) \Big|_{IP}^{\infty} + C \int_{IP}^{+\infty} m(E - V) \frac{dP_i(E)}{dE} dE \quad (3.70)$$

As $P_i(IP) = 0$ and $m(E - V) \rightarrow 0$ if $E \rightarrow \infty$, the first term vanishes. Using $P_i(E) = (E - IP)^1$ as an approximation for the single ionization threshold law one obtains with $dP_i(E)/dE = 1$:

$$\frac{di(V)}{dV} = C \int_{IP}^{+\infty} m(E - V) dE \quad (3.71)$$

Calculation of the second derivative leads to:

$$\frac{d^2i(V)}{dV^2} = C \int_{IP}^{+\infty} \frac{\partial m(E - V)}{\partial V} dE = -C \int_{IP}^{+\infty} \frac{\partial m(E - V)}{\partial E} dE \quad (3.72)$$

Evaluation of this integral gives the electron energy distribution, reversed with respect to the energy scale:

$$\frac{d^2i(V)}{dV^2} = -C \cdot m(E - V) \Big|_{IP}^{\infty} = C \cdot m(IP - V) \quad (3.73)$$

The height of the distribution depends on the proportionality constant C and the ionization potential corresponds to the sharp cutoff in case of the Maxwellian, or to the maximum in case of the Gaussian distribution.

To verify this analytical derivation, Equation (3.63) has been calculated for helium ionization ($IP = 24.56 \text{ eV}$ [138]) using both a Maxwellian and a Gaussian spread function. Both functions were arbitrarily adjusted to $\mathbf{FWHM} = 1 \text{ eV}$ corresponding to $T = 6500 \text{ K}$ or $\sigma = 0.425 \text{ eV}$. C has been chosen as $1 \text{ cps} \cdot \text{eV}^{-1}$. The simplified linear threshold law was inserted for $P_i(E)$. Figure 3.14 shows that Morrison's method works for the simulated data. The spikes in the derivatives of Equation (3.63) using a Maxwellian spread function as $m(E - V)$ are due to rounding errors during the numerical integration.

Application of this method to real measured data reveals two problems, namely, the nonlinear threshold law and the presence of experimental noise which would be strongly amplified by differentiation. The influence of the nonlinearity has been tested using Equation (3.64) for the simulation (Fig. 3.15). The nonlinearity causes a slight distortion of the results. For the Gaussian distribution the \mathbf{FWHM} becomes about 0.05 eV larger than with strict linearity. The Maxwellian distribution with its distinct high energy tail comes out with a reduced \mathbf{FWHM} of 0.94 eV . The ionization potential is influenced marginally. For the Gaussian it is shifted from 24.56 eV to 24.62 eV . The sharp Maxwellian cutoff can hardly be determined as it is blurred by the nonlinearity.

The experimental noise requires smoothing of the raw data which causes an increase of the spread as smoothing is in fact an additional convolution. The results of Morrison's method for measured data on the standards He and Ar are shown in Figure [3.16] using a 5 point \mathbf{FFT} filter for smoothing. Fits of the second derivatives

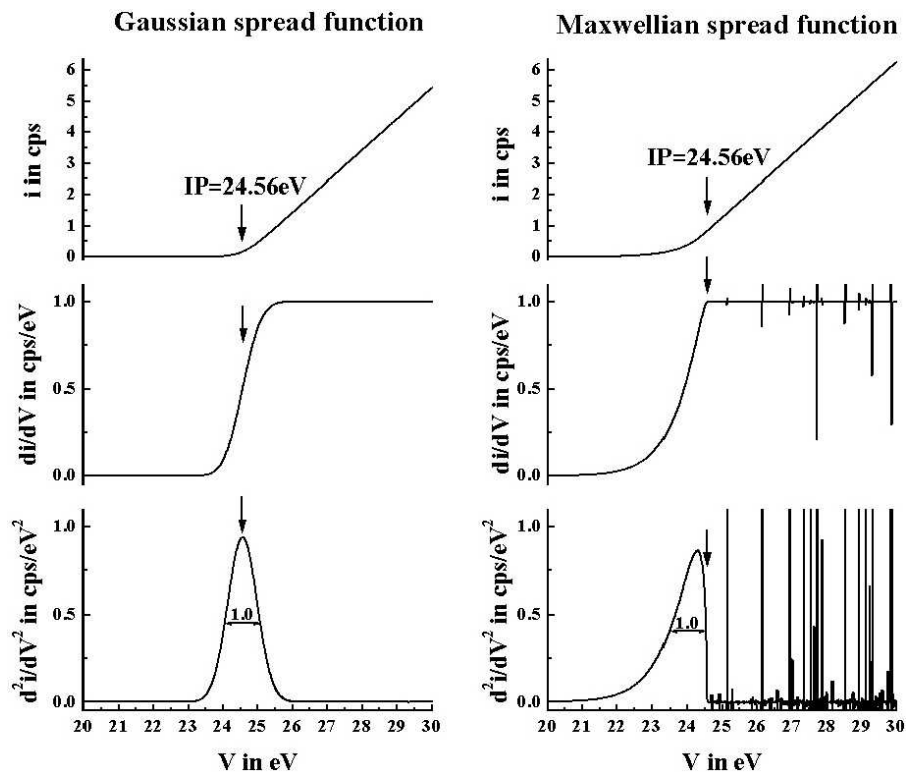


Figure 3.14: Determination of the energy spread function using Morrison's differential method applied to a linear threshold law for helium ionization

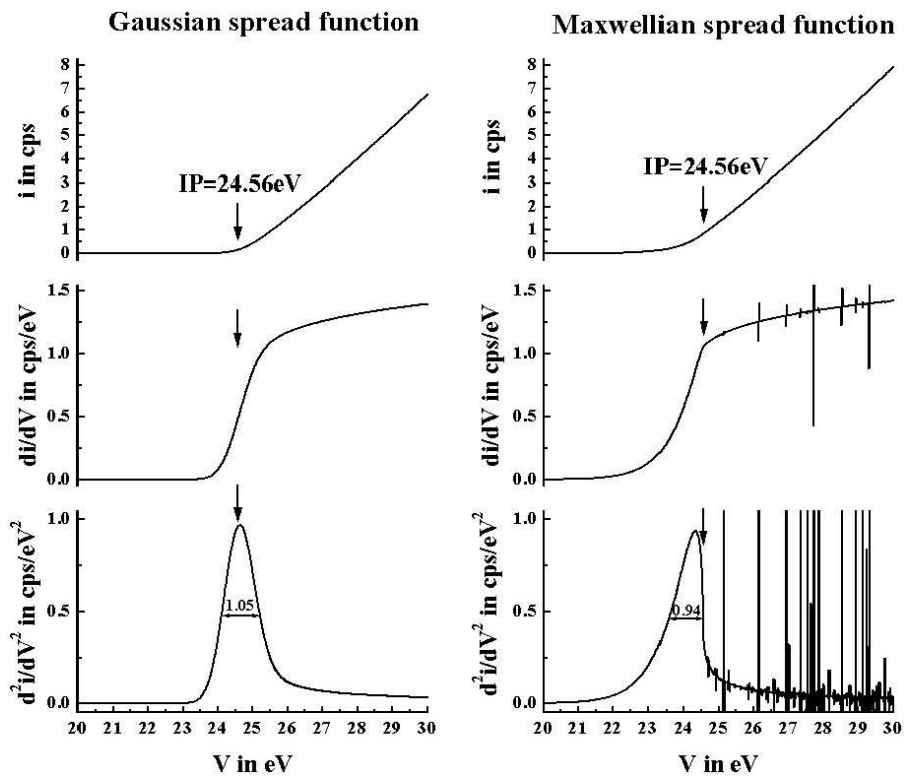


Figure 3.15: Determination of the energy spread function using Morrison's differential method applied to Wannier's nonlinear threshold law for helium ionization

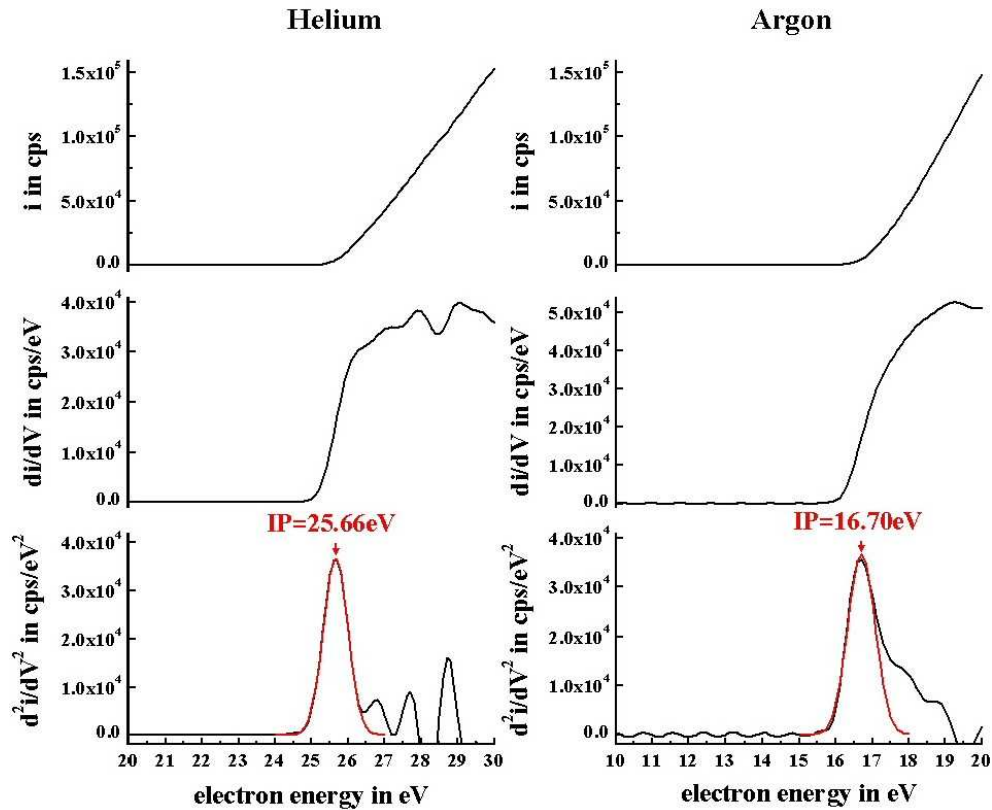


Figure 3.16: Application of Morrison's differential method to smoothed IE -curves of He and Ar , the red curves show the results for Gaussian fits

reveal that the spread function is better described by a Gaussian than a Maxwellian distribution. This leads to the conclusion that potential gradients inside the ion source cause an energy spread in addition to thermal spread which would be purely Maxwellian like. The ionization potentials obtained by this method for Ar (16.7 eV) and He (25.7 eV) are about 1 eV higher than those found in the literature (15.82 eV and 24.56 eV [138]). This is not surprising as the displayed energy of the spectrometer unit has not necessarily to agree with the true one. For a standardization it is much more important that the measured difference of 9.0 eV corresponds to the literature value of 8.74 eV. The portion of additional spread caused by the smoothing procedure was revealed by varying the number of points of the **FFT** filter. It turned out, that already a 5 point smoothing increases the spread by some tenth of an eV. An influence on the shape of the spread function was not observed. In consequence of nonlinearity and smoothing it seems not advisable to take the ionization potential and the energy spread by Morrison's method. However, at least the shape of the spread function could be obtained from this analysis. With the shape known, a

direct fitting of the convolution integral (3.63) is possible:

$$i(V) = C \cdot \int_{IP}^{\infty} m(E - V) P_i(E) dE = \frac{C}{\sigma \cdot \sqrt{2\pi}} \int_{IP}^{\infty} e^{-\frac{(E-V)^2}{2\sigma^2}} (E - IP)^{1.127} dE \quad (3.74)$$

The quality of the fit was evaluated by visual inspection as the integral equation (3.74) could not be used by a nonlinear fitting module. Figures 3.17 and 3.18 show the results for helium and argon. A fitting by visual inspection is of course somewhat subjective. Nevertheless it can be done sufficiently well as the parameters of the fit C , IP and σ are only marginally correlated and can be adjusted one by one. Figure 3.19 illustrates this fact by showing fits for the argon curve each with a significant change in one parameter and the others kept constant.

Variation of the slope C affects only the upper part of the curve leaving the onset unchanged. Contrary, the spreading given by σ influences only the curvature at the onset. Finally variation of the ionization potential causes a parallel shift of the whole curve to the left or to the right. The ionization potentials derived from the fits are in good agreement with the values from Morrison's differential method and their difference of 8.80 eV is even closer to the literature value of 8.74 eV. The width of the energy spread function seems to be higher for *Ar* ($\sigma = 0.42$ eV) than for *He* ($\sigma = 0.28$ eV). There might be of course differences in the spread function depending on the settings of and the conditions in the ion source, but the *Ar-He* difference is more likely due to the additional excited ionic state $^2P_{1/2}$ of Ar^+ just 0.18 eV above the threshold. For this reason, the helium value ($\sigma_{He} = 0.28$ eV) is taken as basis for the experimental error and all results in the following experimental part will be given as:

$$IP(AP) \pm 2\sigma \approx IP(AP) \pm 0.6 \text{ eV} \quad (3.75)$$

The 2σ criterion seems reasonable as confidence interval as 95 % of the electrons have an energy within the range $V \pm 2\sigma$. For comparison with literature it is convenient to express the energy spread in terms of the **F**ull **W**idth at **H**alf **M**aximum (**FWHM**) value of the energy distribution which is related to σ by:

$$\mathbf{FWHM} = \sigma \cdot \sqrt{8 \cdot \ln(2)} \approx 0.7 \text{ eV} \quad (3.76)$$

Established ion sources for ionization- and appearance potential measurements employ nearly monochromatic electrons with a **FWHM** in the range of 0.05 eV [107, 41].

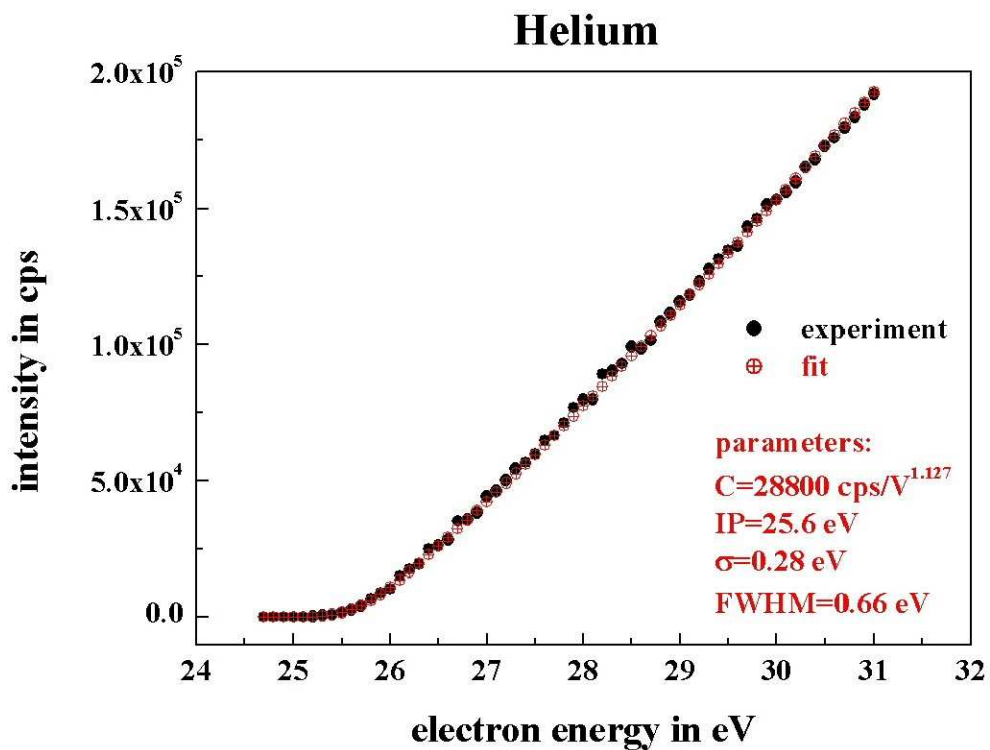


Figure 3.17: Determination of the spread function parameters by fitting Equation (3.74) to the **IE**-curve of helium

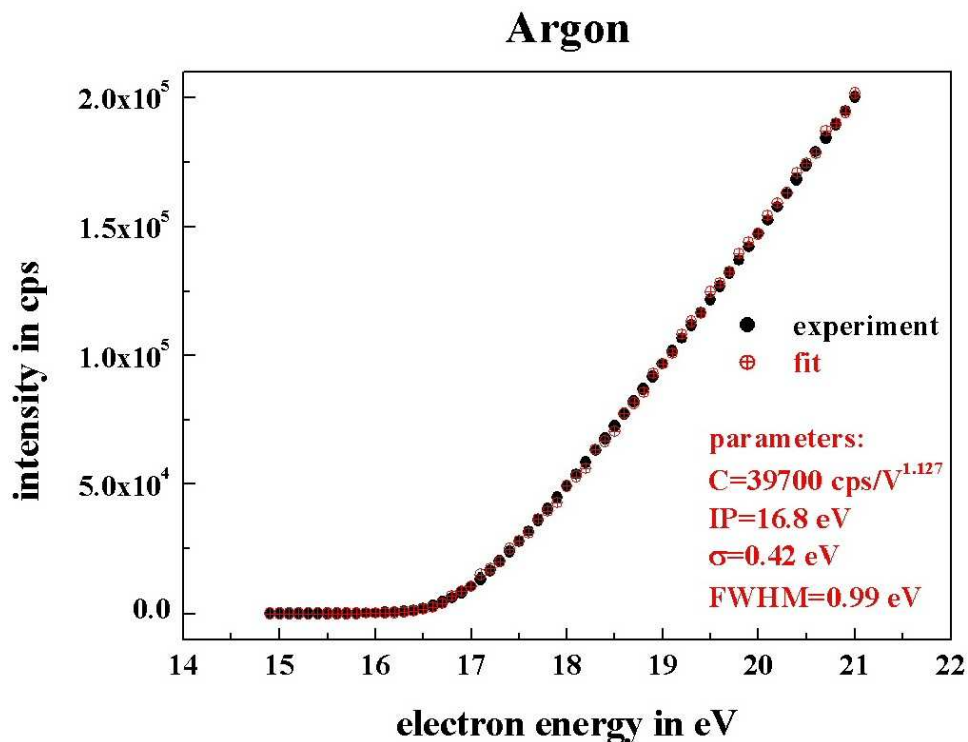


Figure 3.18: Determination of the spread function parameters by fitting Equation (3.74) to the **IE**-curve of argon

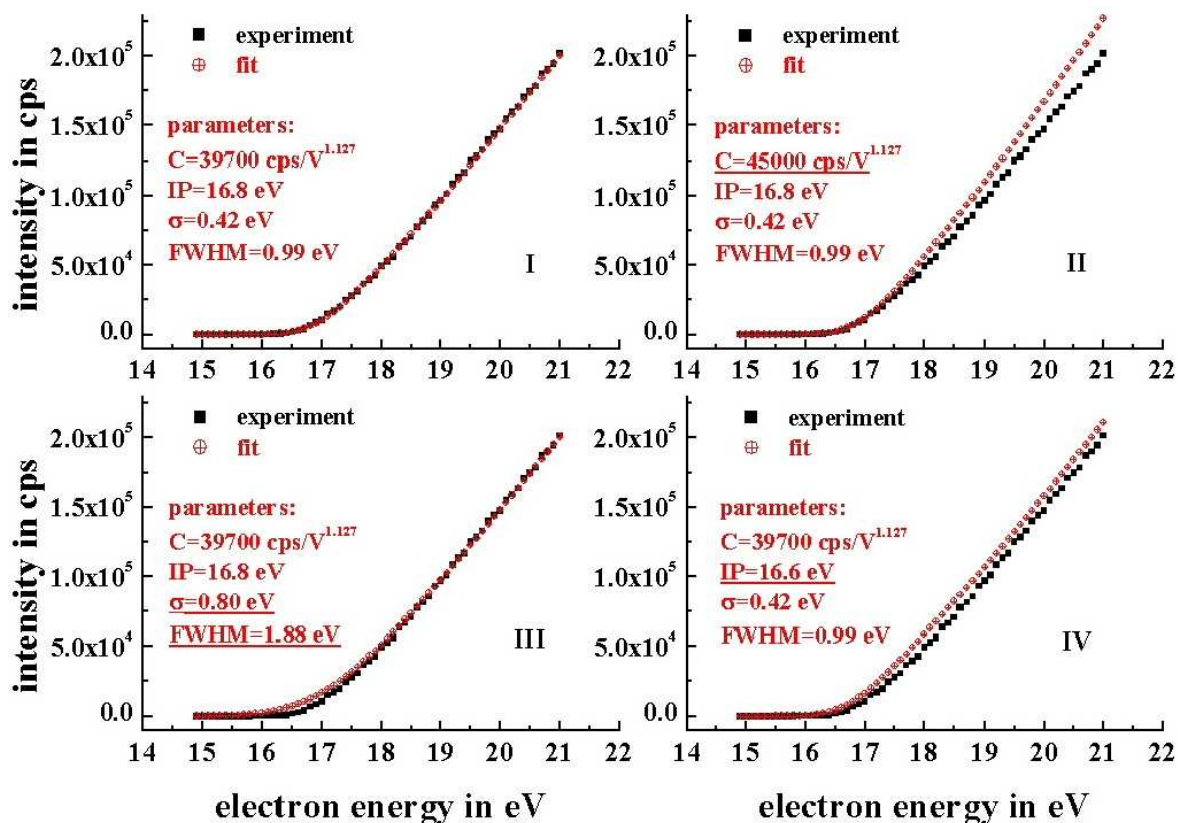


Figure 3.19: Correlation of the fit parameters C , IP and σ in Equation (3.74), original values shown in *I*, changed values underlined: $I \rightarrow II$ increase of C , $I \rightarrow III$ increase of σ , $I \rightarrow IV$ decrease of IP

The determined value of the source used in this work is about fourteen times higher. This is in the nature of the problem to be solved namely the detection of traces of small reactive intermediates like $OH\cdot$, $CH_3\cdot$ or $NH_2\cdot$. Monochromizing electrons goes along with a substantial loss of sensitivity as a result of band pass filtering. This, further complicated by the small total ionization cross section in the threshold region would it make practically impossible to detect traces of the mentioned molecules. As the ionization potentials of such small species are sufficiently separated (about 3 – 5 eV) from their corresponding appearance potentials, one can accept the higher energy spread exploiting rather the increased sensitivity.

Motivated by the literature [139], much effort was made to remove the energy spread from experimental **IE**-curves mathematically. This procedure, commonly known as ‘deconvolution’, has been thoroughly investigated and successfully applied to numerous problems in spectroscopy [140]. Notwithstanding all endeavors, the

approach failed for our data as the Fourier frequencies necessary to restore sharp onsets in the **IE**-curve are not sufficiently different from those of noise. Accordingly, the noise was highly amplified during the deconvolution process making the result useless. In conclusion, species at the same nominal mass need to be separated in their threshold potentials by about 0.6 eV for an unambiguous discrimination.

Part II

Experimental

Chapter 4

Setup

4.1 Conception

The idea of the experimental setup was to simulate the industrial **BMA** reaction as closely as possible and to disturb it as little as possible by the sampling process. To accomplish this, the high temperature tubular flow reactor was connected in line of sight to the quadrupole mass spectrometer via a molecular beam sampling interface. Figure 4.1 shows the experimental setup schematically:

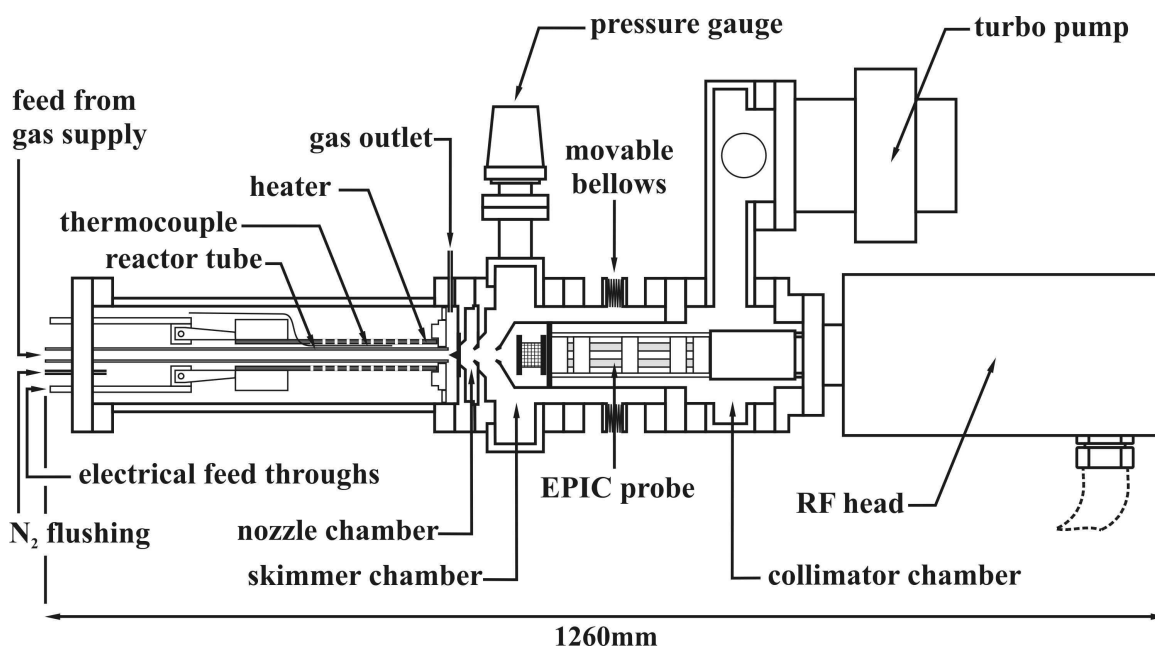


Figure 4.1: Schematic diagram of the experimental setup

A picture of the experiment is shown in Figure 4.2:

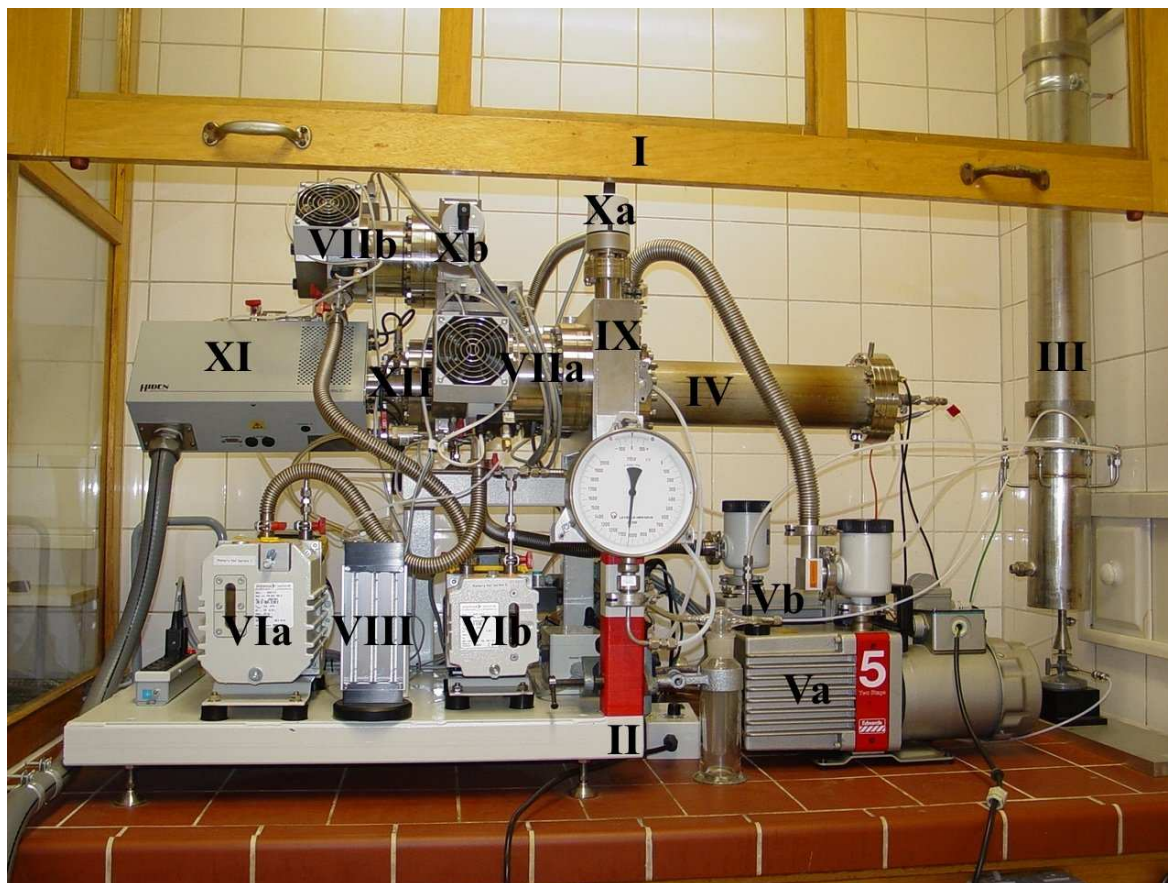


Figure 4.2: Picture of the experimental setup: I) hood, II) rack, III) exhaust gas combustion, IV) reactor, Va and Vb) rotary vane pumps for the nozzle chamber, VIa and VIb) rotary vane pumps for the skimmer and collimator chamber, VIIa and VIIb) turbomolecular pumps for the skimmer and collimator chamber, VIII) purging and flooding for the turbomolecular pumps, IX) skimmer chamber, Xa and Xb) pressure gauges for the skimmer and collimator chamber, XI) RF-head, XII) mass spectrometer

All other investigated reactions have been conducted using the same setup, independent how they are conducted commercially. The line of sight arrangement seemed promising, as a similar apparatus was successfully used by Eltenton in his pioneering work on mass spectroscopic detection of $CH_3\cdot$ radicals formed by thermal decomposition of $Pb(CH_3)_4$ [141]. The BMA experiments necessitated to place the entire experiment under the hood because of the extreme toxicity of hydrocyanic acid. Exhaust gases from reactor outlet and pumps were collected and burnt in the flame of a Bunsen burner. The presence of the flame was checked by a thermocouple so that

flame extinction caused a shutdown of the gas- and power supply of the reactor. Six mass flow controllers (Bronkhorst High-Tech) were used to dose the gases for the different reactions. All flow values given in the experimental part of this work refer to standard conditions namely $0\text{ }^{\circ}\text{C}$ and 1013 mbar . The dosing range of each **MFC** was $50 - 2000\text{ ml}\cdot\text{min}^{-1}$. The high gas throughput was necessary to comply with industrial conditions were flows of $2\text{ mol}\cdot\text{h}^{-1} \approx 750\text{ ml}\cdot\text{min}^{-1}$ and more are admitted to each tube in the bundle of a **BMA** reactor. A particle filter and a check valve were fitted before and behind each **MFC** respectively. The reactants and an internal standard were mixed immediately behind the flow controllers and fed in the reactor. Table 4.1 lists the gases which were used for the experiments:

Table 4.1: *Gases used for the experiments*

gas	purity	usage	manufacturer
CH_4	3.5	reactant	Linde
NH_3	3.8	reactant	Linde
O_2	5.0	reactant	Linde
N_2	5.0	purging	Linde
Ar	5.0	standard	Linde
He	5.0	standard	Linde
$5\%Xe/He$	5.0	calibration	Linde

4.2 Reactor

The high temperature tubular flow reactor was composed of a 500 mm long gas-tight reaction tube (*i.d.* = 6 mm , Al_2O_3 ceramics, Degussit- $Al23^{\text{®}}$, Friatec) heated by a helical silicon carbide heater (Crusilite $^{\text{®}}$, Kanthal). The inner wall of the tube was covered with a thin layer (a few μm) of platinum as catalyst. The heat current was provided by a **DC** power supply (type 6268B, Hewlett Packard) controlled by a programmable temperature controller (type 2416, Eurotherm). Temperature-time programs comprising up to eight different steps could be defined via software (iTools $^{\text{®}}$ v. 3.00, Eurotherm). The temperature was measured using a type S ($Pt - 10\% Rh/Pt$) thermocouple (Thermocoax), located at the position of the

temperature maximum between reaction tube and heater. Figure 4.3 shows the concentric arrangement of reaction tube and heater. A drawing of the reactor is given in Figure 4.4:

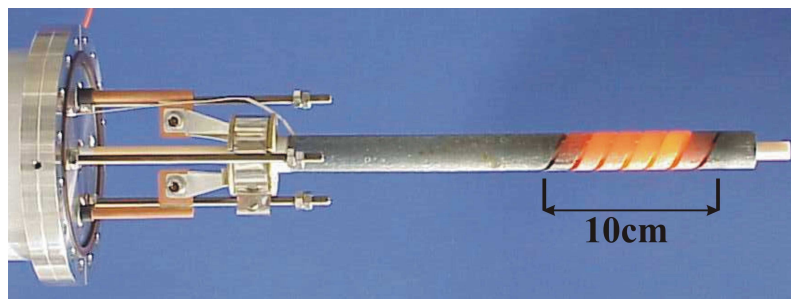


Figure 4.3: Arrangement of reaction tube and heater in the high temperature reactor

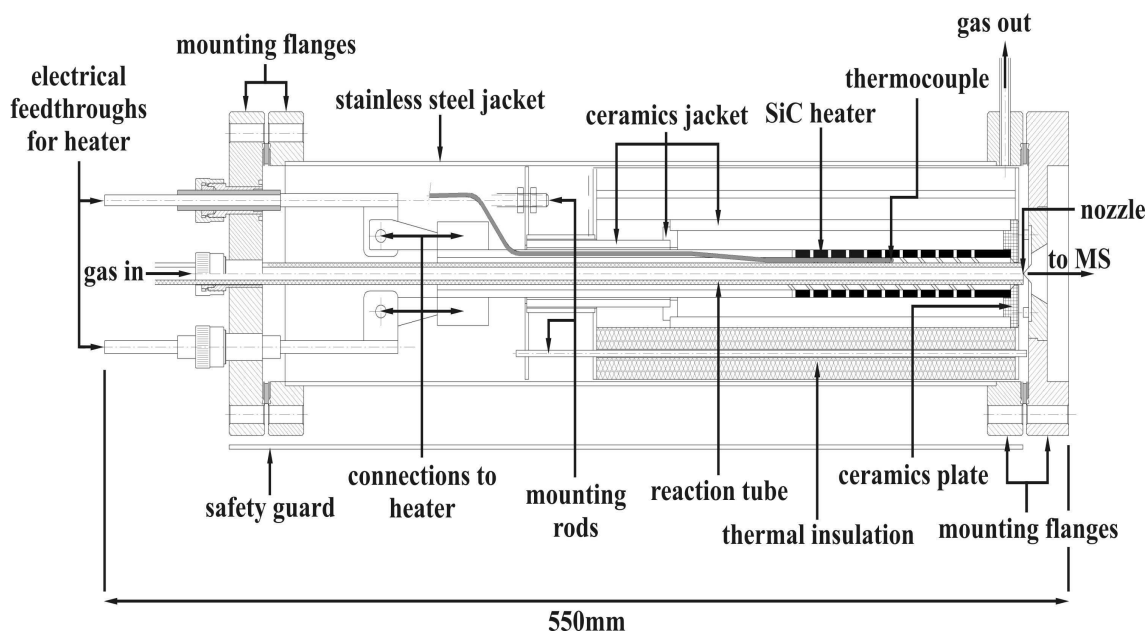


Figure 4.4: Drawing of the high temperature reactor

Temperature Profile Measurements

As will be shown in Chapter 5, different reactions with widely varying conditions have been investigated using the same setup. Accordingly, the temperature profile of the reactor varied depending on external heating power, heat of reaction, degree of conversion, gas composition and total flow. An external cooling was not provided.

Even though, the reactor was not designed to measure the temperature profile in-situ, an ex-situ measurement was performed to obtain at least a rough picture of the temperature distribution. The reactor was removed from the mass spectrometer and a spirally bent thermocouple was moved along the centerline tube axis (q.v. Fig. 4.5):

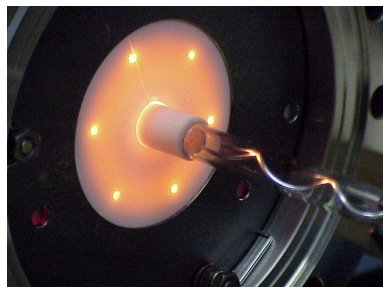


Figure 4.5: *Arrangement for the temperature profile measurements*

The bending provided a guidance of the thermocouple tip which was in one measurement series aligned with the centerline axis of the tube and in another series in close contact with the tube wall. As the temperature control was not yet available at the time, different heating powers were adjusted and the profiles were measured both with and without flows of different gases. Figure 4.6 shows the results for the maximum allowable heating power of 600 W and an argon flow of $0\text{ ml} \cdot \text{min}^{-1}$, $600\text{ ml} \cdot \text{min}^{-1}$ and $1200\text{ ml} \cdot \text{min}^{-1}$ respectively:

The plot reveals a pronounced axial temperature profile of the reactor. Behind the tube entrance, the temperature rises continuously to a maximum which is located about 95 mm in front of the nozzle of the molecular beam interface. Flushing gas through the reaction tube flattens the maximum and shifts it somewhat towards the nozzle. Moderate flows of an inert gas up to about $600\text{ ml} \cdot \text{min}^{-1}$ do not lead to a noteworthy radial temperature gradient ($|\Delta T| \leq 25\text{ }^\circ\text{C}$). At higher flows, the general effect is that in the region where the temperature rises towards the maximum, the temperature on the tube wall is higher than in the center and behind the maximum the situation is vice versa. This is due to the fact that the gas takes up heat until it reaches the same temperature as the surface. Downstream of this point, the radial gradient has the opposite sign and the heat flow is from the gas to the tube wall. In experiments with reacting gases, both the axial and the radial temperature gradient will be additionally influenced by the heat of reaction. Another important information from Figure 4.6 is that the temperature at the place of sampling, i. e. directly in front of the nozzle, depends highly on the flow conditions. Just for an inert gas flow,

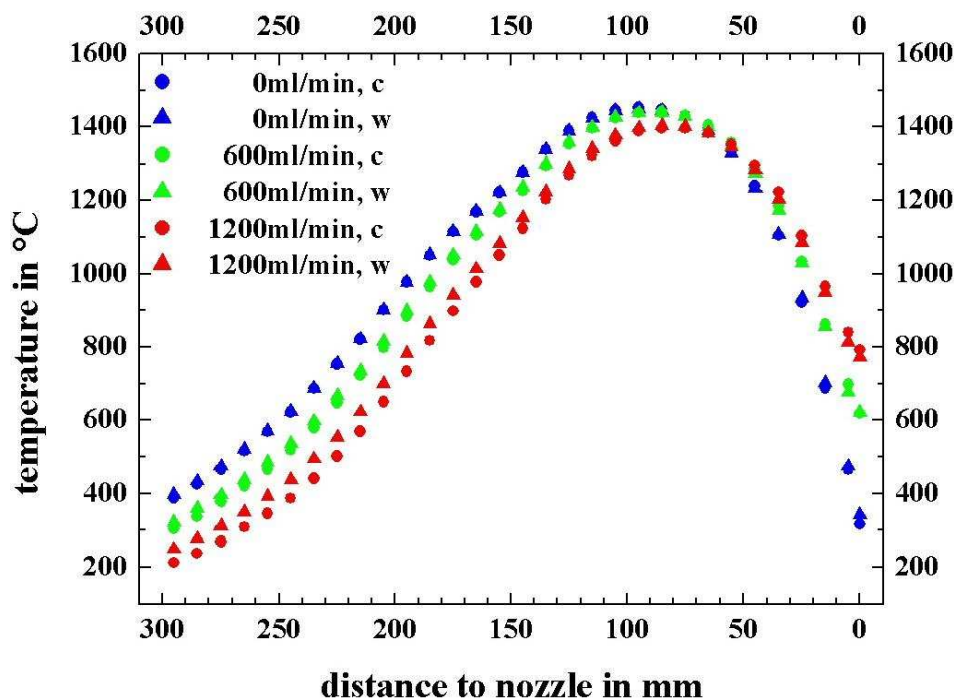


Figure 4.6: *Temperature profile of the reactor at 600 W heating power with and without argon flow: c → centerline axis, w → wall*

the temperatures there can easily reach some hundred °C. Even higher temperatures may result for strongly exothermic reactions. This was the reason to cool the nozzle as described in the following section about the interface.

4.3 Interface

The role of the interface is to reduce the pressure from reaction conditions (~ 1000 mbar) to a value where the mass spectrometer can be operated ($\sim 10^{-6}$ mbar), and to form a molecular beam which is aligned with the ion source and the quadrupole axis. To reach this pressure reduction of about nine orders of magnitude, a differentially pumped arrangement of nozzle, skimmer and collimator has been used (cp. Figure 3.1). Figure 4.7 shows a drawing of the interface. The conical nozzle ($d_n = 125$ μm) is located directly at the reaction tube outlet. It is mounted on a water cooled flange as it is exposed to a high thermal load. Nevertheless, an efficient cooling of the thin-walled nozzle tip can not be taken for granted. As a reaction of unconverted gases on the nozzle surface could lead to erroneous results, it is made up of platinum to have it from the same material as the catalyst. The nozzle plate is made

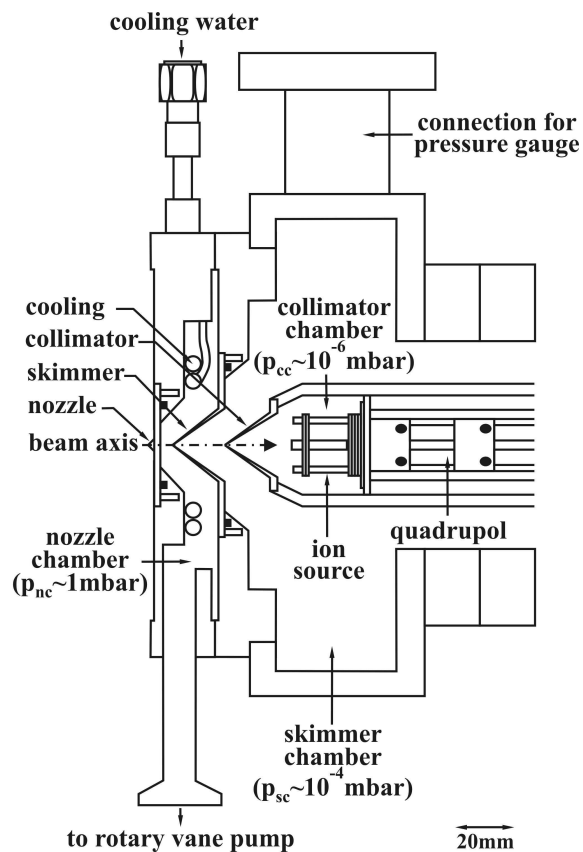


Figure 4.7: *Molecular beam sampling interface connecting reactor and mass spectrometer*

up of nickel. The pressure behind the nozzle (nozzle chamber, subscript nc) is reduced by two strong rotary vane pumps (type D12A, Leybold Hereaus and type E2M5, Edwards) to about 1 *mbar*. The sudden pressure drop from atmospheric pressure to 1 *mbar* causes the supersonic expansion (q.v. Section 3.1). It is the task of the subsequent skimmer ($d = 500 \mu m$) and collimator ($d = 900 \mu m$) arrangement to cut out the center part of the evolving beam. Similar to the nozzle, both cones are made up of nickel with a platinum tip. The volume downstream of the skimmer (skimmer chamber, subscript sc) is evacuated applying a turbo pump (type TMU261, Pfeiffer) backed by a rotary vane pump (type Duo 5C, Pfeiffer). Likewise, a combination of turbo- and rotary vane pump (types TMU261 and Duo2.5C, Pfeiffer) reduces the pressure behind the collimator (collimator chamber, subscript cc). To avoid overloading of the **CEM** detector, movable bellows permit distance variation between skimmer and collimator. As the molecular beam is divergent, an increase of this distance leads to a decrease of the signal intensity (cp. Figure 4.1). The pressure in the nozzle chamber was measured using a Pirany pressure gauge (type TPR250, Pfeiffer). The pressures in the skimmer- and collimator chamber were measured by Penning cold cathode gauges (type IKR261, Pfeiffer). Depending on reactor temperature and gas compo-

sition, heavy pressure fluctuations have been measured ($10^{-1} \text{ mbar} < p_{nc} < 10 \text{ mbar}$, $10^{-5} \text{ mbar} < p_{sc} < 10^{-4} \text{ mbar}$, $10^{-7} \text{ mbar} < p_{cc} < 10^{-6} \text{ mbar}$). Partly they can be considered real because the nozzle gas throughput is a function of the reactor temperature and gas specific properties but on the other hand they are only apparent as the used pressure gauges rely on a gas type dependent measurement principles. For this reason, absolute pressure values are not given in the discussion of the experiments as they could not be gas type corrected. Interface and vacuum assembly were delivered as one complete unit (type HPR60) from Hiden Analytical Limited.

4.4 Mass Spectrometer

The mass spectrometer located in the collimator chamber is a triple mass filter quadrupole instrument (type HAL4 EPIC Low Energy) manufactured by Hiden Analytical Limited. It allows for the analysis of neutrals, radicals, as well as positive and negative ions with a mass scan range from $0.4 - 510 \text{ amu}$ [142]. As discussed in Section 3.2.2, the ion source is of cross beam type, designed to work with a molecular beam sample inlet. The single channel electron multiplier is mounted off-axis to achieve maximum sensitivity. All electrode settings are controlled via computer using Hiden's MASsoft PC software [143]. Beside common mass scans and the possibility to monitor selected masses over time, the software permits scanning and mapping of all electrodes (cp. Figure 3.7). There are numerous publications in the literature where the Hiden spectrometer was applied successfully to detect radicals using the threshold ionization technique [144, 145, 146].

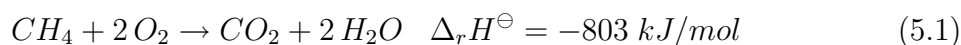
Chapter 5

Experiments

5.1 Catalytic Combustion of Methane

5.1.1 Temperature Programmed Measurements

The first reaction studied was the catalytic combustion of methane:



As it is a highly exothermic reaction, the first experiment was a temperature programmed measurement to get an impression how a CH_4/O_2 mixture behaves in this reactor. A total flow of $300 \text{ ml} \cdot \text{min}^{-1}$ of a fuel rich mixture containing 50 % CH_4 , 13 % O_2 and 37 % He was subjected to a temperature time program. Methane was used in excess to be on the safe side with respect to the explosion limit (5 – 15 % CH_4 in air [69, page 16-17]). For comparison with the literature on combustion it is necessary to express the composition of the mixture by the so called equivalence ratio ϕ , defined as the ratio between the actual fuel/oxidant ratio and the fuel/oxidant ratio at stoichiometric composition:

$$\phi = \frac{\left(\frac{p(\text{fuel})}{p(\text{oxidant})} \right)_{\text{actual}}}{\left(\frac{p(\text{fuel})}{p(\text{oxidant})} \right)_{\text{stoichiometric}}} \quad (5.2)$$

Fuel lean mixtures have a ϕ value between 0 and 1, whereas for fuel rich mixtures ϕ is between 1 and ∞ . Accordingly, the mixture used here corresponds to $\phi = 7.7$.

After narrowing the interesting temperature range down by preliminary tests, the mixture was fed to the reactor which was heated after equilibration from $350\text{ }^{\circ}\text{C}$ to $550\text{ }^{\circ}\text{C}$ with a rate of $0.5\text{ }^{\circ}\text{C}\cdot\text{min}^{-1}$ and afterwards cooled down again to $350\text{ }^{\circ}\text{C}$ with a rate of $-0.5\text{ }^{\circ}\text{C}\cdot\text{min}^{-1}$. To follow the reaction, mass spectra ($0.4 - 50.0\text{ }amu$) were recorded so that each spectrum corresponds to a temperature change of $\Delta T = \pm 1\text{ }^{\circ}\text{C}$.

For a discussion of the results it is necessary to compare the evolution of the reaction products with the temperature curve that was measured by the thermocouple. Figure 5.1 is an enlarged section of Figure 4.4 and shows more precisely the position of the thermocouple. The thermocouple is located at the temperature maximum

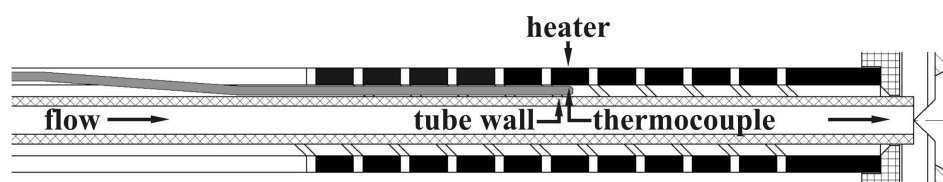


Figure 5.1: *Location of the thermocouple in the reactor*

between the heater and the outer tube wall. Due to the very slow heating rate and the good insulation, all parts inside the concentric heater can be considered to be in thermal equilibrium, as long as there is no chemical reaction proceeding inside the tube. Before the reaction starts, the temperature measured by the thermocouple is thus a good value for the catalyst temperature. Figure 5.2 shows the evolution of the reaction product CO_2 . The data points were obtained by integration of the peak at $44\text{ }amu$ and subsequent division by the peak area of the internal standard (He at $4\text{ }amu$). Figure 5.3 shows the corresponding temperature curve.

At the beginning of the experiment, the temperature rises linearly with the given rate of $0.5\text{ }^{\circ}\text{C}\cdot\text{min}^{-1}$ starting from $350\text{ }^{\circ}\text{C}$. At $358\text{ }^{\circ}\text{C}$ the thermocouple registers a sharp jump in temperature to about $367\text{ }^{\circ}\text{C}$. This jump corresponds to the ignition of the combustion reaction as shown in the enlarged section of Figure 5.2. From this temperature on, CO_2 is produced in small but exponentially increasing amounts. The thermocouple registers this ignition point because the reaction starts at the position in the tube where the temperature is highest and this is the position of the thermocouple tip. The temperature control is too slow to compensate for the sudden ‘chemical heating’ which results in the measured temperature jump. After a slight deviation from linearity the controller reduces the heating power accordingly

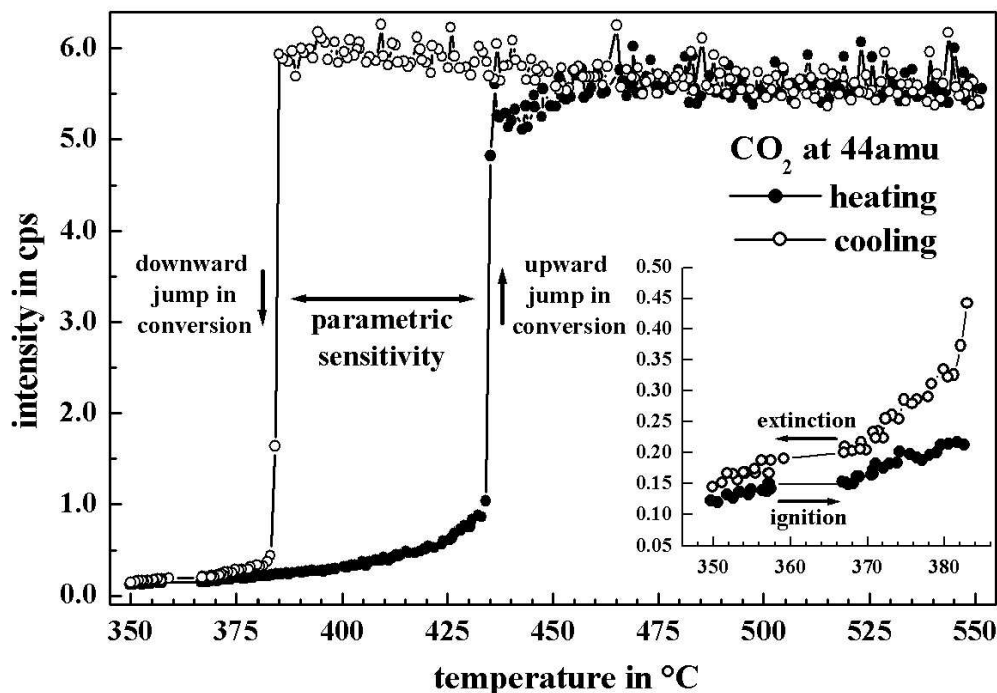


Figure 5.2: Catalytic combustion of methane: CO_2 evolution during the temperature programmed experiment (*He* corrected signal intensities), solid circles - heating up, open circles - cooling down

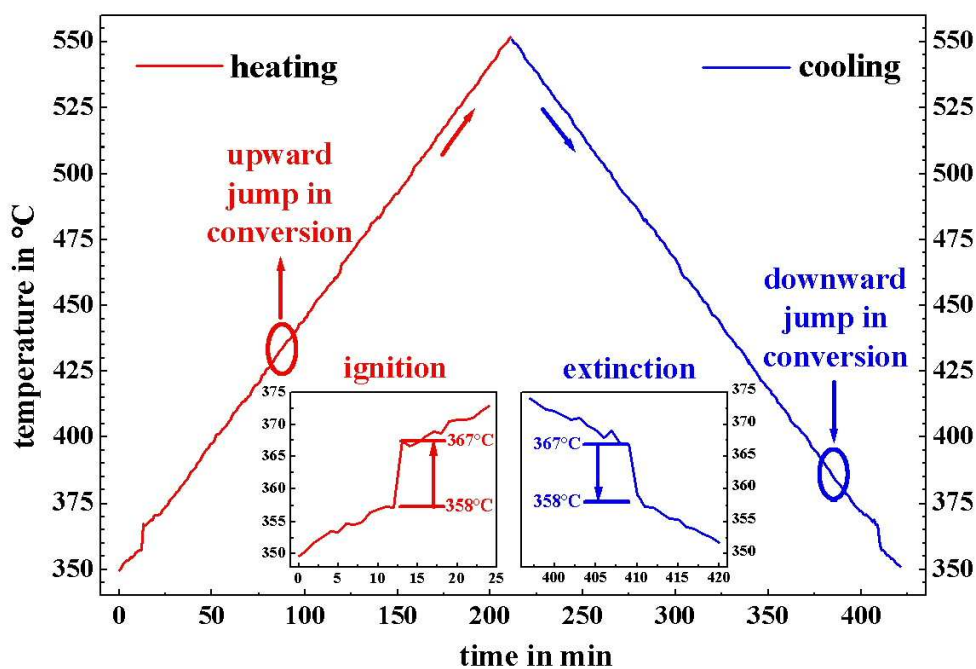


Figure 5.3: Catalytic combustion of methane: temperature curve measured by the thermocouple during the temperature programmed experiment

and proceeds with the temperature program. The same jump at the same position occurs with opposite sign in the cooling part of the program. At this point, frequently denoted as ‘extinction point’, the surface temperature becomes too low to maintain the reaction anymore.

The ignition behavior of CH_4/O_2 mixtures over Pt has been investigated both theoretically [147] and experimentally [148, 149, 150]. The publications cited here discuss the ignition temperature in terms of a modified equivalence ratio which is closely related to ϕ by:

$$\phi_{mod} = \frac{\phi}{\phi + 1} \quad (5.3)$$

This modified equivalence ratio has the advantage that it describes fuel lean and fuel rich mixtures on a comparable scale, namely $0 < \phi_{mod} < 0.5$ for fuel lean and $0.5 < \phi_{mod} < 1$ for fuel rich mixtures. All works found that heterogeneous ignition occurs at a surface temperature between about $600\text{ }^\circ C$ for fuel lean ($\phi_{mod} \approx 0.2$) and $350\text{ }^\circ C$ for fuel rich mixtures ($\phi_{mod} \approx 0.9$) and that the ignition temperature decreases with increasing ϕ_{mod} . A heterogeneous ignition beyond these limits is not possible. The mixture used here had a ϕ_{mod} value of 0.88 and the measured ignition temperature of $358\text{ }^\circ C$ is in good agreement with the literature.

After ignition, the CO_2 signal shows a slow but exponential increase which culminates at about $434\text{ }^\circ C$ in an upward jump in conversion (q.v. Figure 5.2) accompanied by total conversion of the under-stoichiometric oxygen. Figure 5.4 shows mass spectra immediately before and after the conversion jump. The transition to total oxygen conversion takes place within a very small temperature interval from $434 - 436\text{ }^\circ C$. This sudden conversion jump results from the parametric sensitivity of the tubular flow reactor. Parametric sensitivity means, that a small change in an operating variable like here the reactor temperature induces a large change in the conversion. This happens because a small increase in temperature leads to a large change in the reaction rate due to the exponential dependence of the reaction rate from temperature. The increased reaction rate results in turn in more heat generation which further increases the reaction temperature. This feedback mechanism results in a reactor runaway when the rate of heat generation exceeds by far the rate of heat removal.

As pointed out in Figure 5.3, the thermocouple does not register any temperature change neither when the conversion jumps up nor when it jumps down, even though

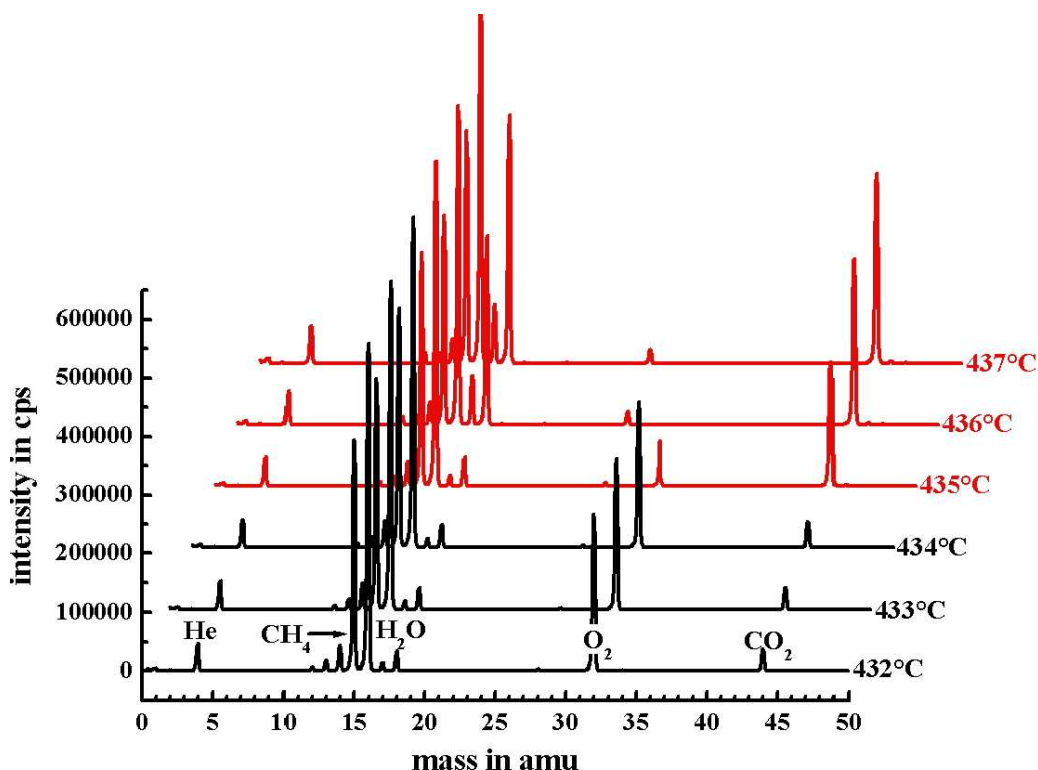


Figure 5.4: *Catalytic combustion of methane: temperature programmed experiment, mass spectra in the parametric sensitive region around 434 °C*

a much higher jump than at the ignition and extinction point is to be expected. The only explanation for this result is, that the conversion jumps do not occur at the position where the reaction was originally ignited but rather in a tube section located upstream the thermocouple tip. This can be understood as follows. After ignition, the reaction zone spreads out up- and downstream of the original onset position. The conversion along the tube axis causes a concentration gradient of the reactants. As a result, the partial pressures of CH_4 and O_2 are higher upstream the ignition point than downstream the ignition point. This leads in turn to a gradient of the reaction rate and shifts the reaction zone more and more towards the reactor inlet, away from the ignition point. If the conversion jump occurs now far enough from the thermocouple position, no change in temperature will be registered anymore. This shift of the reaction zone could have serious consequences for the chance to sample reactive intermediates as their residence time in the remaining tube section becomes longer increasing the probability to lose them before sampling.

The temperature programmed experiment supplies another important result which has to be discussed before going on with the presentation of the mass spectral and the

appearance potential data. For this purpose, Figure 5.5 shows the course of the peak area of the internal standard *He* at $m/z = 4$ *amu* during the temperature program. Additionally, the uncorrected peak area vs. temperature plots for the educts CH_4 , O_2 and the products H_2O and CO_2 are shown in Figure 5.6. According to Equation 5.1, the reaction preserves volume neutrality and as a consequence, the concentration of the internal standard *He* should not be changed during the course of the reaction. Contrary to the expectation, Figure 5.5 shows a sharp increase of the signal intensity of *He* caused by the upward jump in conversion at 434 °C. After this point the signal intensity drops continuously until the downward jump in conversion at 384 °C where the *He* signal shows an intensity jump down as well. The same signal trend is overlaid to the curves of CH_4 , H_2O and CO_2 . Figure 5.7 shows how these changes can be corrected for by standardization with the helium signal. One sees that the correction works well for CO_2 and O_2 , both having signal intensities not much different from the standard. The correction is imperfect for H_2O and an overcorrection is observed for CH_4 . Both components have intensities much higher than the standard and already small differences lead to significant errors. Signal changes that are not related to composition changes limit the value of the data for a quantitative interpretation and it is important to understand their reasons.

Dependence of Signal Intensities from Sampling and Detection Conditions

Signal changes without concentration changes can be due to both, the sampling- and the detection process. From the viewpoint of sampling, the signal intensity measured by the mass spectrometer is proportional to the particle density in the ion source which is by approximation given by the beam density at this point (q.v. Figure 3.1, ion source = target). The beam density in turn is proportional to the mass flow through the nozzle orifice q_m in $g \cdot s^{-1}$:

$$q_m = A \cdot \rho \cdot v \quad (5.4)$$

A is the area of the orifice, ρ the density and v the flow speed. Exploiting Equation (3.9) leads to:

$$q_m = -A \cdot \left(\frac{dp}{dv} \right) \quad (5.5)$$

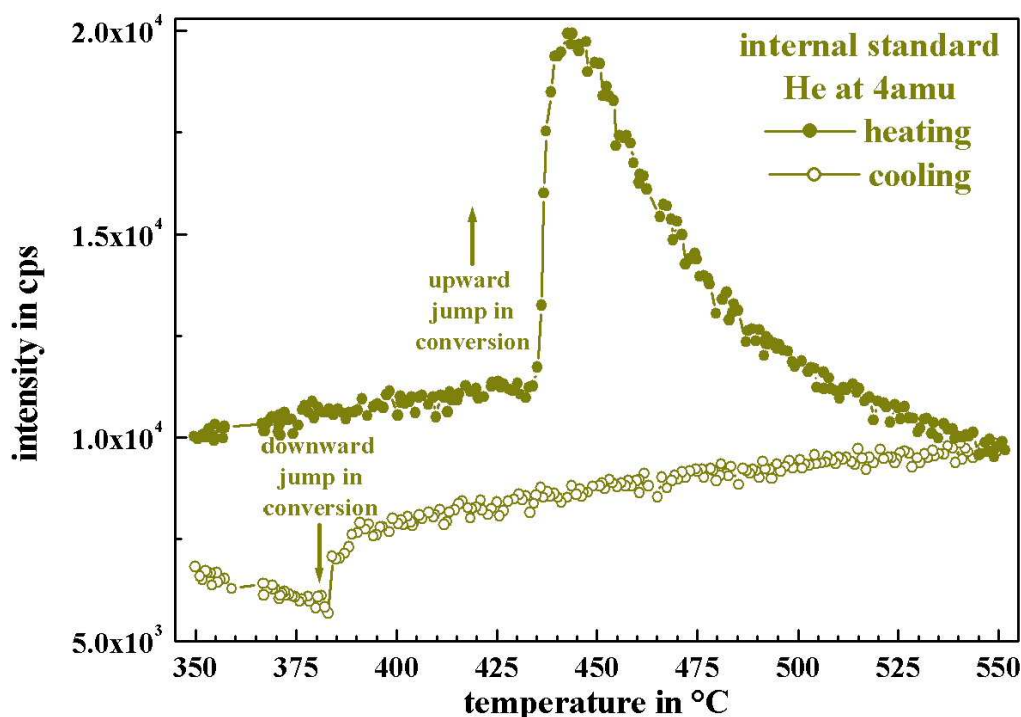


Figure 5.5: Catalytic combustion of methane: temperature programmed experiment, peak area vs. temperature curve for the internal standard He at $m/z = 4$ amu

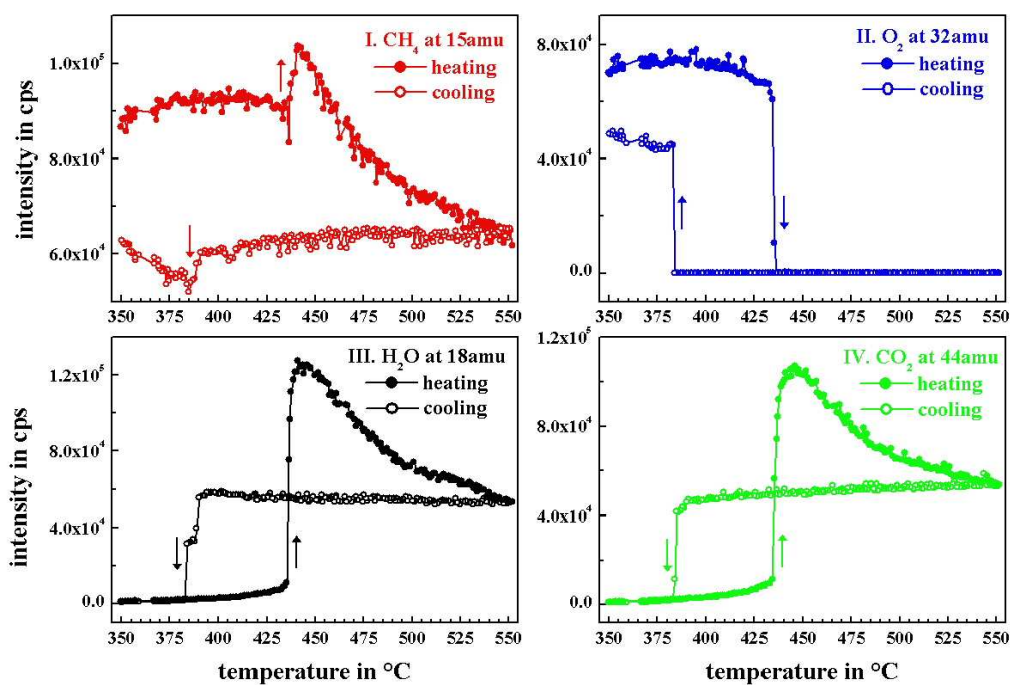


Figure 5.6: Catalytic combustion of methane: temperature programmed experiment, peak area vs. temperature curves for I.) CH_4 , II.) O_2 , III.) H_2O and IV.) CO_2 (uncorrected signal intensities)

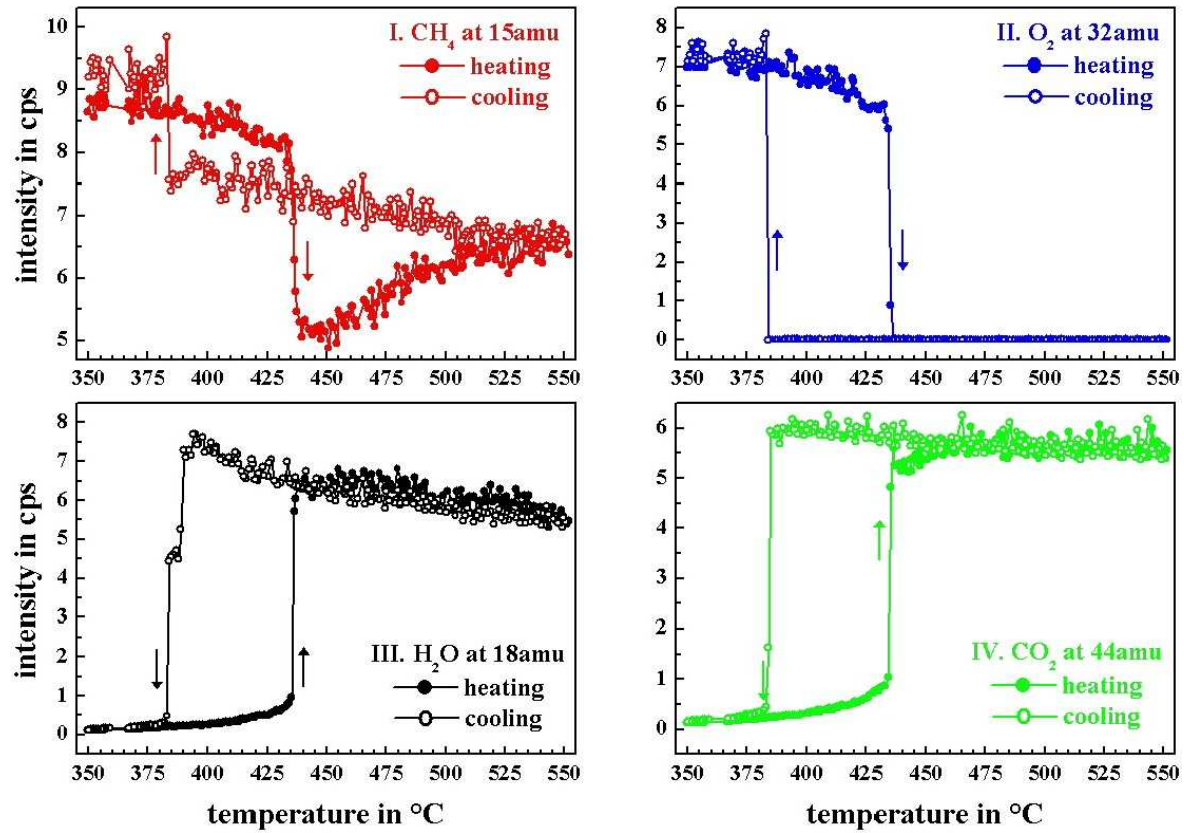


Figure 5.7: Catalytic combustion of methane: temperature programmed experiment, peak area vs. temperature curves for I.) CH₄, II.) O₂, III.) H₂O and IV.) CO₂ (He corrected signal intensities)

Calculating the differential dp/dv from Equation (3.13) and inserting in (5.5) gives:

$$q_m = A \cdot p_0 \cdot \left(\frac{2\kappa}{\kappa - 1} \frac{M}{RT_0} \left[\left(\frac{p}{p_0} \right)^{\frac{2}{\kappa}} - \left(\frac{p}{p_0} \right)^{\frac{1+\kappa}{\kappa}} \right] \right)^{\frac{1}{2}} \quad (5.6)$$

The maximum mass flow q_m^* is reached if the pressure in the nozzle chamber is below the critical pressure p_{nc}^* , which is always fulfilled in our setup. Inserting Equation (3.18) in (5.6) gives:

$$q_m^* = \frac{\pi}{4} d_n^2 \cdot p_0 \cdot \left(\frac{2}{\kappa + 1} \right)^{\frac{1}{\kappa - 1}} \left(\frac{2\kappa}{\kappa + 1} \frac{M}{RT_0} \right)^{\frac{1}{2}} \quad (5.7)$$

Equation (5.7) shows, that the maximum mass flow q_m^* and hence the signal intensities should increase linearly with the reactor pressure p_0 and decrease with the reactor temperature according to $1/\sqrt{T_0}$. Furthermore, the mass flow depends quadratically on the nozzle diameter d_n .

It is not possible to explain the sharp changes of the helium signal by any of these dependencies. Significant pressure fluctuations can be ruled out as the reactor is open to atmosphere. Changes in the gas temperature T_0 could in principle account for the signal intensity jumps but then they should have the opposite sign (q.v. Equation 5.7). A change of the nozzle diameter due to thermal expansion could account for gradual but not for instantaneous signal changes. Resulting from these considerations, the intensity jumps must be due to the abrupt changes of the chemical composition. It is primarily the ion generation and extraction process which depends sensitively on the chemical composition inside the source, even if the pressure of the component under consideration is constant.

There are essentially three effects responsible to cause signal changes by changing the chemical environment:

- **space charge effects:** high ion or electron densities distort the potential inside the source
- **interactions between gas phase and filament:** gas phase components can react with the filament and change the emission characteristic of the material
- **ion-molecule reactions** collisions between ions and neutrals can result in chemical reactions or charge transfer processes

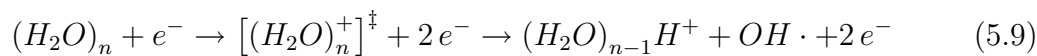
Especially space charge effects could be very pronounced in the measurements done here, because the ion source was operated at relatively high pressures ($\sim 10^{-6}$ mbar) and the ions were decelerated to low energies (≤ 2 eV) to obtain the high mass resolution required for appearance potential measurements [151]. However, it is not possible to predict how the effects listed above influence the measured signal intensities in the individual case. The only possibility to get quantitative reliable results is to keep composition changes small (dilution) and to correct the sensitivity changes using an internal standard.

The second point open to discussion is the reason for the monotonic decreasing signal following the conversion induced jump up in intensity at 434°C . Figure 5.8 shows that the helium signal changes in all measured spectra nearly parallel to the signals of H_2O and CO_2 . The physical conditions in the reactor can again not account

for such a signal trend and the chemical composition is constant over this range. A very likely explanation for this behavior was found in the mass spectra themselves. Figure 5.9 shows spectra around 37 amu immediately before and after the total consumption of oxygen. The low intensity peak at 37 amu was very surprising and could not be explained in the first instance. To check for further peaks at higher mass numbers a high sensitivity measurement was performed which is shown in Figure 5.10. The spectrum shows further peaks all equally spaced by exactly 18 amu and all at odd mass numbers. The declining peak intensities remind of a distribution function. The unexpected peak at 37 amu belongs therefore to this series too. It is known from the literature that water clusters $(H_2O)_n$ are formed under certain conditions during a supersonic expansion of moist gas mixtures [152]:



It is further described that the water clusters stabilize themselves after ionization according to the following mechanism [153]:



The mass spectrum in Figure 5.10 shows obviously the distribution of the protonated cluster ions. Water clusters are nothing else than a pre-stage to condensed water. Taking this into account, the question raises now, whether water can also condense in the nozzle orifice under these conditions. To answer this question unambiguously, the gas temperature in front of the nozzle needs to be known. This value could not be measured during the experiment but it is possible to calculate a critical value $T_{0,max}$ below which condensation occurs and to assess if this value is within the bounds of possibility.

Assuming ideal gas behavior, the composition of the mixture after total conversion of oxygen is $x_{O_2} \sim 0$, $x_{CH_4} \sim 0.435$, $x_{CO_2} \sim 0.065$, $x_{He} \sim 0.370$ and $x_{H_2O} \sim 0.130$ (x means mole fraction). With this composition, one can calculate the κ value of the mixture. Vibrational degrees of freedom can be neglected in this temperature range leading to $\kappa \sim 1.4$. The partial pressure of water at the nozzle exit can then be calculated using Equation (3.18):

$$p_{H_2O}^* = p_0 \cdot \left(\frac{2}{\kappa + 1} \right)^{\frac{\kappa}{\kappa - 1}} \cdot x_{H_2O} \sim 1013 \text{ mbar} \cdot 0.53 \cdot 0.13 = 70 \text{ mbar} \quad (5.10)$$

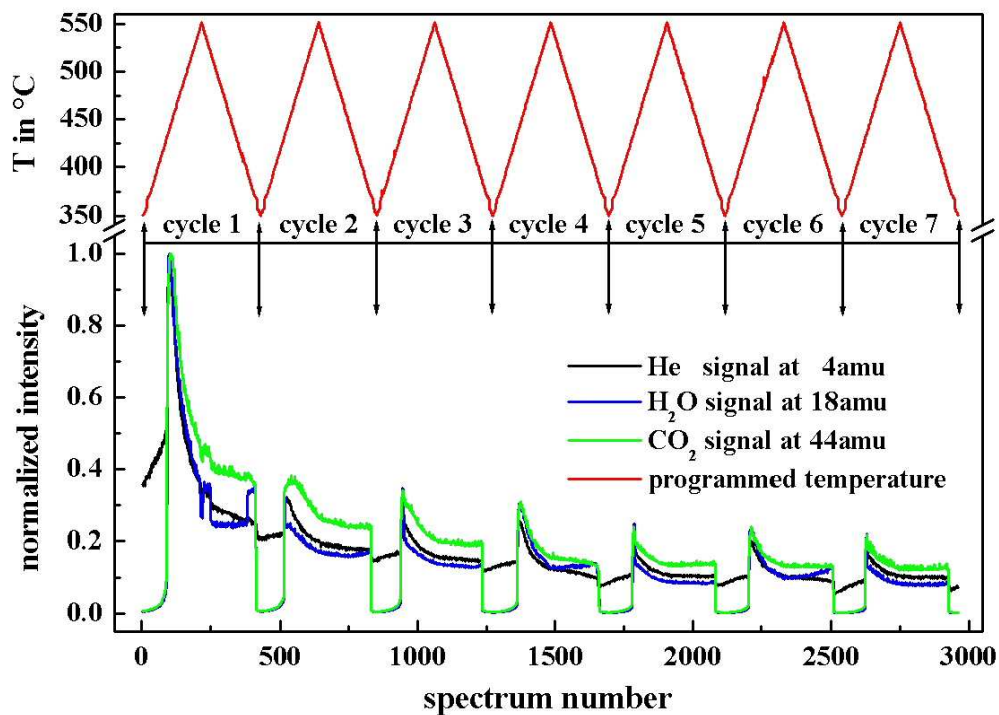


Figure 5.8: Catalytic combustion of methane: signal intensities of He, H₂O and CO₂ during the temperature programmed experiment

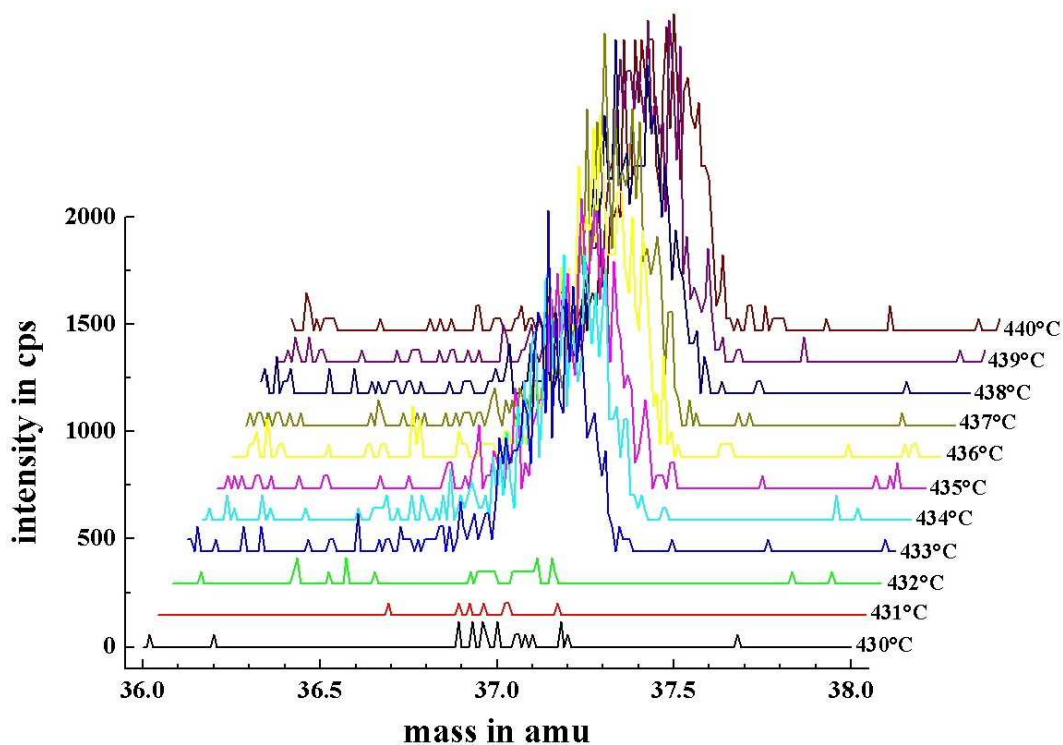


Figure 5.9: Catalytic combustion of methane: temperature programmed experiment, mass spectra around 37 amu before (430–432 °C) and after (433–440 °C) the upward jump in conversion

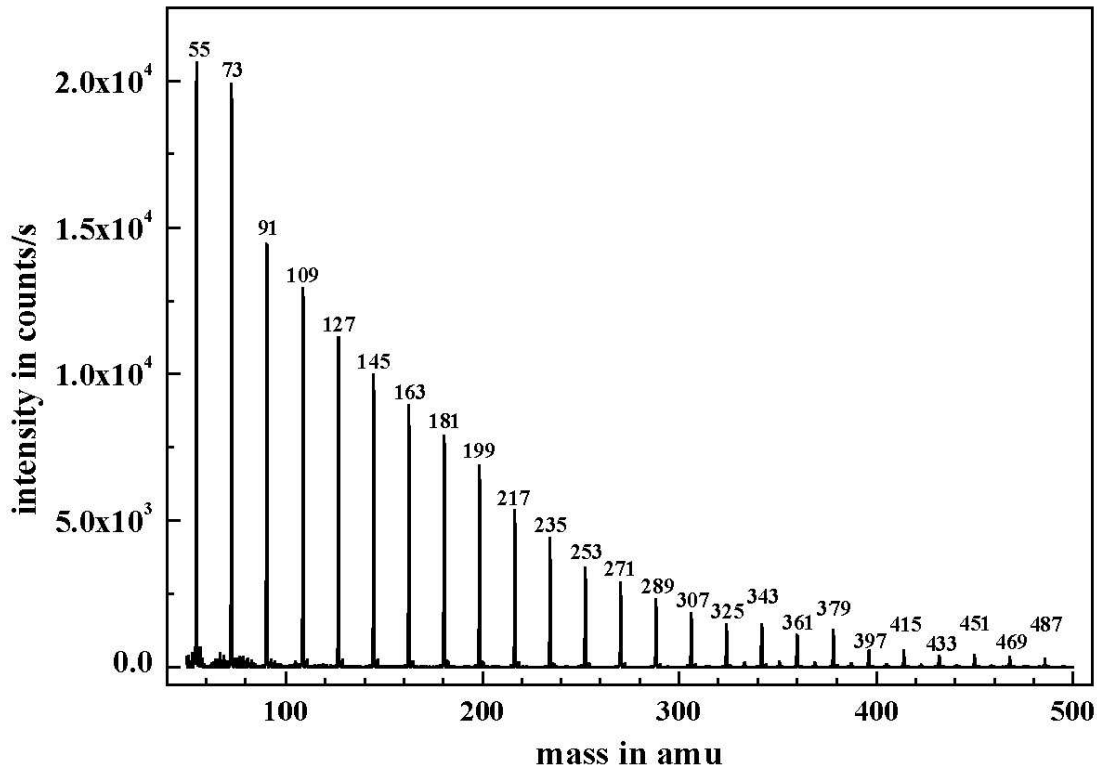


Figure 5.10: *Catalytic combustion of methane: high sensitivity mass spectrum from 50 – 500 amu immediately after the upward jump in conversion*

Condensation will occur if the vapor pressure of water at the nozzle exit is lower than 70 mbar. This is the case if the temperature there is below 39 °C, e.g. $T_{max}^* \leq 39\text{ °C} = 312\text{ K}$ [69, page 6-10]. This critical value at the nozzle exit can be related to the critical value in front of the nozzle using Poisson's law (3.16) together with (3.18):

$$\left(\frac{T_{max}^*}{T_{0,max}}\right)^{\frac{\kappa}{\kappa-1}} = \left(\frac{p^*}{p_0}\right) \rightarrow T_{0,max} = \frac{\kappa+1}{2} \cdot T_{max}^* \sim 1.2 \cdot 312\text{ K} \sim 374\text{ K} \quad (5.11)$$

This means, if the temperature in front of the nozzle T_0 is lower than $T_{0,max} = 101\text{ °C}$, the mixture will be supersaturated with water vapor and condensation inside the nozzle can occur. It is known from the temperature profile measurements (q.v. Figure 4.6) that the temperature at small gas flows decreases steeply towards the tube exit. As the temperature at level of the thermocouple tip is always $\leq 550\text{ °C}$ a value $\leq 101\text{ °C}$ at the tube exit is within the bounds of possibility.

Taking this into account, the signal course in Figure 5.8 can easily be explained. The conversion jump at 434 °C rises the water concentration to a value sufficient for supersaturation at the nozzle exit. Now, water condensation reduces the effective orifice diameter d_n and hence the signal intensity as given by Equation (5.7). At the

same time, water clusters appear in the mass spectrum. The condensation continues until the water production stops at 384 °C. Indeed, the signal intensities rise after this point as part of the water can now evaporate again.

The signal drifts were discussed so extensively here, because they point to problems that appear by sampling chemical reactions. As it is the intention of the experiment to identify species at low concentrations it is not advisable to work with highly diluted mixtures. If one uses undiluted mixtures one has to cope with significant changes in the chemical composition and with condensation as well. Composition changes can be prevented by steady state measurements. Limiting are signal drifts caused by condensation processes as it is not possible to correct them in appearance potential measurements. Consequently, these measurements have to be performed in a time span short as compared to the drift. This in turn causes a loss in signal intensity and reduces considerably the quality of the ionization efficiency curves. Heating the nozzle could avoid the condensation but then one risks to start reactions at the nozzle surface. A solution is to use an internal nozzle, that means a pinhole in the reactor wall as shown schematically in Figure 3.5, Sketch II. In this case, the nozzle is at high temperature and sampling is truly in-situ.

5.1.2 Mass Spectral Data

After discussing important fundamentals like ignition behavior and signal drifts the question on intermediates is still open. According to Section 2.3.1, the following species are possibly involved in the reaction mechanism: a) $HO_2\cdot$, b) $CH_3OO\cdot$, c) $HCHO$, d) CH_3OH , e) H_2O_2 , f) $OH\cdot$, g) $CH_3\cdot$.

For the molecules a - e it is sufficient to explore the mass spectrum as all have at least one mass which is not superimposed by peaks of the reactants and products. To identify the radicals f and g it is necessary to investigate the corresponding appearance potential measurements. Figure 5.11 shows a mass spectrum recorded at a temperature of 438 °C, that means shortly after the conversion jump up. The spectrum was taken from cycle 1 of the temperature programmed experiment and corresponds to the maximum sensitivity region (cp. Figure 5.8). Table 5.1 shows the assignment of the peaks. If several ions contribute to one signal, the significant ions are printed in boldface. Expected intermediates are highlighted using red font. As

Table 5.1: Peak assignment table to Figure 5.11, significant ions bold, expected species red

mass in amu	assignment	ion type	intensity in cps	comment
1	$^1H^+$	fragment	$22 \cdot 10^3$	-
2	$^1H_2^+$	parent	$39 \cdot 10^2$	-
4	$^4He^+$	atomic ion	$32 \cdot 10^4$	internal standard
12	$^{12}C^+$	fragment	$52 \cdot 10^3$	-
13	$^{12}C^1H^+$	fragment	$59 \cdot 10^3$	-
14	$^{12}C^1H_2^+$	fragment	$13 \cdot 10^4$	-
15	$^{12}C^1H_3^+$	fragment radical ion?	$13 \cdot 10^5$	- AP measurement follows
16	$^{12}C^1H_4^+$ $^{16}O^+$	parent fragment	$20 \cdot 10^5$	-
17	$^{16}O^1H^+$ $^{13}C^1H_4^+$	fragment radical ion? parent	$30 \cdot 10^4$	- AP measurement follows isotopic peak
18	$^1H_2^{16}O^+$	parent	$16 \cdot 10^5$	-
19	$^1H_3^{16}O^+$	ion-molecule reaction	$60 \cdot 10^2$	formed in ion source
20	$^{18}O^1H_2^+$	parent	$39 \cdot 10^2$	isotopic peak
22	$^{12}C^{16}O_2^{++}$	parent	$13 \cdot 10^3$	doubly charged
28	$^{12}C^{16}O^+$	parent/fragment	$55 \cdot 10^3$	-
29	$^{13}C^{16}O^+$ $^{12}C_2^1H_5^+$ $^{12}C^{16}O^1H^+$	parent/fragment fragment fragment	$12 \cdot 10^2$	isotopic peak impurity CH_4 not detectable
30	$^{12}C_2^1H_6^+$ $^{12}C^{16}O^1H_2^+$	parent parent	$12 \cdot 10^2$	impurity CH_4 not detectable
31	$^{12}C^{16}O^1H_3^+$	fragment	-	not detectable
32	$^{16}O_2^+$ $^{12}C^{16}O^1H_4^+$	parent parent	$27 \cdot 10^2$	- not detectable
33	$^{16}O_2^1H^+$	radical ion	-	not detectable
34	$^{16}O_2^1H_2^+$	parent	-	not detectable
37	$^{16}O_2^1H_5^+$	fragment	$11 \cdot 10^2$	water cluster
44	$^{12}C^{16}O_2^+$	parent	$12 \cdot 10^5$	-
45	$^{13}C^{16}O_2^+$	parent	$15 \cdot 10^3$	isotopic ion
46	$^{12}C^{18}O^{16}O^+$	parent	$53 \cdot 10^2$	isotopic ion
47	$^{12}C^{16}O_2^1H_3^+$	radical ion	-	not detectable

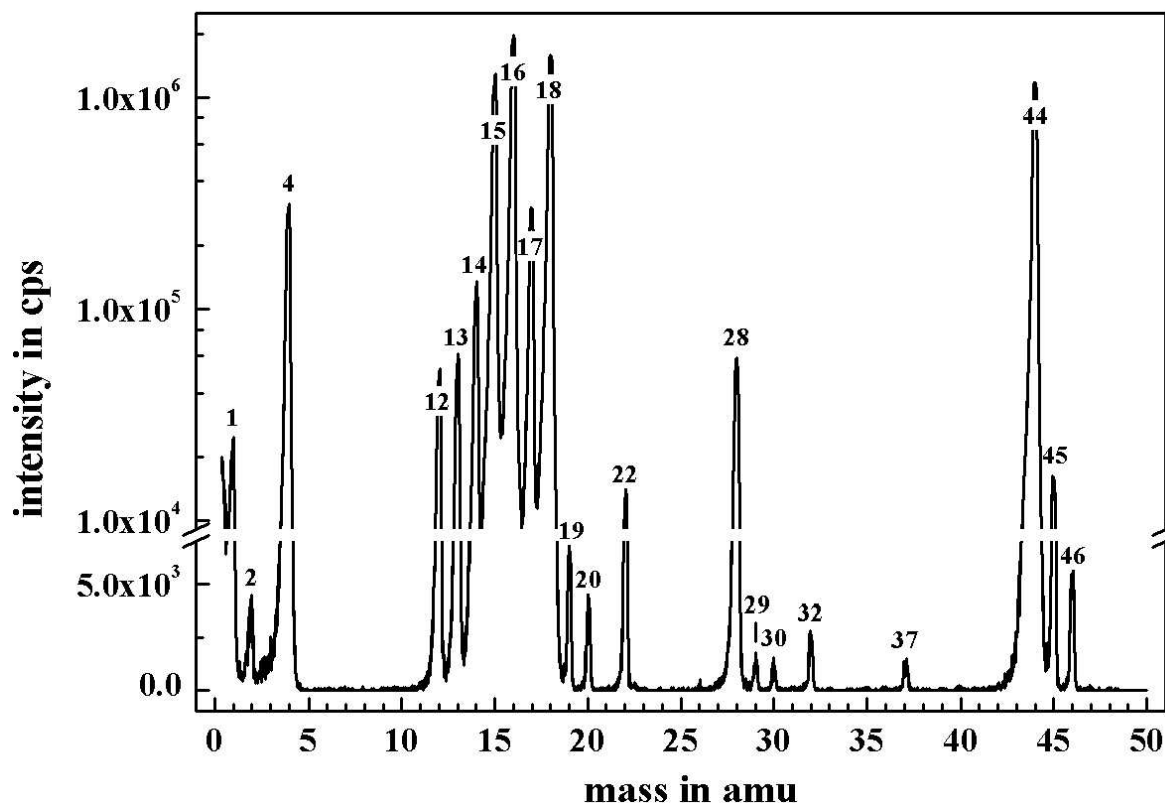


Figure 5.11: *Catalytic combustion of methane: $\dot{V} = 300 \text{ ml} \cdot \text{min}^{-1}$, $x_{\text{CH}_4} = 0.50$, $x_{\text{O}_2} = 0.13$, $x_{\text{He}} = 0.37$, $T_{\text{reactor}} = 438 \text{ }^\circ\text{C}$, mass spectrum 0.40 – 50.00 amu*

shown in Table 5.1, the mass spectrum provides no indication of any intermediate. All peaks can be explained by ions of the educts or products. The interpretation is clear for methanol CH_3OH (peak at 31 amu missing), for the hydroperoxo-radical $\text{HO}_2\cdot$ (peak at 33 amu missing), for hydrogen peroxide H_2O_2 (peak at 34 amu missing) and for the methylperoxo-radical $\text{CH}_3\text{OO}\cdot$ (peak at 47 amu missing). There are two small peaks at 29 amu and 30 amu which could be attributed to formaldehyde. However, a comparison with a mass spectrum of pure methane showed that these peaks belong to ethane, an impurity in the methane gas.

5.1.3 Appearance Potential Measurements

To decide about the presence or absence of methyl- and hydroxyl-radicals it is necessary to investigate the ionization efficiency curves at 15 amu and 17 amu respectively. However, the results from the foregoing section corroborate the hypothesis that the reaction is completed long before the sample is taken. Therefore, the appearance po-

tential measurements were performed with a total flow of $3000 \text{ ml} \cdot \text{min}^{-1}$ to reduce the mean residence time and to shift the reaction zone towards the sampling orifice. The obtained ionization efficiency curves are shown in Figure 5.12. The energy axis was corrected for instrumental corruption using the ionization potential of helium as internal standard (24.6 eV [108, page 4]). The assignment of the measured threshold values on the basis of literature values is summarized in Table 5.2. Consistent values are highlighted red.

Methyl radicals can be excluded as the measured threshold value of $13.7 \pm 0.6 \text{ eV}$ corresponds to the appearance potential of CH_3^+ from CH_4 ($14.01 \pm 0.08 \text{ eV}$ [155]). The assignment is unambiguous as the value of the ionization potential of the $\text{CH}_3\cdot$ radical ($9.84 \pm 0.03 \text{ eV}$ [154]) is sufficiently different. It is more difficult to assess the presence or absence of hydroxyl radicals as both $^1\text{H}^{16}\text{O}^+$ and $^{13}\text{C}^1\text{H}_4^+$ contribute to the signal at $m/z = 17 \text{ amu}$. Nevertheless, the onset of the corresponding **IE** curve at $12.3 \pm 0.6 \text{ eV}$ is within the margins of error in better agreement with the ionization potential of CH_4^+ ($12.63 \pm 0.02 \text{ eV}$ [155]) than with that of $\text{OH}\cdot$ ($13.18 \pm 0.1 \text{ eV}$ [99]). The sharp increase in slope at $18.9 \pm 0.6 \text{ eV}$ can be attributed to the appearance potential of OH^+ from H_2O ($18.2 \pm n.s. \text{ eV}$ [100]).

5.1.4 Conclusions

Recapitulating one can say that neither reactive radicals nor transient stable molecules could be detected for the catalytic combustion of methane. Observed are solely peaks of the reaction products as well as peaks from unconsumed educt molecules. The temperature programmed measurement indicates that our setup is probably not adapted to study this reaction because of the considerable distance between reaction zone and sampling nozzle. Flow variations were not successful to shift the reaction zone close to the nozzle as the reaction is not self-sustaining at the low catalyst temperatures at the tube end. Further problems arise from unspecific signal changes due to sudden changes in the chemical composition and condensation in the nozzle orifice.

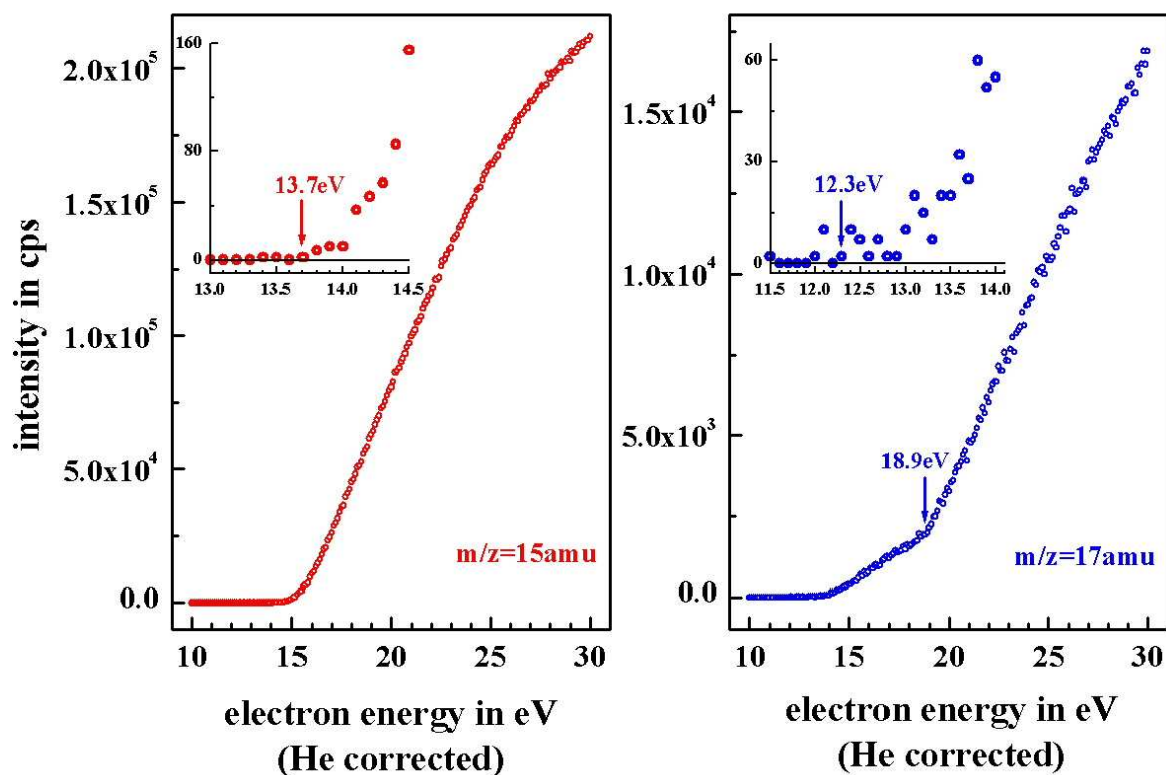


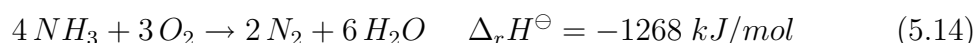
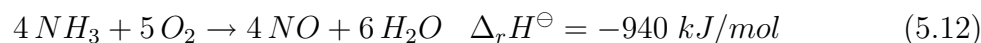
Figure 5.12: Catalytic combustion of methane: $\dot{V} = 3000 \text{ ml} \cdot \text{min}^{-1}$, $x_{\text{CH}_4} = 0.50$, $x_{\text{O}_2} = 0.13$, $x_{\text{He}} = 0.37$, $T_{\text{reactor}} = 450 \text{ }^\circ\text{C}$, **IE**-curves at 15 and 17 amu

Table 5.2: Assignment of the measured threshold values from Figure 5.12

species	15 amu (literature)	17 amu (literature)	15 amu (experiment)	17 amu (experiment)
$^{12}\text{C}^1\text{H}_3^+ / ^{12}\text{C}^1\text{H}_3\cdot$	$9.84 \pm 0.03 \text{ eV}$ [154]	-	-	-
$^{12}\text{C}^1\text{H}_3^+ / ^{12}\text{C}^1\text{H}_4$	$14.01 \pm 0.08 \text{ eV}$ [155]	-	$13.7 \pm 0.6 \text{ eV}$	-
$^{16}\text{O}^1\text{H}^+ / ^{16}\text{O}^1\text{H}\cdot$	-	$13.18 \pm 0.1 \text{ eV}$ [99]	-	-
$^{13}\text{C}^1\text{H}_4^+ / ^{13}\text{C}^1\text{H}_4$	-	$12.63 \pm 0.02 \text{ eV}$ [155]	-	$12.3 \pm 0.6 \text{ eV}$
$^{16}\text{O}^1\text{H}^+ / ^{16}\text{O}^1\text{H}_2$	-	$18.2 \pm n.s. \text{ eV}$ [100]	-	$18.9 \pm 0.6 \text{ eV}$

5.2 Ammonia Oxidation

The second reaction investigated was the *Pt* catalyzed oxidation of ammonia which leads to three different oxidation products depending on the reaction conditions (q.v. Section 2.3.2):



5.2.1 Temperature Programmed Measurements

The investigations on this reaction were started again with a temperature programmed experiment. The reactor was preheated to 200 °C and supplied with 500 ml · min⁻¹ of a mixture of 51 % NH₃, 39 % O₂ and 10 % Ar. This corresponds to the stoichiometry of reaction (5.14). The temperature was programmed to increase slowly (1 °C · min⁻¹) to 300 °C and to decrease afterwards (-1 °C · min⁻¹) to 20 °C. Each mass spectrum corresponds to a temperature interval of 2 °C. Figure 5.13 shows the evolution of nitrogen (peak area at 28 amu) which was the only reaction product at these conditions. A comparison between the programmed and the measured temperature is given in Figure 5.14 .

There are distinct differences between the temperature programmed experiments on the methane combustion and the ammonia oxidation. The NH₃/O₂ mixture used here shows a lower ignition temperature than the mixture used for the methane combustion. Whereas CO₂ production started not until 358 °C, N₂ is already detected from about 220 °C on. Such low ignition temperatures are characteristic for NH₃/O₂ mixtures which ignite nearly independent from composition around 200 °C [150].

Increasing the temperature further increases the nitrogen production until it culminates in an intensity jump up at about 240 °C. Figure 5.15 shows mass spectra around this point. The observed reactor runaway results again from the parametric sensitivity of the tubular reactor to highly exothermic reactions (cp. Section 5.1.1). The sudden conversion jump around 240 °C seems to occur on a level with the thermocouple tip as Figure 5.14 shows a pronounced temperature increase at this point.

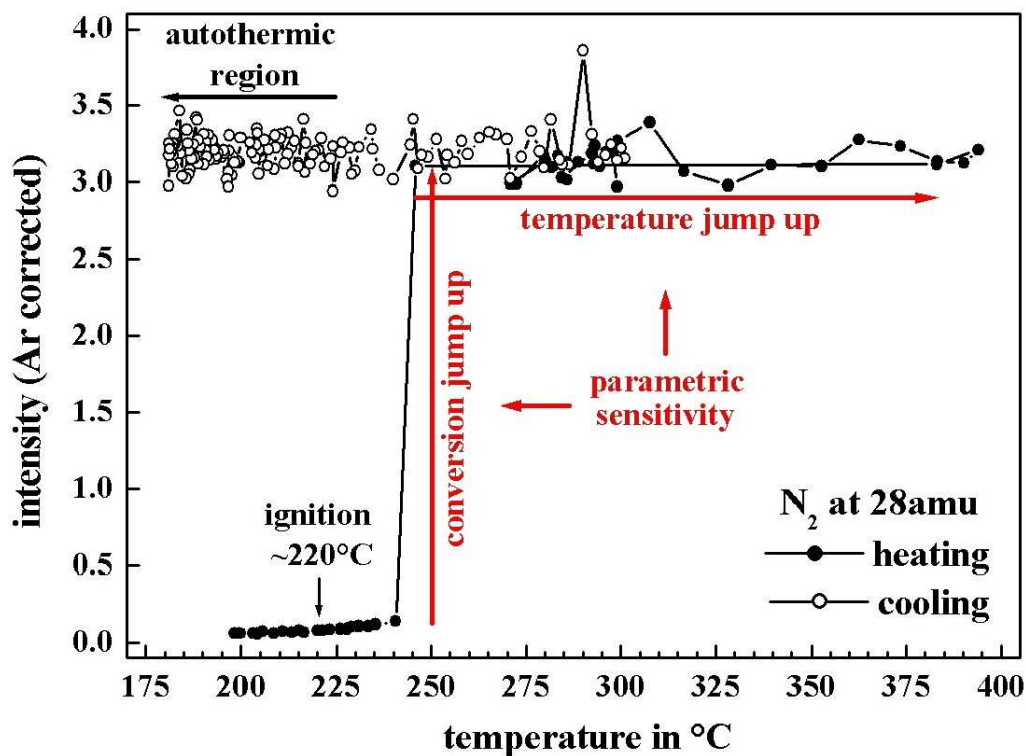


Figure 5.13: Ammonia oxidation: $\dot{V} = 500 \text{ ml} \cdot \text{min}^{-1}$, $x_{\text{NH}_3} = 0.51$, $x_{\text{O}_2} = 0.39$, $x_{\text{Ar}} = 0.10$, N_2 evolution during the temperature programmed experiment (Ar corrected signal intensities)

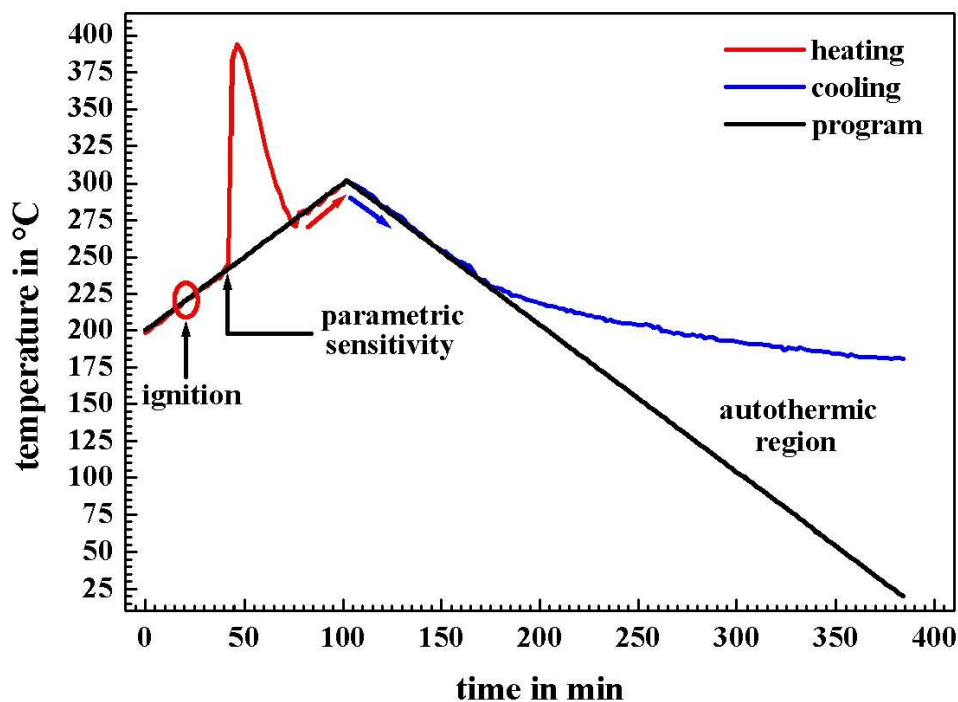


Figure 5.14: Ammonia oxidation: $\dot{V} = 500 \text{ ml} \cdot \text{min}^{-1}$, $x_{\text{NH}_3} = 0.51$, $x_{\text{O}_2} = 0.39$, $x_{\text{Ar}} = 0.10$, programmed and measured temperature curve

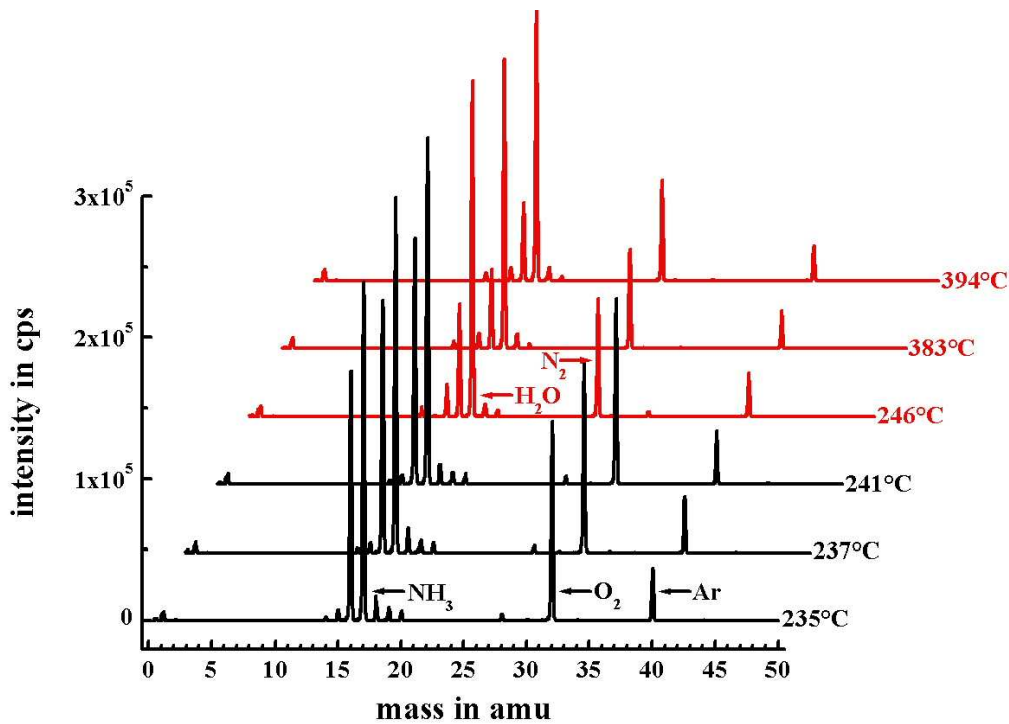


Figure 5.15: Ammonia oxidation: $\dot{V} = 500 \text{ ml} \cdot \text{min}^{-1}$, $x_{\text{NH}_3} = 0.51$, $x_{\text{O}_2} = 0.39$, $x_{\text{Ar}} = 0.10$, temperature programmed experiment, mass spectra in the parametric sensitive region around 240°C

This is in contrast to the methane combustion experiment where the thermocouple did not sense any temperature change at the point of maximum conversion (cp. Figure 5.3). However, a more detailed comparison of both experiments is omitted here because they were conducted at different compositions, different flows and different heating rates.

Much more important is the course of the temperature in the cooling branch of Figure 5.14 which indicates that the reactor runs autothermic below 225°C . Autothermic means that the reaction is self-sustaining without any external heating. As a consequence it should be possible to shift the reaction zone towards the nozzle just by increasing the flow rate. The ammonia oxidation should keep running as long as there is enough fuel and oxygen left. To determine a flow high enough for incomplete conversion, the temperature programmed experiment was repeated for total flows of 1000, 2000, 3000 and $4000 \text{ ml} \cdot \text{min}^{-1}$. Figure 5.16 shows the corresponding mass spectra after the conversion jump together with the temperature curves measured during the heating process. The experiment reveals the high reaction rate of the

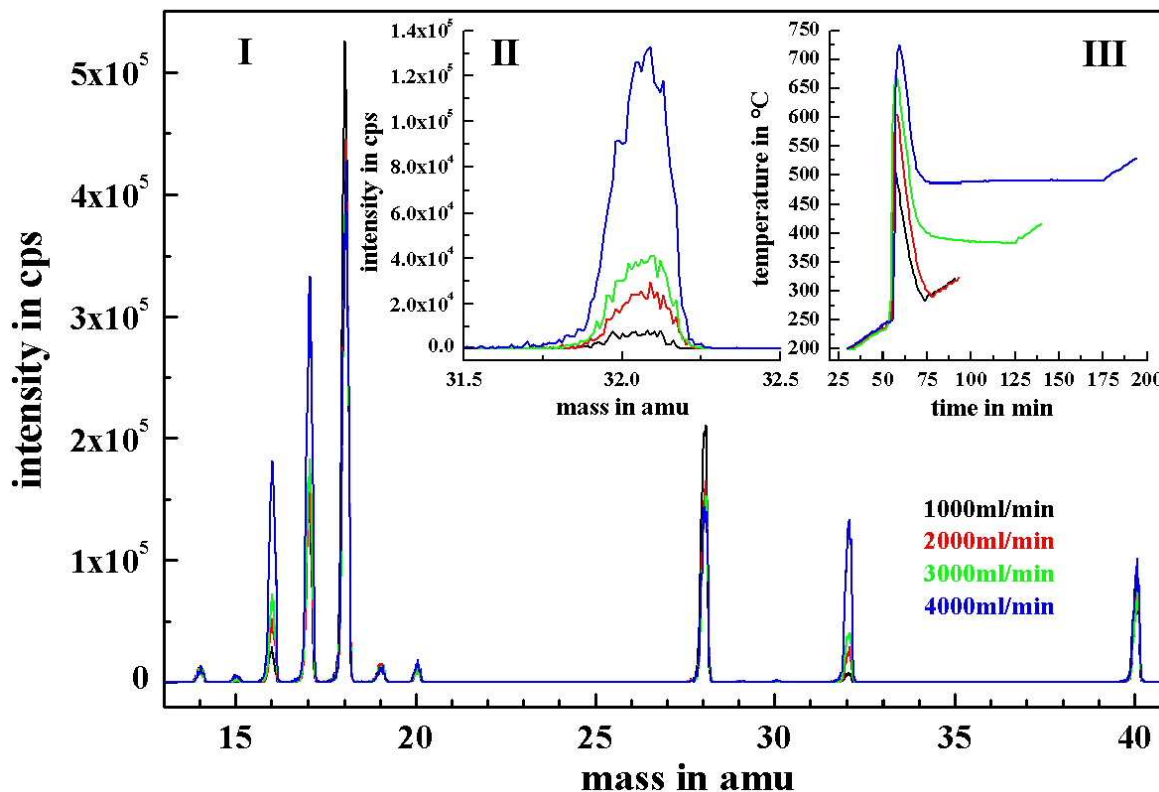


Figure 5.16: Ammonia oxidation: temperature programmed experiments for $\dot{V} = 1000, 2000, 3000$ and $4000 \text{ ml} \cdot \text{min}^{-1}$, I) mass spectra II) oxygen signal at 32 amu III) measured temperature curve

ammonia oxidation. A total flow of at least $2000 \text{ ml} \cdot \text{min}^{-1}$ is required to detect significant amounts of oxygen at the reactor outlet.

5.2.2 Mass Spectral Data

The temperature programmed experiments showed clearly that once the ammonia oxidation has started it can hardly be extinguished anymore except by removing one of the educts. This stability against composition changes and the possibility to shift the reaction zone close to the nozzle led to the idea to screen the reaction for intermediates across a wide range of compositions, temperatures and flows. The ammonia oxidation is especially suited for a screening because some of the expected intermediates would be identifiable immediately by means of their specific signals in a mass spectrum without requiring time consuming appearance potential measurements. To this group belong HNO at 31 amu, NH_2OH at 33 amu, NO_2 at

46 *amu* and HNO_2 at 47 *amu* (q.v. Section 2.3.2). An experimental design for mixtures has been used to carry out the screening efficiently. Figure 5.17 shows the design comprising seven mixtures with $NH_3/O_2/Ar$ compositions according to their triangular coordinates. Each of the seven mixtures was supplied to the reac-

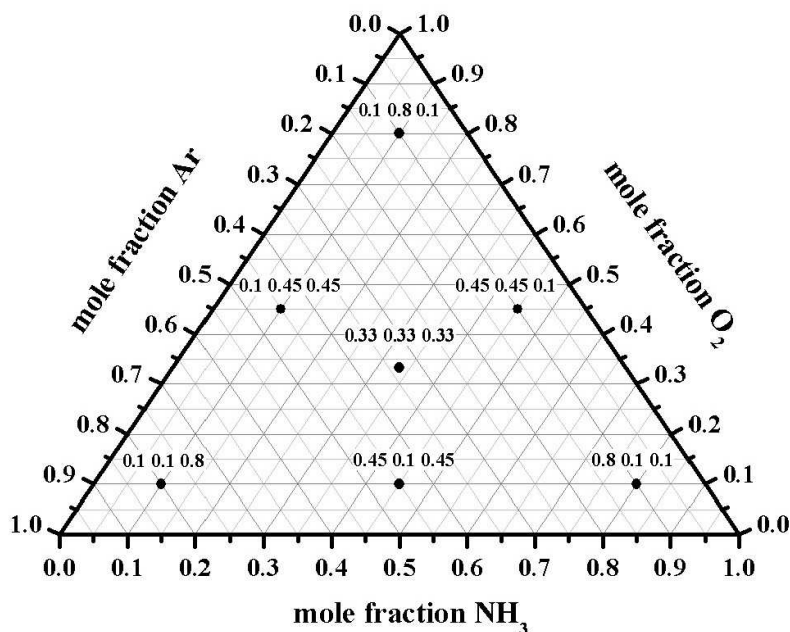


Figure 5.17: Ammonia oxidation: experimental design for $NH_3/O_2/Ar$ mixtures

tor both with a total flow of $500 \text{ ml} \cdot \text{min}^{-1}$ and $2000 \text{ ml} \cdot \text{min}^{-1}$. The influence of temperature was tested by conducting each experiment at $300 \text{ }^\circ\text{C}$ and at $1300 \text{ }^\circ\text{C}$. After two minutes equilibration time a mass scan from 0.40 – 50.00 *amu* has been recorded. The results are presented here exemplarily for the least diluted mixture with $x_{NH_3}/x_{O_2}/x_{Ar} = 0.45/0.45/0.10$. Figures 5.18 - 5.21 show the corresponding mass spectra for the four different temperature-flow combinations with the peaks assigned in Table 5.3. The intensity axis is normalized to the argon peak at 40 *amu* to correct unspecific signal variations. This is possible as the *Ar* concentration is approximately the same in all mixtures. Appearance potential measurements could not be performed to look for $\cdot NH\cdot$ and $OH\cdot$ radicals because there was a breakdown of the machine after the screening experiments which made it necessary to disassemble the setup. After reconstruction and fitting of a new reactor tube it was decided to proceed with the ammonia decomposition and to refrain from further measurements on the ammonia oxidation.

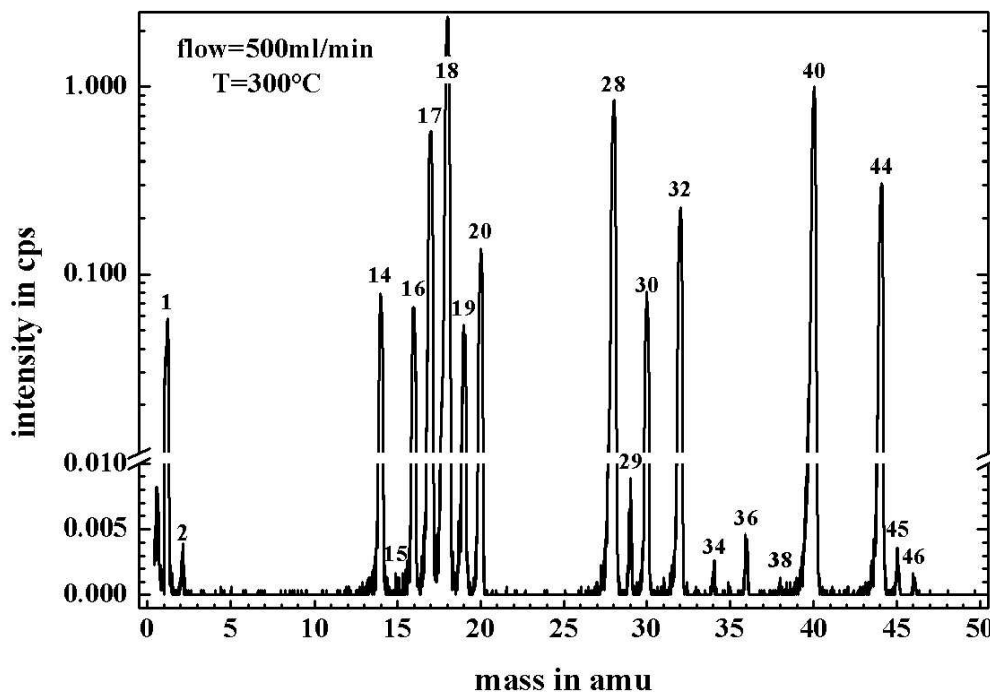


Figure 5.18: Ammonia oxidation: screening for intermediates, $x_{NH_3} = 0.45$, $x_{O_2} = 0.45$, $x_{Ar} = 0.10$, $\dot{V} = 500 \text{ ml} \cdot \text{min}^{-1}$, $T_{reactor} = 300 \text{ }^\circ\text{C}$

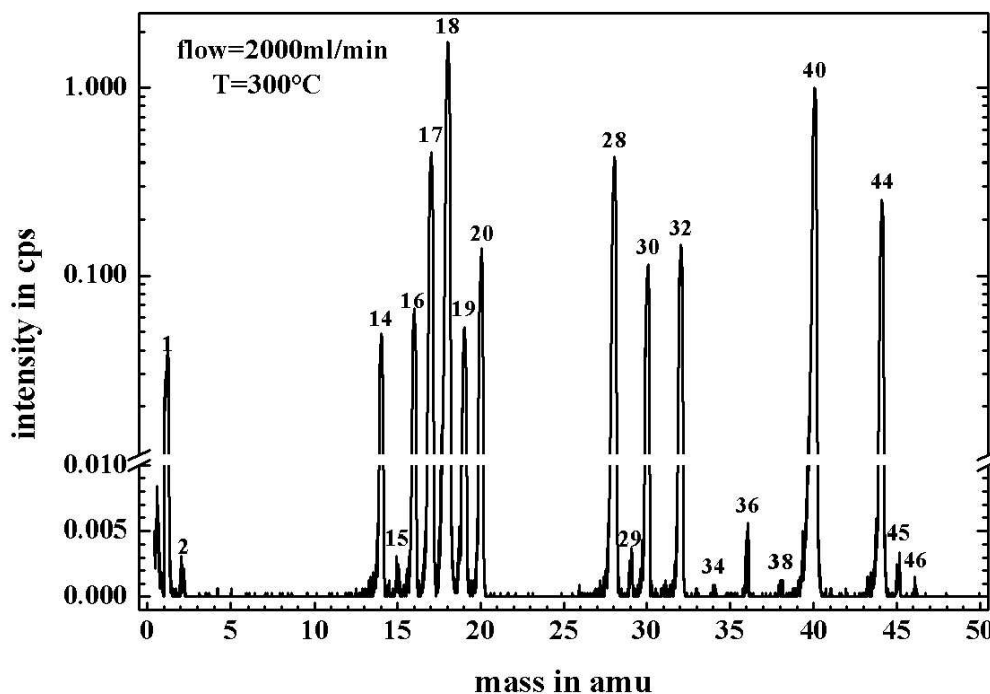


Figure 5.19: Ammonia oxidation: screening for intermediates, $x_{NH_3} = 0.45$, $x_{O_2} = 0.45$, $x_{Ar} = 0.10$, $\dot{V} = 2000 \text{ ml} \cdot \text{min}^{-1}$, $T_{reactor} = 300 \text{ }^\circ\text{C}$

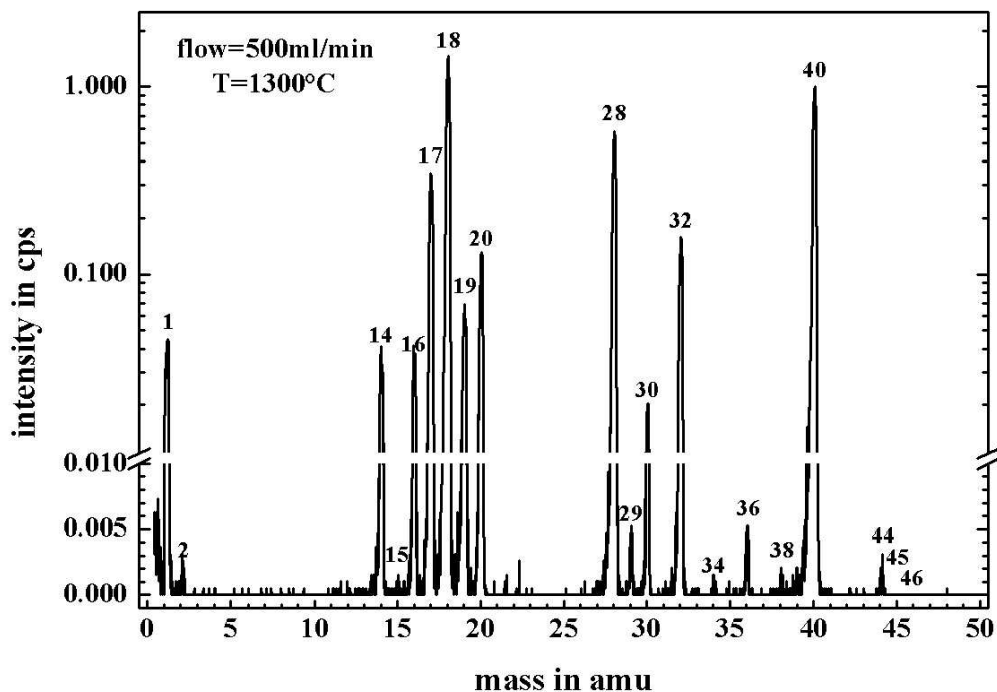


Figure 5.20: Ammonia oxidation: screening for intermediates, $x_{NH_3} = 0.45$, $x_{O_2} = 0.45$, $x_{Ar} = 0.10$, $\dot{V} = 500 \text{ ml} \cdot \text{min}^{-1}$, $T_{reactor} = 1300 \text{ }^\circ\text{C}$

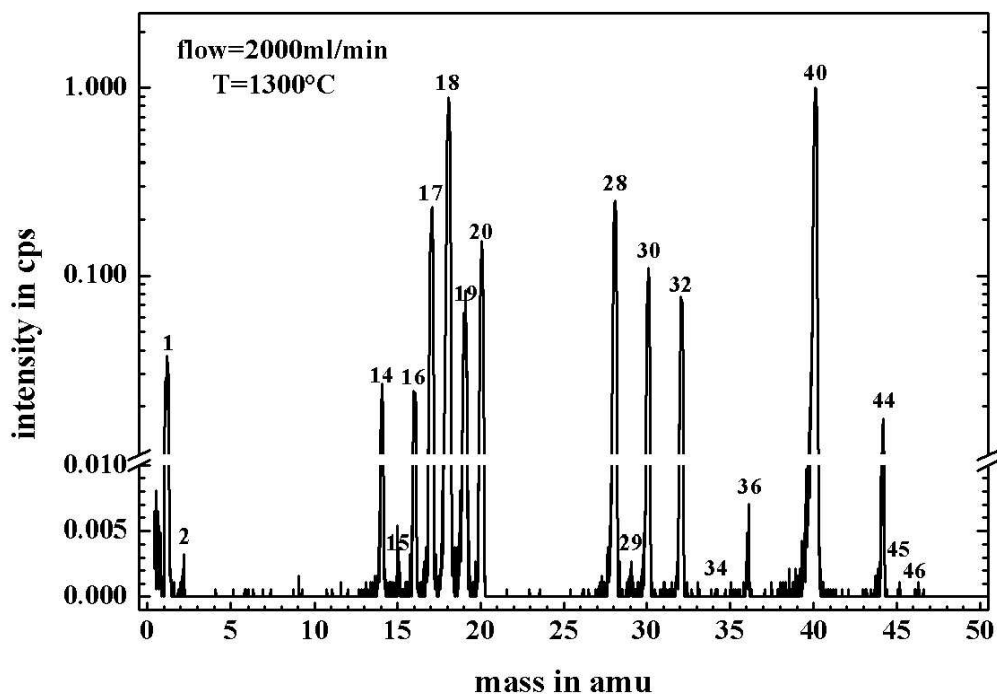


Figure 5.21: Ammonia oxidation: screening for intermediates, $x_{NH_3} = 0.45$, $x_{O_2} = 0.45$, $x_{Ar} = 0.10$, $\dot{V} = 2000 \text{ ml} \cdot \text{min}^{-1}$, $T_{reactor} = 1300 \text{ }^\circ\text{C}$

Table 5.3: Peak assignment table to the Figures 5.18 - 5.21, significant ions bold, expected species red

mass in amu	assignment	ion type	comment
1	$^1H^+$	fragment	-
2	$^1H_2^+$	parent	-
14	$^{14}N^+$	fragment	-
15	$^{14}N^1H^+$	fragment	-
	$^{14}N^{16}O^{++}$	parent	AP measurement required doubly charged
16	$^{14}N^1H_2^+$	fragment	-
	$^{16}O^+$	fragment	-
17	$^{14}N^1H_3^+$	parent	-
	$^{16}O^1H^+$	fragment radical ion?	- AP measurement required
18	$^{15}N^1H_3^+$	parent	isotopic peak
	$^{14}N^1H_4^+$	ion-molecule reaction	formed in ion source
	$^{16}O^1H_2^+$	parent	-
19	$^{16}O^1H_3^+$	ion-molecule reaction	formed in ion source
20	$^{40}Ar^{++}$	atomic ion	doubly charged
	$^{18}O^1H_2^+$	parent	isotopic peak
28	$^{14}N_2^+$	parent	-
29	$^{15}N^{14}N^+$	parent	isotopic peak
30	$^{14}N^{16}O^+$	parent	-
31	$^{14}N^{16}O^1H^+$	parent	not detectable
32	$^{16}O_2^+$	parent	-
33	$^{14}N^{16}O^1H_3^+$	parent	not detectable
34	$^{18}O^{16}O^+$	parent	isotopic peak
36	$^{36}Ar^+$	atomic ion	isotopic peak
38	$^{38}Ar^+$	atomic ion	isotopic peak
40	$^{40}Ar^+$	atomic ion	internal standard
44	$^{14}N_2^{16}O^+$	parent	-
45	$^{14}N^{15}N^{16}O^+$	parent	isotopic peak
46	$^{14}N_2^{18}O^+$	parent	isotopic peak
	$^{14}N^{16}O_2^+$	parent	not detectable
47	$^{14}N^{16}O_2^1H^+$	parent	not detectable

5.2.3 Conclusions

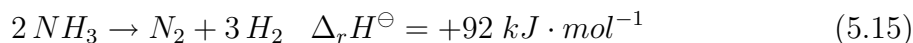
Although a flow of $2000 \text{ ml} \cdot \text{min}^{-1}$ should enable proper probing of the reaction zone, no non-radicalic intermediates were detected. Regardless of composition, temperature and flow, none of the recorded mass spectra shows a peak at 31, 33 or 47 *amu*. All observed peaks can be assigned to educt and product molecules or to the internal standard. The small peak in Figure 5.18 and 5.19 at 46 *amu* is due to the isotopic combination $^{14}\text{N}_2^{18}\text{O}^+$ and not to nitrogen dioxide $^{14}\text{N}^{16}\text{O}_2^+$.

This result is in disagreement with the early experiments of Bodenstein [60] who supposed to detected NH_2OH , HNO_2 and HNO_3 as transient species desorbing from the platinum catalyst in the ammonia oxidation (q.v. Section 2.3.2). However, the results agree with a work performed about thirty years later by Nutt and Kapur [156]. They studied the ammonia oxidation on a platinum ribbon at about the same pressure as Bodenstein (10^{-2} Torr) by sampling the species which evaporate from the catalyst surface using molecular beam mass spectrometry. No peaks at masses corresponding to any of the postulated intermediates have been found in their work. As the samples analyzed in the present experiments can be considered representative for the reaction zone, the latter result is confirmed for atmospheric pressure as well. It might be the case that some of the intermediates proposed in the pioneering works of Andrussow, Raschig and Bodenstein appear on the catalyst surface but then they are consumed very rapidly and do not desorb into the gas phase.

The assumption of a purely heterogenous mechanism for the ammonia oxidation is also corroborated by more recent works published in literature. For example, Rebrov et al. used an exclusively heterogenous microkinetic model to predict nicely selectivities and product yields for the ammonia oxidation over supported polycrystalline platinum in an aluminium-based microreactor [157]. Another example was found from Pignet and Schmidt who studied the kinetics of the NH_3 oxidation on platinum at a total pressure between 0.1 and 1 *Torr* and from 200 to 1500 $^\circ\text{C}$ [158]. They found exclusively NO and N_2 as oxidation products with production rates described well by Langmuir-Hinshelwood rate expressions. An isothermal stirred tank reactor model was then used to extrapolate the kinetic model to realistic reaction conditions. It was possible by means of this extrapolation to predict correctly conversions and selectivities for atmospheric pressure. If this purely heterogenous model was wrong it would hardly apply in an extrapolation.

5.3 Ammonia Decomposition

The ammonia decomposition into the elements has been chosen as third test reaction to bridge the gap between the exothermic oxidation reactions and the highly endothermic **BMA** reaction:



The reaction was especially suited for testing purposes because it was previously studied using threshold ionization mass spectrometry [28]. The authors studied the ammonia decomposition over a pressure range from 0.1 to 1 *Torr* and from 50 to 1100 °C. They reported several radicals whereby $NH_2\cdot$ was the most abundant (q.v. Section 2.3.3). The $NH_2\cdot$ production starts already at about 450 °C, increases continuously with temperature up to 1000 °C where it levels off finally. It was the question if similar results could be obtained for atmospheric pressure as well.

5.3.1 Mass Spectral Data

The measurements in the present work were conducted feeding a mixture of 400 $ml \cdot min^{-1}$ NH_3 and 100 $ml \cdot min^{-1}$ Ar to the reactor at room temperature (20 °C) and at 650 and 1300 °C respectively. As the reaction is endothermic, a temperature programmed experiment was not performed. Figure 5.22 shows the corresponding mass spectra with the peaks assigned in Table 5.4.

Already the spectrum at 650 °C shows a measurable ammonia decomposition indicated by the small peaks at 2 and 28 *amu*. This medium temperature has been chosen in hope that potentially arising radicals do not decompose too fast before sampling. The spectrum at 1300 °C shows that ammonia decomposition has occurred to a large extent. It is not possible to quantify the reaction on the basis of the mass spectral data alone as the sampling process and hence the signal intensities depend strongly on the temperature in front of the nozzle (q.v. Equation 5.6) and a standardization is not possible here because the standard becomes diluted by progress of Reaction (5.15).

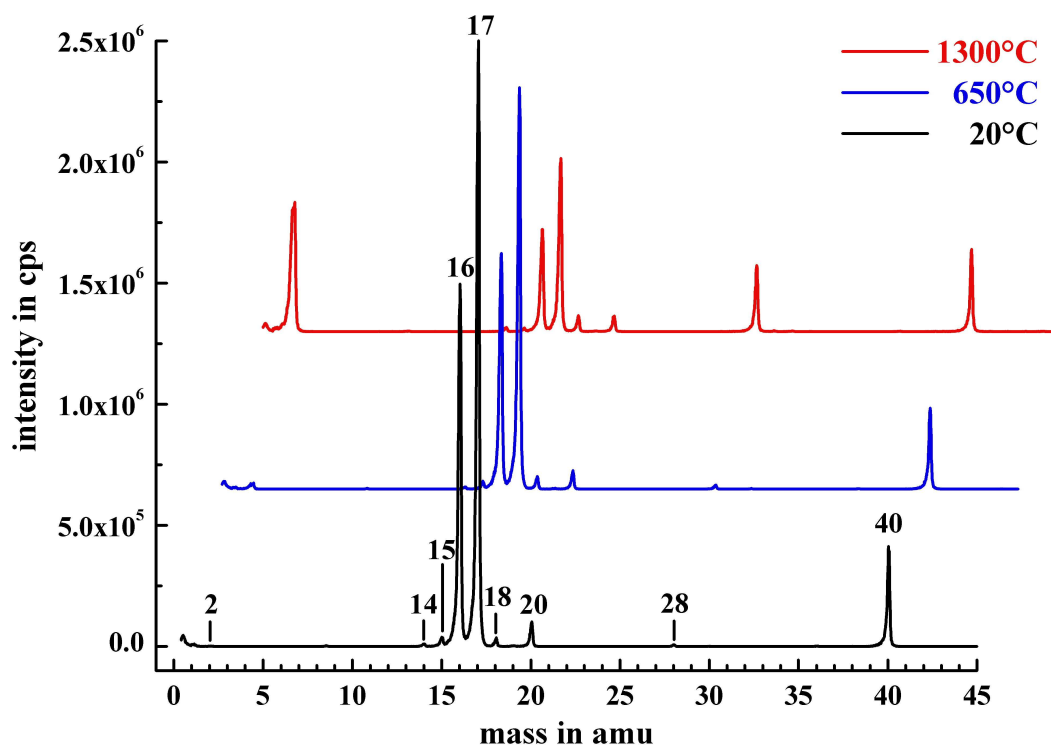


Figure 5.22: Ammonia decomposition: $\dot{V} = 500 \text{ ml} \cdot \text{min}^{-1}$, $x_{\text{NH}_3} = 0.80$, $x_{\text{Ar}} = 0.20$, mass spectra for $T_{\text{reactor}} = 20, 650$ and $1300 \text{ }^\circ\text{C}$

Table 5.4: Peak assignment table to Figure 5.22, significant ions bold, expected species red

mass in amu	assignment	ion type	comment
2	$^1\text{H}_2^+$	parent	-
14	$^{14}\text{N}^+$	fragment radical ion?	- AP measurement required
15	$^{14}\text{N}^1\text{H}^+$	fragment radical ion?	- AP measurement required
16	$^{14}\text{N}^1\text{H}_2^+$	fragment radical ion?	- AP measurement required
17	$^{14}\text{N}^1\text{H}_3^+$	parent	-
18	$^{15}\text{N}^1\text{H}_3^+$ $^{14}\text{N}^1\text{H}_4^+$	parent ion-molecule reaction	isotopic peak formed in ion source
20	$^{40}\text{Ar}^{++}$	atomic ion	doubly charged
28	$^{14}\text{N}_2^+$	parent	-
40	$^{40}\text{Ar}^+$	atomic ion	internal standard

5.3.2 Appearance Potential Measurements

The only function of the argon standard in these experiments is to calibrate the energy axis for the appearance potential measurements. These have been performed by recording a nearly base line separated full profile mass spectrum for each setting of the electron energy. The corresponding **IE**-curves were then obtained by plotting the peak areas against the argon standardized energy values. This procedure, although much more time consuming than the common monitoring of a single m/z -value against the electron energy, supplies better **IE**-curves and can be used here because the signals are time stable in contrast to the exothermic reactions (no condensation!). Figure 5.23 shows the results for the peaks at 16, 15 and 14 amu . The long arrows which extend over all **IE**-curves at a particular mass mark the ionization potentials of the expected radicals as reported in the literature [159, 160, 161]. The short arrows indicate the onset values of the curves as determined by the vanishing current method (q.v. Section 3.3.4).

5.3.3 Conclusions

The obtained **IE**-curves show again no indication for any of the expected radicals. Except for one, all measured threshold values can be assigned to the appearance potentials of the corresponding ions from ammonia. Only the onset of the curve at 14 amu and 1300 °C has to be attributed to the formation of N^+ from N_2 because most of the ammonia is decomposed and has beyond only a marginal fragmentation into N^+ (q.v. Figure 5.22). Table 5.5 summarizes these results.

The direct comparison of the **IE**-curves in Figure 5.23 shows that the determination of the onset values is straightforward for the curves at 16 amu but becomes more and more subjective for the curves at 15 and 14 amu . One reason for that is that the **IE**-curves for NH^+ and N^+ approach the energy axis with more curvature than that for NH_2^+ . This is characteristic for ions formed by a fragmentation process which involves multiple-bond breaking (q.v. Section 3.3.4). Another reason is the limited mass resolution of the quadrupole mass filter which leads even at optimum performance to a small transfer of counts from adjacent peaks. In this case, the onset point was taken at the position where the curve deviates significantly from the lin-

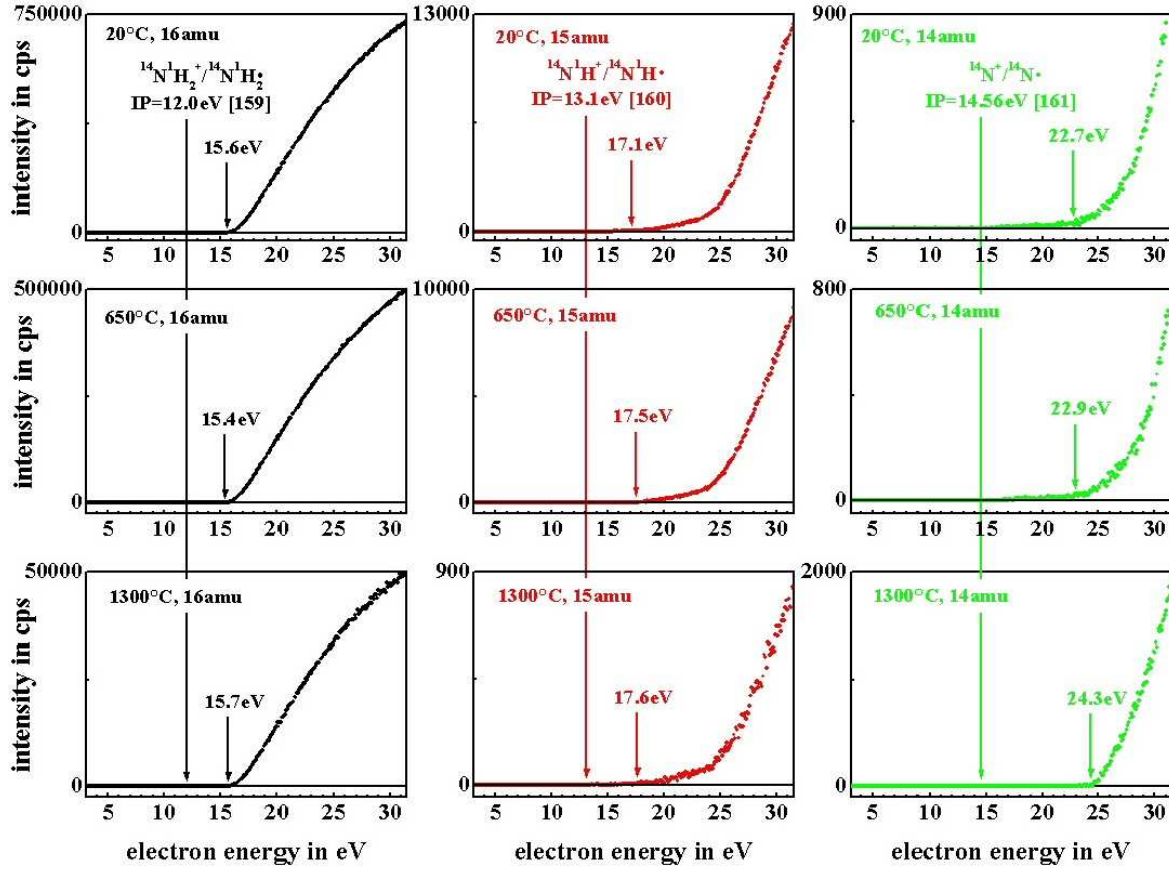


Figure 5.23: Ammonia decomposition: $\dot{V} = 500 \text{ ml} \cdot \text{min}^{-1}$, $x_{NH_3} = 0.80$, $x_{Ar} = 0.20$, **IE**-curves at 16, 15 and 14 amu, $T_{reactor} = 20, 650$ and $1300 \text{ }^\circ\text{C}$

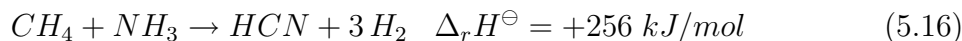
Table 5.5: Assignment of the measured threshold values from Figure 5.23

m/z in amu	temperature in $^\circ\text{C}$	AP in eV (experiment)	assignment	AP in eV (literature)	reference
16	20	15.6 ± 0.6	$^{14}\text{N}^1\text{H}_2^+ / ^{14}\text{N}^1\text{H}_3$	15.76 ± 0.05	[159]
	650	15.4 ± 0.6			
	1300	15.7 ± 0.6			
15	20	17.1 ± 0.6	$^{14}\text{N}^1\text{H}^+ / ^{14}\text{N}^1\text{H}_3$	16.9 ± 0.1	[159]
	650	17.5 ± 0.6			
	1300	17.6 ± 0.6			
14	20	22.7 ± 0.6	$^{14}\text{N}^+ / ^{14}\text{N}^1\text{H}_3$	22.6 ± 0.1	[162]
	650	22.9 ± 0.6			
	1300	24.3 ± 0.6	$^{14}\text{N}^+ / ^{14}\text{N}_2$	24.34 ± 0.20	[163]

early raising background. Notwithstanding these limitations, all experimental values agree within the precision of measurements with the literature and the absence of radicals can be deduced with sufficient reliability. The measurements have also been repeated for a total flow of $2500 \text{ ml} \cdot \text{min}^{-1}$ but since the results were equivalent they are not shown here. The general question, if it would have been possible to detect radicals in this reaction, will be discussed in Chapter 6.

5.4 Hydrocyanic Acid from Methane and Ammonia

The last reaction investigated was the formation of hydrocyanic acid from methane and ammonia, the so called **BMA**-reaction:



Before presenting mass spectra and **IE**-curves, some expectations regarding gas phase intermediates shall be recapitulated here. As already reported in Section 2.3.4, there are essentially two mechanisms published for the oxygen free *HCN* formation over platinum. The mechanism proposed by Pfeil and Hoffmann [65] discusses *NH* (imidogen), *CH₃NH₂* (methylamine) and *CH₂=NH* (methylenimine) as potential intermediates towards *HCN* but no information is given in this work whether these species exist exclusively on the catalyst surface or if they can also escape to the gas phase. More concrete statements in this regard are made in the work published by Diefenbach et al. where the dehydrogenation of *CH₂=NH* to *HCN* was reported to be the only step proceeding homogeneously in the gas phase. Besides looking for intermediates that are involved in the formation of *HCN* itself likewise interesting are those leading to the formation of soot. Of special interest are thereby hydrocarbon radicals like for instance *CH₃·*.

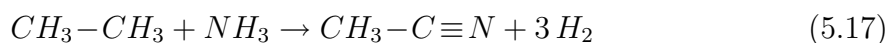
5.4.1 Mass Spectral Data

All measurements concerning this reaction have been performed with the reactor at its maximum temperature of 1300 °C and with an additional nitrogen purging of 25 ml · min⁻¹ (q.v. reactor construction shown in Figure 4.4). The purging was required to avoid a coking of the glowing heater by contact with reactor off-gases. To prevent contact of the catalyst with air the heating up was done under a flow of 300 ml · min⁻¹ N₂. After reaching the final temperature, the feed was switched to 250 ml · min⁻¹ NH₃. In contrast to all other reactions studied up to now a reference method was used here to quantify the off-gas composition of the reactor. This was done using a non-dispersive infrared analyzer (type NGA2000, Rosemount) with channels for *HCN*, *NH₃* and *CH₄*.

A monitoring of the off-gas composition was required for the **BMA**-experiments as stable long time operation conditions had to be found with a high *HCN* yield on

one hand and without a risk of coking of the catalyst on the other hand. Numerous experiments have been performed to find a good compromise for our bench-scale reactor. The mixture that could be finally used to record the mass spectra and the **IE**-curves consisted of $300 \text{ ml} \cdot \text{min}^{-1} \text{ NH}_3$, $150 \text{ ml} \cdot \text{min}^{-1} \text{ CH}_4$ and $50 \text{ ml} \cdot \text{min}^{-1} \text{ He}$ as internal standard. In other words, about 100 % ammonia excess was necessary to enable stable long time operation. Even under these conditions the methane conversion and equal to that the yield of *HCN* based on CH_4 was only $X_{\text{CH}_4} = Y_{\text{HCN}/\text{CH}_4} \approx 74 \%$. The yield of *HCN* based on NH_3 was correspondingly lower ($Y_{\text{HCN}/\text{NH}_3} \approx 37 \%$). The commercial process for comparison employs only a slight excess of ammonia ($x_{\text{NH}_3}/x_{\text{CH}_4} \simeq 1.1$) and supplies *HCN* yields of more than 90 % for CH_4 and between 80 – 85 % for NH_3 . The instability of our laboratory reactor with respect to coking could not be explained up to now but its smoothly varying temperature profile (cp. Figure 4.6) is assumed to be one important reason. The technical reactor shows a well-defined reaction zone with a sharp rise of temperature at the inlet and a likewise sharp temperature drop at the outlet [164]. However, the conversion achieved with our reactor was sufficient to study the reaction mass spectrometrically. Figure 5.24 shows a mass spectrum recorded under the conditions described above and Table 5.6 lists the observed peaks and their assignment.

In contrast to the mass spectra obtained for all other reactions studied the spectrum for the **BMA**-reaction shows several unexpected peaks which necessitate a closer examination. The peaks at 19 amu ($^1\text{H}_3^{16}\text{O}^+$) and 32 amu ($^{16}\text{O}_2^+$) are caused by traces of water and oxygen respectively which are stored from previous measurements in the isolation material of the reactor and are flushed out now by the nitrogen purging. Due to the construction of the reactor, the purging gas can be sampled to a small extent but it can not participate in the reaction (q.v. Figure 4.4). The small peak at 30 amu is probably due to ethane because the methane used for the experiments contains traces of higher hydrocarbons (concentration of other C_nH_m than CH_4 certified to be $\leq 300 \text{ ppm}$). The presence of C_2 hydrocarbons could also explain the peaks from $38 - 41 \text{ amu}$ as a reaction of them with ammonia would lead to the formation of acetonitrile ($m/z = 41 \text{ amu}$):



This assumption was verified by recording a mass spectrum at highest sensitivity from

Table 5.6: Assignment table to Figure 5.24, significant ions bold, expected species red

mass in amu	assignment	ion type	comment
1	$^1H^+$	fragment	-
2	$^1H_2^+$	parent	-
4	$^4He^+$	atomic ion	internal standard
12	$^{12}C^+$	fragment	-
13	$^{12}C^1H^+$	fragment	-
13.5	$^{12}C^{14}N^1H^{++}$	parent	doubly charged
14	$^{12}C^1H_2^+$	fragment	-
	$^{14}N^+$	fragment	-
15	$^{12}C^1H_3^+$	fragment radical ion?	- AP measurement required
	$^{14}N^1H^+$	fragment radical ion?	- AP measurement required
16	$^{12}C^1H_4^+$	parent	-
	$^{14}N^1H_2^+$	fragment radical ion?	- AP measurement required
17	$^{14}N^1H_3^+$	parent	-
	$^{13}C^1H_4^+$	parent	isotopic peak
18	$^{14}N^1H_4^+$	ion-molecule reaction	formed in ion source
	$^{15}N^1H_3^+$	parent	isotopic peak
	$^{16}O^1H_2^+$	parent	contamination
19	$^{16}O^1H_3^+$	ion-molecule reaction	formed in ion source
26	$^{12}C^{14}N^+$	fragment	-
27	$^{12}C^{14}N^1H^+$	parent	-
28	$^{14}N_2^+$	parent	-
	$^{13}C^{14}N^1H^+$	parent	isotopic peak
	$^{12}C^{15}N^1H^+$	parent	isotopic peak
29	$^{14}N^{15}N^+$	parent	isotopic peak
	$^{12}C^{14}N^1H_3^+$	parent	AP measurement required
	$^{12}C_2^1H_5^+$	fragment	contamination
30	$^{12}C_2^1H_6^+$	parent	contamination
	$^{12}C^{14}N^1H_4^+$	fragment	AP measurement required
31	$^{12}C^{14}N^1H_5^+$	parent	not detectable
32	$^{16}O_2^+$	parent	contamination
38 – 44	$^{12}C_3^1H_2^+ - ^{12}C_3^1H_8^+$	fragment, parent	AP measurements required
	$^{12}C_2^{14}N^+ - ^{12}C_2^{14}N^1H_6^+$	fragment, parent	AP measurements required

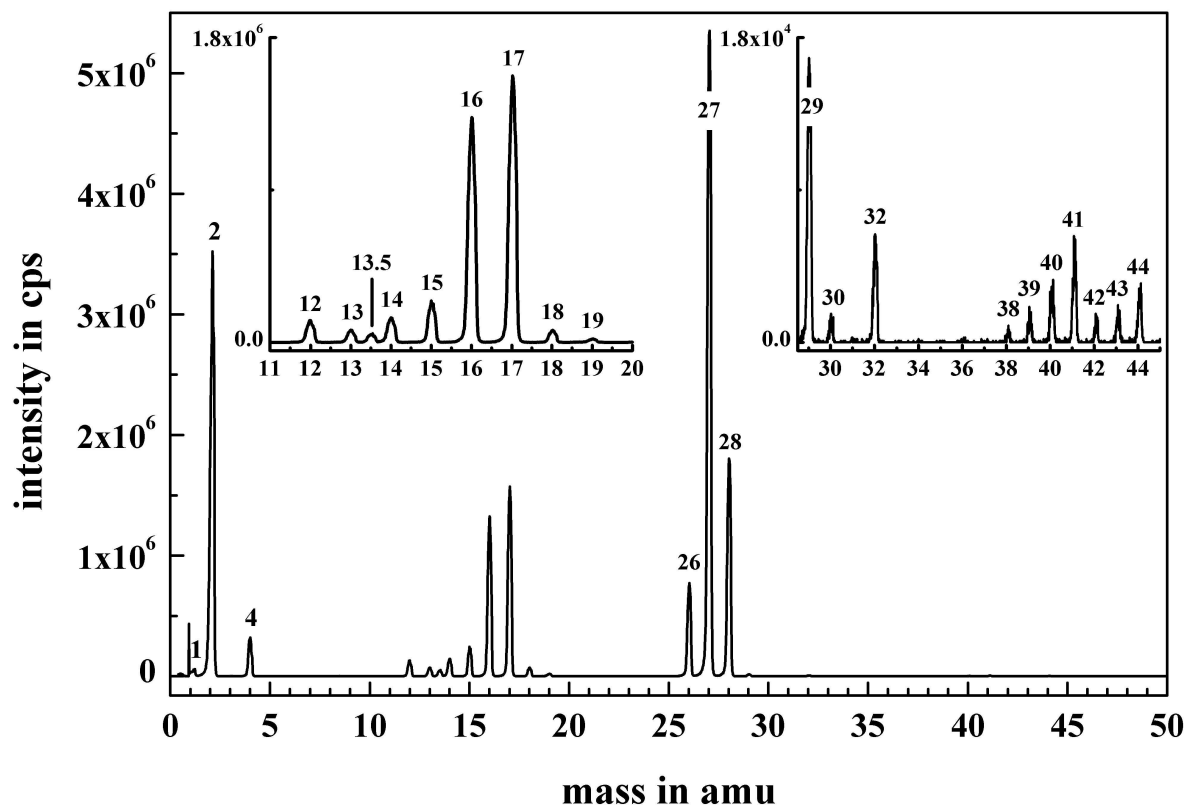


Figure 5.24: BMA-reaction: $\dot{V} = 500 \text{ ml} \cdot \text{min}^{-1}$, $x_{\text{NH}_3} = 0.60$, $x_{\text{CH}_4} = 0.30$, $x_{\text{He}} = 0.10$, mass spectrum for for $T_{\text{reactor}} = 1300 \text{ }^\circ\text{C}$

30–100 *amu*. The high intensity peaks below 30 *amu* could not be scanned with these settings of the spectrometer as this would damage the SEM detector. Figure 5.25 shows the obtained mass spectrum together with a spectrum of acetonitrile taken from literature [165]. Indeed, there is a good match between the acetonitrile spectrum and the peaks from 38 – 41 *amu* (C_2NH_x , $x = 0 - 3$). The peaks from 42 – 44 *amu* might either be assigned to hydrogenated species of acetonitrile or more likely to propane and its fragments. The spectrum shows further peaks from 50 – 58 *amu* and from 64 – 70 *amu* which indicate traces of several other higher molecular species. It can not be concluded definitely whether these molecules are formed by the reaction of impurities (ethane, propane etc.) with ammonia (similar Equation (5.17)) or if they arise from *C* – *C* bond formation reactions of *C*₁ components during the BMA-mechanism. The last-mentioned reaction path would then be the first step towards carbon black formation frequently observed in the practical operation of BMA-reactors.

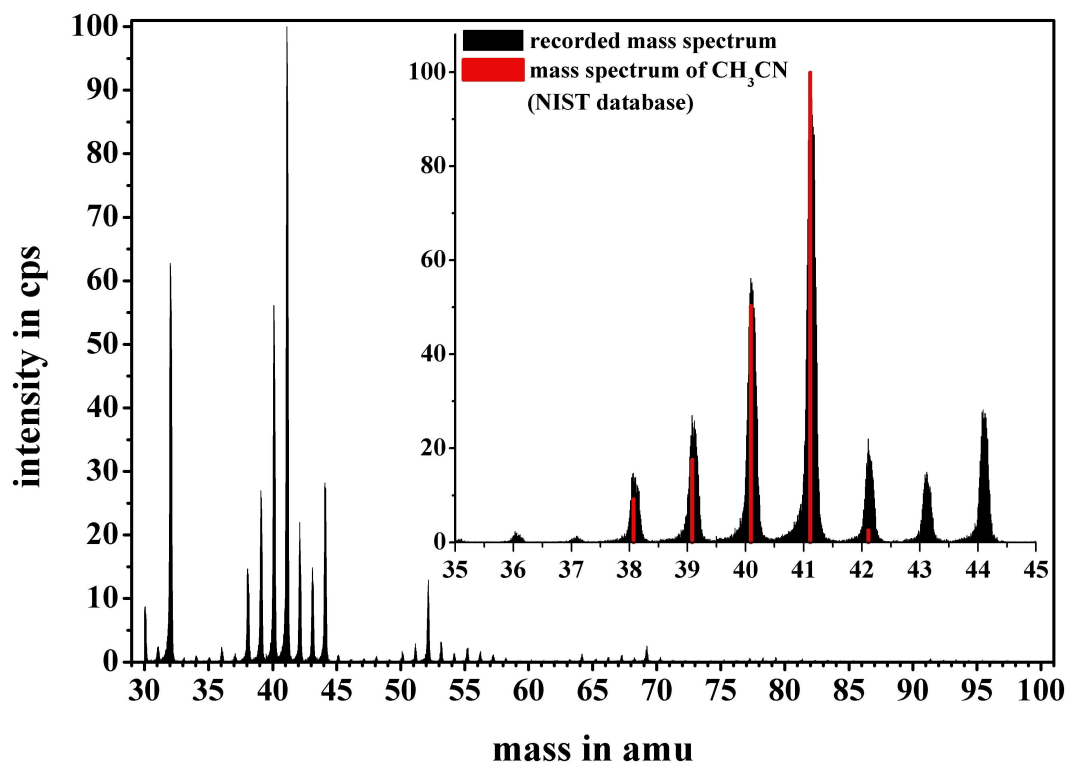


Figure 5.25: *BMA*-reaction: $\dot{V} = 500 \text{ ml} \cdot \text{min}^{-1}$, $x_{\text{NH}_3} = 0.60$, $x_{\text{CH}_4} = 0.30$, $x_{\text{He}} = 0.10$, $T_{\text{reactor}} = 1300 \text{ }^\circ\text{C}$, high sensitivity mass spectrum from 30 – 100 *amu*, comparison with a literature spectrum of acetonitrile [165]

The only intermediate on which can be concluded immediately from the mass spectra is methylamine by its peak at 31 *amu*. This peak is only observable in Figure 5.25 at very high sensitivity. However, the peak is too high to be an isotopic peak ($^{13}\text{C}^{12}\text{C}^1\text{H}_6^+$) from mass 30 *amu* and can hence either be a fragment of one of the larger molecules or the molecular peak of methylamine. Unfortunately its intensity is not sufficient for an appearance potential measurement so one has to consult the **IE**-curve at 30 *amu*. Statements about the other species labelled red in Table 5.6 require the corresponding **IE**-curves as well.

5.4.2 Appearance Potential Measurements

Figure 5.26 shows a selection of relevant **IE**-curves measured for the *BMA*-reaction under the experimental conditions described in the foregoing section. The assignments of the determined threshold values is summarized in Table 5.7. The curves were again obtained by recording full profile mass spectra and plotting the peak ar-

eas against the electron energy. This procedure requires long time measurements (several hours) but reduces the scatter in the curves conspicuously, a prerequisite to determine threshold values for low intensity peaks.

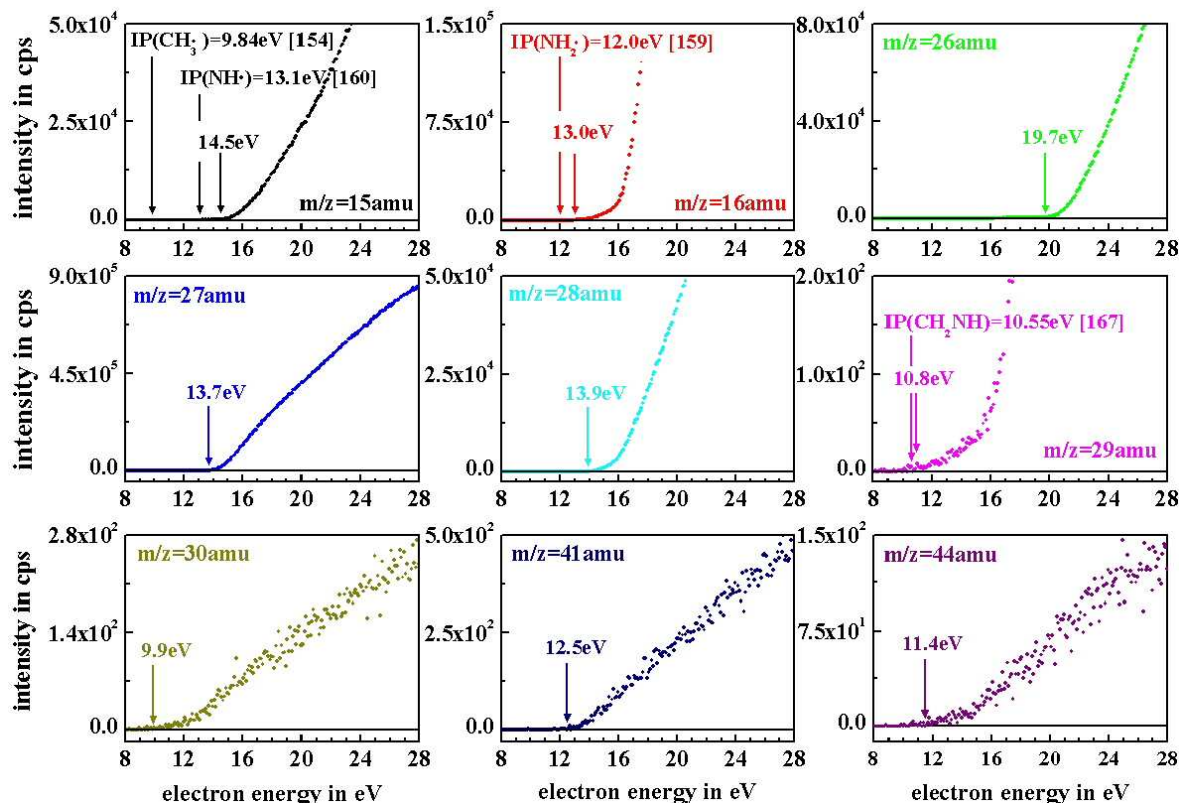


Figure 5.26: *BMA*-reaction: $\dot{V} = 500 \text{ ml} \cdot \text{min}^{-1}$, $x_{\text{NH}_3} = 0.60$, $x_{\text{CH}_4} = 0.30$, $x_{\text{He}} = 0.10$, $T_{\text{reactor}} = 1300 \text{ }^\circ\text{C}$, *IE*-curves at 15, 16, 26, 27, 28, 29, 30, 41 and 44 *amu*

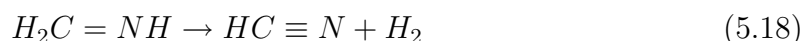
The *IE*-curves at 15 and 16 *amu* do not show any indication for radicals because their onset values of 14.5 *eV* and 13.0 *eV* are respectively too high to match the ionization potential of one of the radicals. The curves at 26 and 27 *amu*, corresponding to $^{12}\text{C}^{14}\text{N}^+$ and $^1\text{H}^{12}\text{C}^{14}\text{N}^+$, are given here to document that the appearance- and ionization potentials obtained by the vanishing current method agree within the precision of the measurements with literature values (q.v. Table 5.7). This is important to rely on assignments for less unambiguous values as for example that obtained for 28 *amu*. This mass is by orders of magnitude dominated by $^{14}\text{N}_2^+$ but the measured threshold value corresponds to the lower ionization potential of hydrocyanic acid which has two isotopic combinations at this mass ($^1\text{H}^{13}\text{C}^{14}\text{N}^+$ and $^1\text{H}^{12}\text{C}^{15}\text{N}^+$).

The remaining four *IE*-curves at 29, 30, 41 and 44 *amu* are more difficult to ana-

Table 5.7: Assignment of the measured threshold values from Figure 5.26

m/z in amu	AP in eV (experiment)	assignment	AP in eV (literature)	reference
15	14.5 ± 0.6	$^{12}\text{C}^1\text{H}_3^+ / ^{12}\text{C}^1\text{H}_4$	14.01 ± 0.08	[155]
16	13.0 ± 0.6	$^{12}\text{C}^1\text{H}_4^+ / ^{12}\text{C}^1\text{H}_4$	12.63 ± 0.02	
26	19.7 ± 0.6	$^{12}\text{C}^{14}\text{N}^+ / ^1\text{H}^{12}\text{C}^{14}\text{N}$	20.1 ± 0.2	[166]
27	13.7 ± 0.6	$^1\text{H}^{12}\text{C}^{14}\text{N}^+ / ^1\text{H}^{12}\text{C}^{14}\text{N}$	13.7 ± 0.1	
28	13.9 ± 0.6	$^1\text{H}^{13}\text{C}^{14}\text{N}^+ / ^1\text{H}^{13}\text{C}^{14}\text{N}$	13.7 ± 0.1	
29	10.6 ± 0.6	$^{12}\text{C}^{14}\text{N}^1\text{H}_3^+ / ^{12}\text{C}^1\text{H}_2^{14}\text{N}^1\text{H}$	$10.55 \pm n.s.$	[167]
30	9.9 ± 0.6	$^{12}\text{C}^{14}\text{N}^1\text{H}_4^+ / ^{12}\text{C}^1\text{H}_3^{14}\text{N}^1\text{H}_2$	10.18 ± 0.07	[168]
41	12.5 ± 0.6	$^{12}\text{C}_2^{14}\text{N}^1\text{H}_3^+ / ^{12}\text{C}^1\text{H}_3^{12}\text{C}^{14}\text{N}$	12.38 ± 0.04	[169]
44	11.4 ± 0.6	$^{12}\text{C}_3^1\text{H}_8^+ / ^{12}\text{C}^1\text{H}_3^{12}\text{C}^1\text{H}_2^{12}\text{C}^1\text{H}_3$	11.27 ± 0.05	[170]

lyze because they show poor signal intensities and pronounced threshold curvatures. However, the assignments are consistent with the corresponding literature values and reveal interesting results. The onset value at 29 *amu* of 10.6 ± 0.6 eV corresponds in fact to the ionization potential of methylenimine $10.55 \pm n.s.$ eV [167]. This would be in line with the work of Diefenbach et. al [66], who postulate besides a heterogeneous also a homogeneous formation route of hydrocyanic acid by dehydrogenation of methylenimine:



The appearance potentials of the interfering ion $^{12}\text{C}_2^1\text{H}_5^+$ which can be formed from $^{12}\text{C}_2^1\text{H}_6$ or $^{12}\text{C}_3^1\text{H}_8$ are with 12.45 ± 0.08 eV [171] and 12.02 ± 0.05 eV [172] respectively significantly higher. Even larger is the difference to the isotopic combination of nitrogen $^{14}\text{N}^{15}\text{N}^+$ which appears at the ionization potential of nitrogen of 15.65 ± 0.1 eV [173]. Figure 5.27 shows the enlarged **IE**-curve at 29 *amu* with arrows indicating the experimental onset value and the literature threshold values of the three interfering species. The onset value at 30 *amu* was expected to be around the ionization potential of $^{12}\text{C}_2^1\text{H}_6$ (11.56 eV [171]) but it was found to be significantly lower (9.9 ± 0.6 eV). This value matches much better the appearance potential of $^{12}\text{C}^{14}\text{N}^1\text{H}_4^+$ from methylamine $^{12}\text{C}^1\text{H}_3^{14}\text{N}^1\text{H}_2$ (cp. Table 5.7), a surprising result

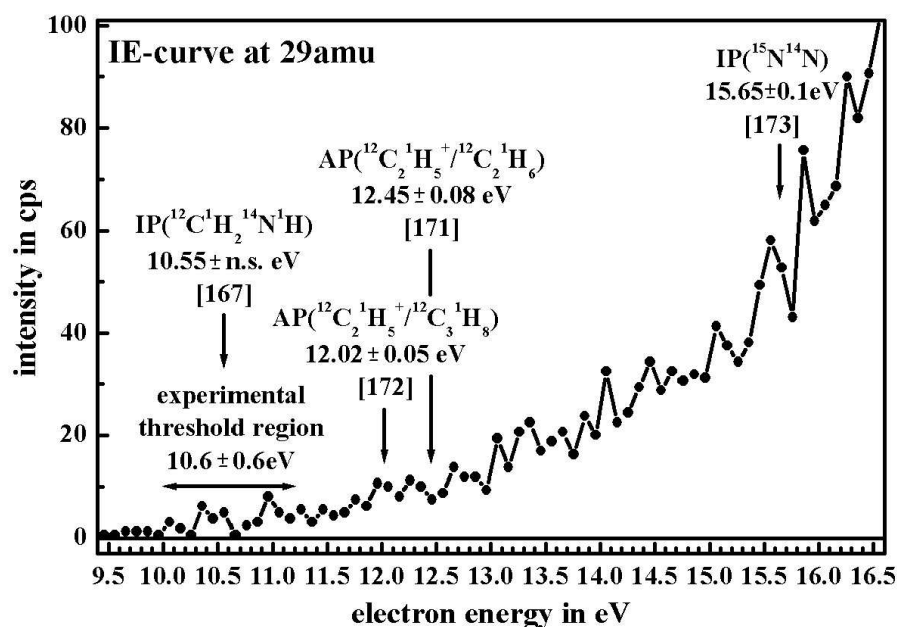
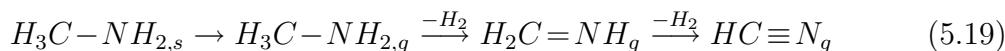


Figure 5.27: BMA-reaction: $\dot{V} = 500 \text{ ml} \cdot \text{min}^{-1}$,
 $x_{\text{NH}_3} = 0.60$,
 $x_{\text{CH}_4} = 0.30$,
 $x_{\text{He}} = 0.10$,
 $T_{\text{reactor}} = 1300 \text{ }^\circ\text{C}$,
 IE-curve at 29 amu

because Figure 5.24 does not show the molecular peak of methylamine at 31 amu. Nevertheless, this can be possible as this peak has only two-thirds of the intensity of that at 30 amu [165]. Indeed, the same measurement at higher sensitivity (q.v. Figure 5.25) shows a small peak at 31 amu. Nevertheless, the signals are altogether too small to assess the presence of methylamine with sufficient reliability. The IE-curve measured at 41 amu confirms the assumption of acetonitrile $^{12}\text{C}^1\text{H}_3^{12}\text{C}^{14}\text{N}$ as the determined threshold value corresponds nicely to its ionization potential. Finally the curve onset at 44 amu can be attributed to the ionization potential of propane $^{12}\text{C}_3^1\text{H}_8$ which is either an impurity in the methane or is formed in the reaction. The peaks at 64 – 70 amu belong than probably to butyronitrile.

5.4.3 Conclusions

In conclusion one can say, that it was also for the BMA-reaction not possible to detect radicals. Even if they were formed, their life time would probably be too short for them to reach the sampling orifice. However, it was possible to identify methylenimine and with some reservation also methylamine by means of their outstanding low appearance potentials. These results lead to the following proposal for the homogeneous formation route of hydrocyanic acid:



The gas phase pyrolysis of methylamine according Equation (5.19) is well known in the literature and can be used for example to prepare methylenimine for threshold ionization experiments [174].

The last chapter of this experimental Part II will be dedicated to a summary of the results obtained for all reactions studied and to a discussion of them with reference to the background Part I.

Chapter 6

Discussion and Assessment of the Method

Goal of the present work was the in-situ investigation of heterogeneously catalyzed reactions with respect to transient gas phase intermediates using molecular beam sampling mass spectrometry supplemented by the determination of ionization and appearance potentials. The main focus was placed on the investigation of the *Pt*-catalyzed hydrocyanic acid formation from methane and ammonia and the setup was designed for this reaction. In addition, the setup was used to study the catalytic combustion of methane, the ammonia oxidation and the ammonia decomposition. These four *Pt*-catalyzed reactions have in common that they are believed to involve transient gas phase species, in many cases radicals. It was in fact possible to identify methylenimine ($CH_2=NH$) as intermediate in the hydrocyanic acid formation, but it was not possible to detect more short-lived species like radicals in any of the investigated reactions, not even in the catalytic combustion of methane although combustion reactions are known to proceed via radical chains. Consequently, the question that has to be discussed thereafter is whether these results can prove the absence of radicals and other very short-lived species in the gas phase or whether our experimental setup was not suited to sample and analyze them.

To answer this question, the in-situ character of the method with respect to heterogeneously formed transient gas phase species has to be assessed. The method could be considered in-situ if it was possible to take a sample, representative for the

reaction zone, and to detect the species of interest in presence of high concentrations of interfering compounds. It could be shown that the mass spectrometric detection supplemented by the threshold ionization technique is an excellent technique to fulfill the latter requirement. Examples therefore were the detection of $^{13}\text{C}^1\text{H}_4^+$ besides $^{16}\text{O}^1\text{H}^+$ in the catalytic combustion of methane (Section 5.1.3) and the detection of $^{13}\text{C}^{14}\text{N}^1\text{H}^+$ besides $^{14}\text{N}^{14}\text{N}^+$ and $^1\text{H}_2^{12}\text{C}^{14}\text{N}^1\text{H}^+$ besides $^{14}\text{N}^{15}\text{N}^+$ in the **BMA**-reaction (Section 5.4.2). A much more serious problem is whether the analyzed sample is really representative for the reaction zone or whether very reactive species like radicals are lost before they reach the ion source of the mass spectrometer. This question will be addressed in the following.

Problem I: External Nozzle

A fundamental problem arises from the use of an external nozzle to probe the gas phase in the tubular reactor as schematically shown in Figure 6.1. At first glance,

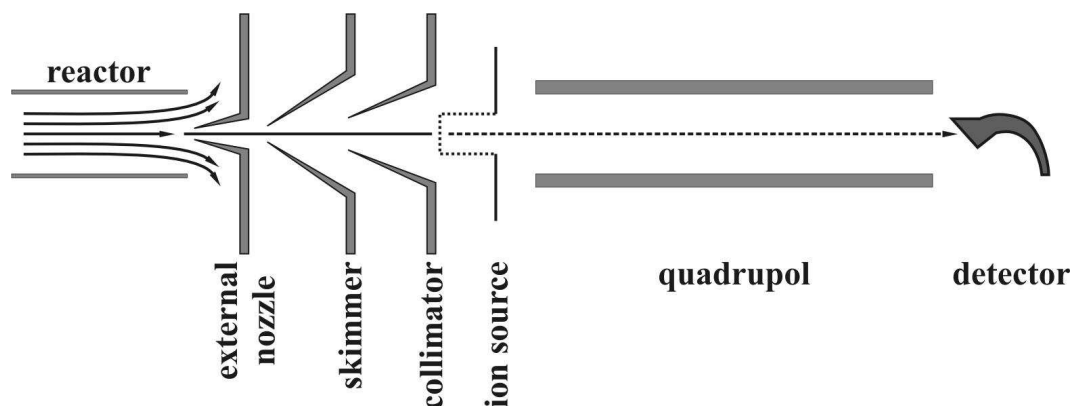


Figure 6.1: *Sampling of the tubular reactor by means of an external nozzle*

the most straightforward solution to get a representative sample seems to be to place the nozzle directly inside the reaction zone. Facing the high temperatures there, this would definitely reduce the in-situ character of the method as the nozzle material itself could serve as a catalyst. It would not be possible to distinguish in this case whether observed species were part of the reaction mechanism inside the tube or were formed on the nozzle surface around the sampling orifice. An efficient cooling is impossible here because the heat dissipation through the thin-walled nozzle cone is limited. The only possibility to avoid a participation of the nozzle material is

to keep its temperature low by allowing for a sufficient distance to the reaction zone. This was realized in our setup where the temperature profile of the heater reaches its maximum about 90 *mm* in front of the nozzle and drops steeply behind (cp. Figure 4.6). However, increasing the distance between reaction zone and place of sampling goes along with a loss of reactive intermediates because of subsequent reactions in the gas phase and collisions with the tube wall. This conflict will be illustrated considering as example the **BMA**-reaction.

As described in Section 5.4, a total flow of 500 *ml · min*⁻¹ has been used to perform the **BMA**-experiments. This flow leads to a temperature profile corresponding roughly to that shown in Figure 4.6 for an argon flow of $\dot{V} = \dot{V}_{ref} = 600 \text{ ml} \cdot \text{min}^{-1}$ ($T_{ref} = 273 \text{ K}$). The temperature at the tube end is under these conditions only about 600 °C and a participation of the nozzle surface can be excluded. The question is rather, whether a transient molecule formed in the zone of maximum temperature ($\sim 85 \text{ mm}$ in front of the nozzle), will survive its transport to the tube end or will be lost in between. An explicit answer to this question can not be given here because it would require a knowledge of the lifetime of the respective molecule under the experimental conditions. However, an impression can be received by calculating roughly how many collisions the molecule suffers before it reaches the nozzle.

Dividing the remaining tube length l (diameter d) according to the measured profile into parts (lengths l_i , mean temperatures T_i) and summing up of the individual residence times τ_i gives an approximate value of the mean residence time τ :

$$\tau = \sum_i \tau_i = \sum_i \frac{V_i}{\dot{V}_i} = \frac{\pi d_r^2 T_{ref}}{4 \dot{V}_{ref}} \sum_i \frac{l_i}{T_i} \approx 50 \text{ ms} \quad (6.1)$$

That is, the transient molecule thought to be formed at the temperature maximum position had to survive about 50 *ms* before it would reach the nozzle. During this time span it will undergo numerous collisions both with other molecules and with the tube wall. The number of binary collisions N_m an individual molecule suffers with other molecules by passing the remaining tube section can be estimated as follows:

$$N_m = \frac{p_0 d_r^2 \sigma T_{ref} N_A}{\dot{V}_{ref}} \sqrt{\frac{\pi}{MR}} \sum_i \frac{l_i}{T_i^{3/2}} \quad (6.2)$$

This equation was derived from the customary formulas of the kinetic theory of gases [175, page 813]. It holds strictly speaking only for a single ideal gas with

molar mass M and collision cross section σ and not for a complex mixture. However, inserting arbitrarily the values for ammonia ($M = 17 \text{ g}\cdot\text{mol}^{-1}$, $\sigma = 0.2\cdot 10^{-18} \text{ m}^2$ [165, page 6-47]) gives at least an idea of the dimension:

$$N_m \sim 10^8 \quad (6.3)$$

The number of collisions N_w a molecule performs with the tube wall depends on the radial dispersion. A heterogeneously formed molecule transported in a flow layer near the tube wall will surely perform more wall collisions than one formed homogeneously in the tube center. Only a statistical value might be obtained by calculating the total number of wall collisions in each volume element V_i and dividing it by the number of molecules contained in V_i . Summing up gives then an approximate value of N_w :

$$N_w = \frac{d_r \cdot T_{ref}}{\dot{V}_{ref}} \cdot \sqrt{\frac{\pi R}{2M}} \sum_i \frac{l_i}{T_i^{1/2}} \sim 10^4 \quad (6.4)$$

The dimensions of N_m and N_w make clear that a highly reactive molecule like a radical will most likely be lost before it reaches the tube end. Even if it survives the collisions in the gas phase where a recombination requires a second radical and an inert collision partner it will be lost in all likelihood by one of the N_w wall collisions. Methylenimine in turn is known to be comparatively stable [167] and was probably for this reason the only intermediate that could be sampled successfully. The conclusion from this discussion is, that an optimal sampling arrangement requires to have the nozzle much closer to the catalytic surface. It will be shown in Part III of this work how this can be reached without violating the in-situ requirement.

Problem II: Interface Construction

Another problem concerns the construction of the molecular beam interface. The intrinsic idea of this interface is to provide a collisionless transfer of the sampled molecules to the ion source of the mass spectrometer. This was not given in our setup as the nozzle chamber could only be pumped by rotary vane pumps. Even with two of them (q.v. Section 4.7), the lowest achievable background pressure p_{nc} was only about 1 *mbar* (cp. Figure 3.1). If one applies Equation 3.21 to calculate

the position of the Mach disk shock x_M one finds it very close behind the nozzle ($d_n = 125 \mu m$):

$$x_M = 0.67 \cdot \sqrt{\frac{p_0}{p_{nc}}} \cdot d_n = 0.67 \cdot \sqrt{\frac{1013 \text{ mbar}}{1 \text{ mbar}}} \cdot 0.125 \text{ mm} = 2.7 \text{ mm} \quad (6.5)$$

The adjacent skimmer cone is located in a fixed position 6 mm behind the nozzle and thus behind the Mach disk shock. From this it follows that all beam molecules have to pass this shock wave, a region of high density, high pressure and high temperature which leads to a loss of their unidirectional motion and possibly to a loss of collision sensitive species. The interface, designed by the manufacturer of the mass spectrometer, fulfills neither the criteria of a ‘Fenn’-type nor those of a ‘Campargue’-type interface (q.v. Section 3.1.2) and needs to be reconstructed.

Conclusion

Notwithstanding the detection method which is excellently suited, the sample finally analyzed in the mass spectrometer can not be considered representative for the chemical composition in the reaction zone. In consequence thereof, the entire method can not be termed in-situ and the non-detectability of transient gas phase species apart from methylenimine must not be interpreted in terms of their absence in the investigated reactions. The only way to check if such species are present or not is to reconstruct the setup under elimination of the problems outlined in the foregoing paragraphs. Even though this requires a much higher experimental effort, it was decided to accept this challenge and a new apparatus is currently under construction. The ideas underlying this new setup will constitute the last part of this work and are at the same time an outlook for the future.

Part III

New Design

Chapter 7

New Design

7.1 Reactor

The core of the new setup is a tubular reactor probed via an internal instead of an external nozzle. Figure 7.1 illustrates the operating principle. Internal nozzle

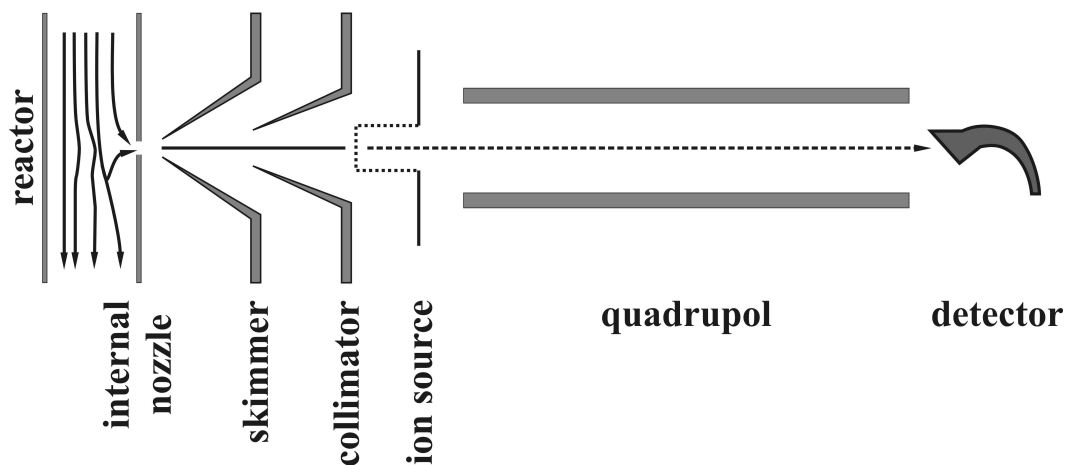


Figure 7.1: *Sampling of the tubular reactor by means of an internal nozzle*

means here nothing else than a tiny hole drilled directly in the tube wall which must be catalytically active. Depending on the wall material the heating can either be achieved directly by using the tube itself as an ohmic resistance or it has to be done indirectly by any other method. The entire reactor is placed in a high vacuum chamber which causes a free jet expansion of the reaction gas mixture through the sampling orifice. A subsequent arrangement of skimmer and collimator extracts the

center of this expansion to form a molecular beam aligned with the quadrupole mass spectrometer. All gas phase species, even those just desorbing from the catalyst surface around the orifice, should get into the pull of this expansion and should be trapped within the molecular beam. No foreign body has to be placed in the reaction zone making it possible to have temperature maximum, reaction zone and nozzle at the same place. This principle conforms to the in-situ idea but is restricted to catalytic wall reactors.

Even though the basic construction is already obvious from Figure 7.1, some modifications are necessary to adapt it to our task. Figure 7.2 shows a three-dimensional cut view of the new reactor as it will be technically realized. The tube arrangement and the nozzle section are shown enlarged in Figure 7.3. The reactor consists of two concentric platinum tubes, each combining three operational elements. Firstly, the tubes serve as catalyst, can secondly be heated by direct current flow and guide thirdly the gas flow into and out of the reaction zone. The entire reactor is designed to be symmetric to the nozzle, leaving its position fixed against thermal expansion.

The operating principle is as follows: As shown in Figure 7.2, feed gas is supplied to the reactor evenly from both sides forming a reaction zone in the annular gap between the inner and the outer tube. A strong direct current, supplied to both tubes by massive electrical contacts, generates a symmetrical temperature profile with its maximum on a level with the nozzle. Consequently, just a flow adjustment is necessary to force any reaction zone to this position. A gold plated heat shield encloses the outer reaction tube and minimizes heat dissipation to the surrounding especially to the sensitive skimmer cone. The concentric tube arrangement offers two catalytic active surfaces in close vicinity to the nozzle, one from the outer tube directly around the hole and the other from the inner tube in close distance line-of-sight to it. This minimizes any sort of collisions and raises hope to detect even very short-lived species. The inner tube serves further as gas outlet as it has a small opening diametrically opposed to the nozzle through which the effluent stream leaves the reactor again symmetrical to the left and to the right. This counter current flow preheats the inlet flow and flattens the temperature profile.

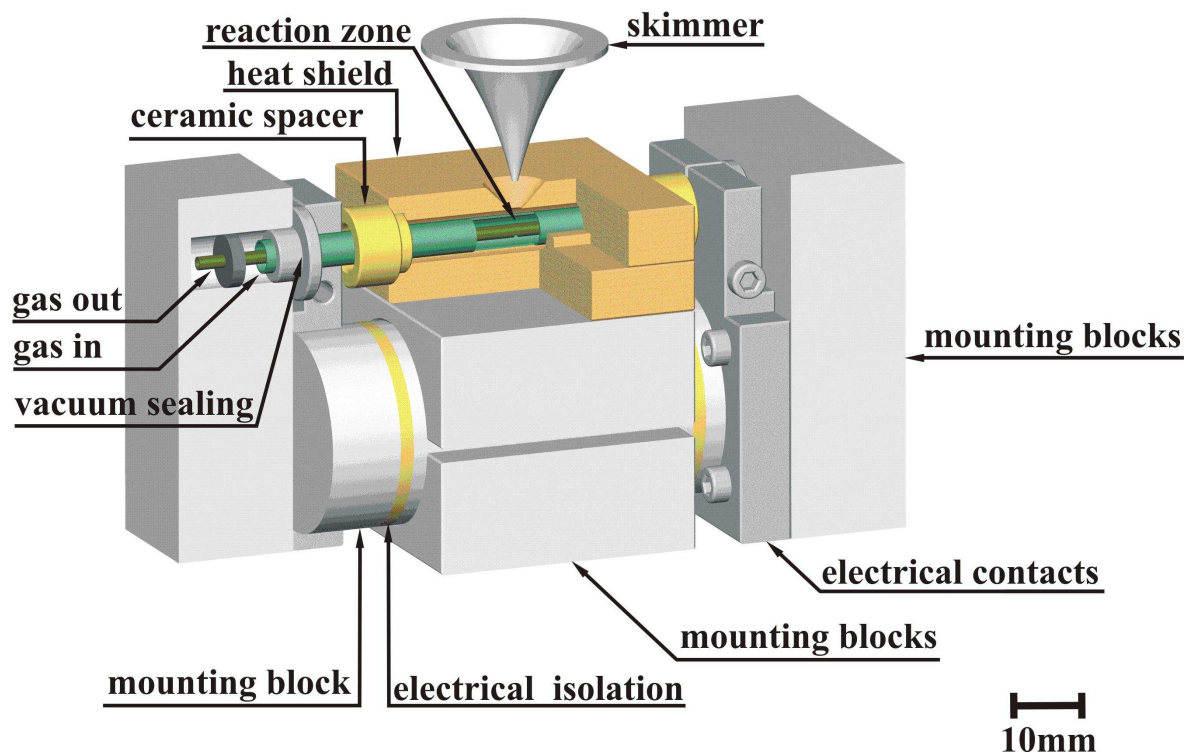


Figure 7.2: New design: reactor - three-dimensional cut view

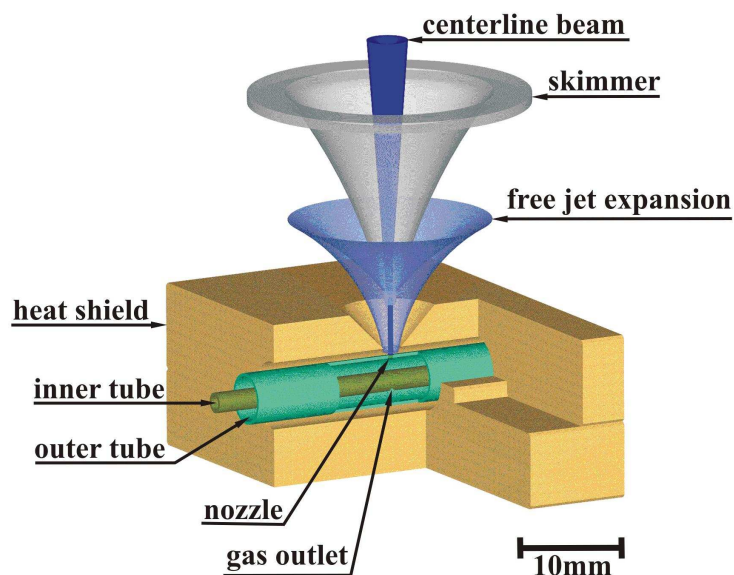


Figure 7.3: New design: reactor - enlarged nozzle section

7.2 Interface and Vacuum System

7.2.1 Interface

Notwithstanding these attractive features, the use of an internal nozzle implicates a challenging technical problem, namely to put the entire reactor operated at atmospheric pressure and high temperatures into a high vacuum surrounding. In consequence of the unfavorable Mach disk location obtained for the old interface (Equation (6.5)), it was decided to operate the new one in the low pressure, that means in the ‘Fenn’-type regime. This offers the advantage to place the skimmer cone in sufficient distance to the hot reactor but still upstream of the Mach disk shock.

The distance between nozzle and skimmer is less critical at low pressure in the nozzle chamber than in the high pressure ‘Campargue’-regime (q.v. Section 3.1.2). Nevertheless, some general criteria have to be considered. For example, a recommendation for a ‘Fenn’-type interface is, to place the skimmer at a distance x_s of the nozzle not larger than one tenth of the hypothetical Mach disk location x_M to avoid too strong intensity losses by background scattering [76]:

$$x_s \leq \frac{1}{10} \cdot x_M \quad (7.1)$$

On the other hand, it is also unfavorable to place the skimmer too close to the nozzle as this would degrade the effect of the first pumping stage. A lower limit is given in the literature to be the point where transition to free molecular flow occurs [67, chapter 2]. The distance between the nozzle and this transition point depends on the stagnation parameters (T_0 , p_0 , gas composition) and the nozzle diameter d_n itself. The stagnation parameters, being here nothing else than the reactor conditions, will vary over a wide range in our experiments making an exact projection difficult. A sort of worst case result can be obtained by calculating the value for room temperature ($T_0 = 298 \text{ K}$). Nitrogen ($M = 28 \text{ g} \cdot \text{mol}^{-1}$) at atmospheric pressure ($p_0 = 1013 \text{ mbar}$) can be used representative for a gas mixture. Concerning the nozzle diameter, the new one should be larger than the old one. This will offer several advantages. Firstly, a larger nozzle diameter leads to a higher beam intensity per steradian resulting in better signal intensities. This will be beneficial for the threshold ionization technique which contends with low ionization cross sections. Secondly it makes the nozzle less

sensitive to blocking and provides thirdly some scope with respect to the required pumpage. As the nozzle discharge depends quadratically from d_n an increase from 125 μm to 150 μm is already substantial.

Performing the calculation for the p_0 , T_0 , M , d_n values set above, the transition from continuum to free molecular flow is obtained to occur about 0.5 cm downstream the nozzle. The calculations were done according to [67, page 48] but are not shown here as they would go beyond the scope of this chapter. Assuming 0.5 cm as a general lower limit, Equation (7.1) leads to the requirement to have the Mach disk shock at least 5 cm downstream the nozzle. Rearrangement of Equation 3.21 gives the maximum pressure in the nozzle chamber that can be allowed to fulfill this condition:

$$p_{nc} \leq p_0 \left(\frac{0.67 \cdot d_n}{x_M} \right)^2 = 1013 \text{mbar} \cdot \left(\frac{0.67 \cdot 0.015 \text{ cm}}{5 \text{ cm}} \right)^2 = 4 \cdot 10^{-3} \text{ mbar} \quad (7.2)$$

7.2.2 Vacuum System

The pumpage S (in $l \cdot s^{-1}$) required to maintain p_{nc} below $4 \cdot 10^{-3} \text{ mbar}$ depends on the nozzle gas discharge Q (in $\text{mbar} \cdot l \cdot s^{-1}$):

$$S = \frac{Q}{p_{nc}} \quad (7.3)$$

Q in turn depends quadratically on nozzle diameter (d_n), the stagnation parameters (T_0 , p_0) and on the discharging gas itself (M , κ) [68, page 84]:

$$Q = \frac{\pi}{4} d_n^2 \cdot p_0 \cdot \left(\frac{2}{\kappa + 1} \right)^{\frac{1}{\kappa - 1}} \cdot \sqrt{\frac{2\kappa}{\kappa + 1} \cdot \frac{RT_0}{M}} \quad (7.4)$$

Again, a reasonable value providing a profound basis for a pump selection, can be obtained by performing the calculation for nitrogen ($\kappa = 1.4$) at room temperature and atmospheric pressure. The results for Q and S are shown in Equation 7.5 :

$$Q = 3.7 \frac{\text{mbar} \cdot l}{s} \quad \rightarrow \quad S = \frac{3.7}{4 \cdot 10^{-3}} \frac{\text{mbar} \cdot l}{s \cdot \text{mbar}} = 925 \frac{l}{s} \quad (7.5)$$

The latter value is very important as it illustrates that considerable pumpage is required to maintain a sufficiently low background pressure. In contrast to common molecular beam setups which use large diffusion pumps to operate their nozzle chambers, this must be avoided here as such a vacuum contains always traces of the

pumping oil. As one task of our new setup is to look for hydrocarbon intermediates, dryly working pumps are the only alternative. It was decided to use a large turbomolecular pump with a pumpage higher than $1000 \text{ l} \cdot \text{s}^{-1}$. Figure 7.4 gives an impression how the new setup will look like.

The dimensions of the new machine are provided by the vacuum requirements. It will be considerable larger than the old one. In favor of the center of gravity, it will be operated in vertical position. The reactor is mounted on a x,y,z -adjustable platform (not shown in Figure 7.4) to allow for a precise positioning with respect to the fixed skimmer cone. However, as calculated in Section 7.2.1 high signal intensities will allow only a small distance between nozzle and skimmer (heat shield required). The skimmer itself is fixed on a platform and this construction separates nozzle and skimmer chamber. The collimator cone builds the tip of a cylindrical chamber which is connected to the collimator chamber and contains the mass spectrometer (cp. Figure 4.1). Movable bellows between skimmer- and **MS** chamber allow varying the distance between skimmer and collimator to adapt the pressure to mass spectrometric conditions. Both chambers are separately pumped by turbomolecular pumps.

7.3 Applications and Outlook

The new setup was designed to be as flexible as possible. In principle, any reactor that can be probed via internal nozzle could be installed in the nozzle chamber. The reactor described in Section 7.1 is solely chosen to have a simple system to study platinum catalyzed reactions like the catalytic combustion of methane or the ammonia oxidation. It will not allow for studying reactions involving hydrogen (ammonia decomposition, **BMA**-reaction) as it would diffuse out of the platinum tubes overloading the turbo pumps. Such reactions would need to have the catalyst on a gas tight support which can be heated by an indirect method. In any case, the principle remains the same and even such more demanding reactors may be operated in our new setup. Depending on the success of the mass spectrometric experiments, it could also be tried to perform other spectroscopic methods on the molecular beam. The traverse path of the bellows is sufficient to move the **MS** chamber out of the skimmer chamber. The latter is equipped with suitable ports providing two optical axes perpendicular to each other and to the molecular beam. Such a cross-beam arrangement could be used for example to perform laser induced fluorescence spectroscopy.

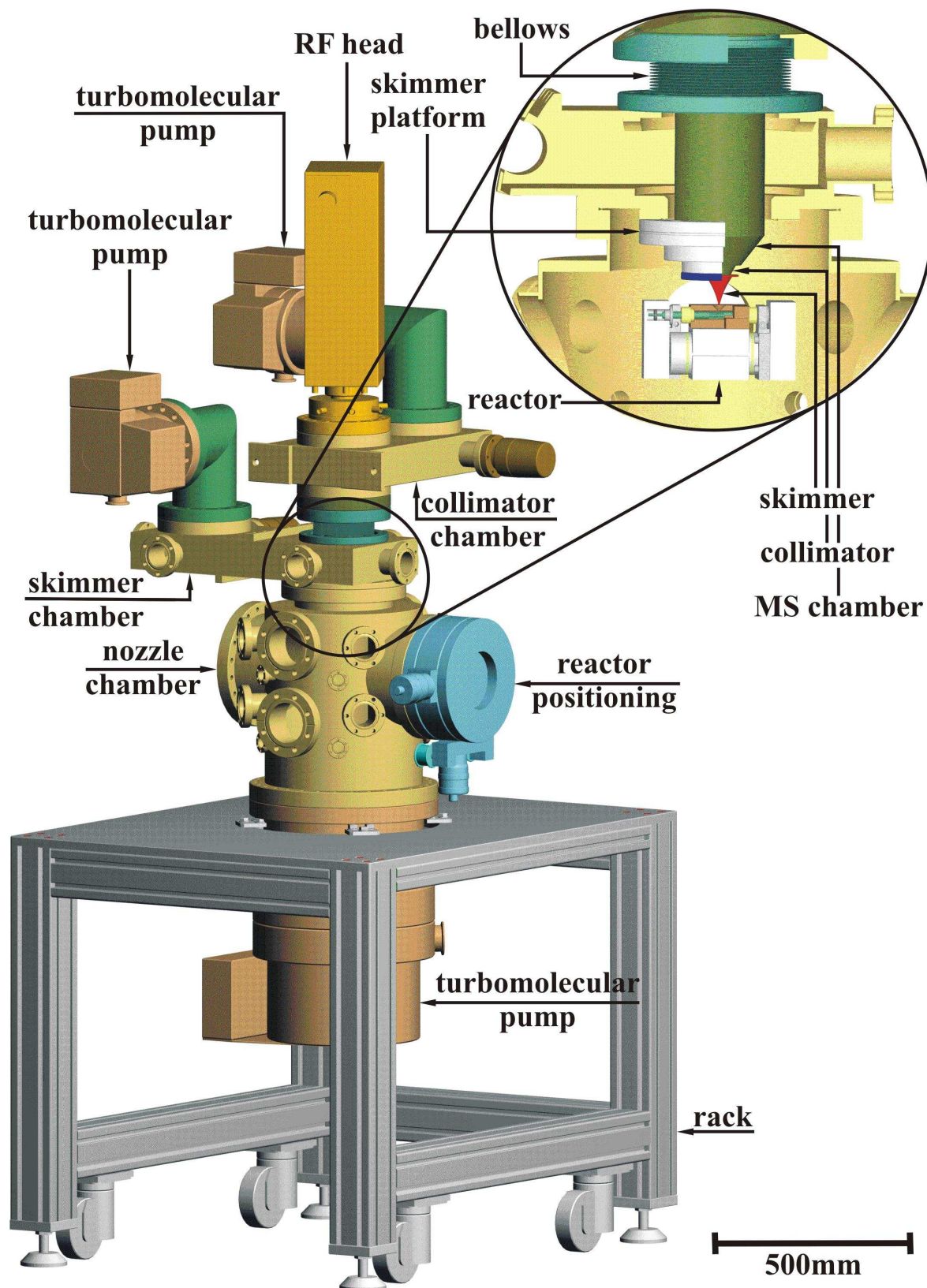


Figure 7.4: New design: core features - vacuum system and interface

Chapter 8

Summary

Heterogeneous catalysis is characterized by complex chemical and physical interactions between the surface and the bulk of the catalyst and the surrounding gas phase. The present work is aimed at the in-situ investigation of the gas phase above a working catalyst with respect to transient intermediates. If such species were detected, it would be an indication of reaction steps proceeding homogeneously in the gas phase.

The reaction of interest was the *Pt*-catalyzed formation of hydrocyanic acid from methane and ammonia. To study this reaction under technical operation conditions, a bench-scale model reactor, simulating a single tube of the technical tube bundle reactor, was connected via a molecular beam sampling interface to a quadrupole mass spectrometer. This particular instrument allowed to identify the beam constituents both by means of their mass numbers and their ionization- and appearance potentials respectively. The reactor consisted of an electrically heated ceramic tube, covered on the inside with platinum, and could be operated at atmospheric pressure, temperatures up to 1300 °C and gas flows up to 4000 ml · min⁻¹. Molecular beam sampling has been applied to quench short-lived species arising in the reaction zone and to provide their collisionless transport to the ion source of the mass spectrometer. As radicals are an important group of gas phase intermediates in heterogeneous catalysis, the determination of ionization and appearance potentials (threshold ionization technique) was necessary to distinguish their molecular ions from fragments of interfering molecules appearing at the same nominal mass in the mass spectrum. To gain experience with the new method, the experimental setup has been used to investigate in addition to the hydrocyanic acid formation further *Pt*-catalyzed reactions. The

catalytic combustion of methane, the ammonia oxidation and the ammonia decomposition were selected because they are also thought to involve different gas phase intermediates.

The investigations were started with determination of the uncertainty connected with the ionization- and appearance potential measurements. As the experimental error is largely determined by the energy spread of the ionizing electrons, a simple theoretical model, containing this spread as parameter, was fitted to the ionization efficiency curve of helium. The He^+ -ion was chosen here as it has no low-lying excited electronic states making the curvature at the onset of its ionization efficiency curve exclusively determined by the energy distribution of the ionizing electrons. This distribution was found to be of Gaussian-type with a standard deviation of $\sigma = 0.28 \text{ eV}$. Taking the experimental error as $2 \cdot \sigma \approx 0.6 \text{ eV}$, the threshold ionization technique allowed to discriminate between interfering ions which are separated in their ionization- or appearance potentials by at least 0.6 eV . This requirement was fulfilled by all of the expected intermediates.

The first reaction studied was the catalytic combustion of methane as combustion reactions are known to proceed via radical chains. Contrary to the expectations, neither a radical nor any other reaction intermediate could be detected. Only CO_2 and H_2O have been observed. However, this result could not prove the absence of intermediate species as a temperature programmed experiment suggested that complete conversion has already been achieved considerably upstream of the sampling orifice. This was concluded because a thermocouple, fixed outside the tube at position of maximum temperature of the external heater, registered a jump in temperature when the reaction ignited but it registered no temperature change at the much higher conversion jump caused by the parametric sensitivity of the tubular reactor to highly exothermic reactions. Consequently, it seems that the reaction ignites at a position predetermined by the external heater but shifts then axially towards the reactor inlet like a burner flame, which, even when ignited in some distance to the burner tube, moves rapidly to its upper end. In this case, the failure to detect radicals could be understood. If radicals were at all present in the reaction zone, they would have hardly survived their transport to the tube end where the reaction mixture was sampled. Even measurements performed at high gas flow failed to detect intermediates as it was apparently not possible to shift the reaction zone in front of the sampling orifice.

The reaction was not self-sustaining and the catalyst temperature near the orifice was in all likelihood below the experimentally determined ignition temperature of $358\text{ }^{\circ}\text{C}$.

The second reaction studied was again an exothermic one, namely the platinum catalyzed ammonia oxidation. Also the investigations on this reaction were started performing a temperature programmed experiment. Similar to the methane combustion, the ammonia oxidation showed an ignition point ($\sim 220\text{ }^{\circ}\text{C}$), that was followed some degree Centigrade higher by a sudden complete conversion of the understoichiometric component in consequence of the sensitivity of the nonisothermal reactor to small temperature changes. In contrast to the methane combustion, the ammonia oxidation ran autothermically in the reactor. Utilizing this self-sustaining behavior, the reaction zone could be shifted close to the sampling orifice just by increasing the gas flow. Consequently, the reaction was screened across a wide range of temperatures, flows and compositions but none of the intermediates proposed in the literature was detected. Only the common oxidation products NO , N_2O , N_2 and H_2O have been found in varying amounts. As the reaction zone could be probed properly for the ammonia oxidation, this result was interpreted with respect to the reaction mechanism. Although transient gas phase species can not be definitely excluded, their concentration must at least be very low. In other words, it seems likely that the ammonia oxidation proceeds so fast that any intermediate formed on the catalyst surface reacts further before it can desorb in the gas phase.

One step towards the hydrocyanic acid formation was done by performing as third test reaction the endothermic ammonia decomposition into the elements. This reaction is likewise platinum catalyzed and reported in the literature to involve gas phase radicals formed from ammonia by successive loss of hydrogen atoms on the platinum surface. However, the measurements leading to these results were performed at low pressures up to 1 mbar . Indeed, radicals could not be detected in our experiments which were performed under atmospheric pressure. All measured threshold values could be attributed to the appearance potentials of the corresponding ions from ammonia or nitrogen. Nevertheless, there was again the question about the interpretation of these findings. For endothermic reactions, the reaction zone was given by the temperature profile of the external heater. Taking this into account, calculations on the number of collisions between the gas molecules themselves and

the tube wall casted doubts on the possibility that radicals formed in the reaction zone could reach the sampling orifice. Consequently, the sample taken at the tube end could not be considered to be representative for the reaction zone, making it impossible to conclude about the radical concentration there.

The same arguments held of course for the hydrocyanic acid formation. Also for this reaction, none of the determined threshold values corresponded to the ionization potential of one of the expected radicals. An important result was, that the threshold value measured at $m/z = 29$ *amu* agrees with the ionization potential of methylenimine ($CH_2=NH$) which is lower than those of any of the interfering ions. The experimental proof of this intermediate is hence of importance, as it supports a theoretical work published in the literature which predicts the dehydrogenation of methylenimine to hydrocyanic acid as a homogeneous key step in the reaction mechanism. In contrast to radicals, methylenimine is known to be comparatively stable and could therefore be sampled even some centimeters behind the reaction zone.

This result shows that the method is basically suited to detect transient gas phase intermediates in heterogeneously catalyzed reactions and can be used to develop or improve microkinetic models involving homogeneous reaction steps. However, a careful investigation of the experimental setup showed that the entire method could not be considered as in-situ with respect to real short-lived species like radicals. The mass spectrometric detection itself was excellently suited, but the sampling process would be hardly survived by a radical or any other highly reactive molecule. It was found that the problem to obtain a representative sample out of the reaction zone could be solved by drilling the sampling orifice directly in the catalytically active tube wall. This method's disadvantage is that the molecular beam sampling requires placing the entire reactor into a high vacuum surrounding. As the latter requirement is only a technical but not any longer a fundamental problem, the sampling system was redesigned and a new machine is presently under construction.

Bibliography

- [1] Büchel K. H.; Moretto H. H.; Woditsch P. *Industrielle Anorganische Chemie*. Wiley-VCH, Weinheim, 3rd edition, 1999.
- [2] Jennings J. R. *Catalytic Ammonia Synthesis: Fundamentals and Practice*. Plenum Press, New York, 1991.
- [3] Ertl G.; Knözinger H.; Weitkamp J.; Eds. *Handbook of Heterogeneous Catalysis*, volume 4, chapter 2 - Inorganic Reactions. Wiley-VCH, Weinheim, 1997.
- [4] Ertl G.; Knözinger H.; Weitkamp J.; Eds. *Handbook of Heterogeneous Catalysis*, volume 5, chapter 4 - Organic Reactions. Wiley-VCH, Weinheim, 1997.
- [5] Ertl G.; Knözinger H.; Weitkamp J.; Eds. *Handbook of Heterogeneous Catalysis*, volume 4, chapter 3 - Energy Related Catalysis. Wiley-VCH, Weinheim, 1997.
- [6] Ertl G.; Knözinger H.; Weitkamp J.; Eds. *Handbook of Heterogeneous Catalysis*, volume 4, chapter 1 - Environmental Catalysis. Wiley-VCH, Weinheim, 1997.
- [7] Sinfelt J. H. Role of Surface Science in Catalysis. *Surf. Sci.* **2002**, *500* (1-3), 923-946.
- [8] Hoffmann F. M.; Dwyer D. J. *The Promise of Surface Science in Catalysis - Success or Failure?* ACS Symposium Series **1992**, *482*, 1-22, Amer. Chemical Soc., Washington.
- [9] Haw J. F. *In-Situ Spectroscopy in Heterogeneous Catalysis*. Wiley-VCH, Weinheim, 2002.
- [10] Gleaves J. T.; Ebner J. R.; Kuechler T. C. Temporal Analysis of Products (TAP) - A Unique Catalyst Evaluation System with Submillisecond Time Resolution. *Catal. Rev.-Sci. Eng.* **1988**, *30* (1), 49-116.

- [11] Anderson B. G.; van Santen R. A.; van Ijzendoorn L. J. Positron Emission Imaging in Catalysis. *Appl. Catal. A-Gen.* **1997**, *160*, 125-138.
- [12] Clausen B. S.; Topsøe H.; Frahm R. Application of Combined X-Ray Diffraction and Absorption Techniques for In Situ Catalyst Characterization. *Adv. Catal.* **1998**, *42*, 315-344.
- [13] Clausen B. S.; Steffensen G.; Fabius B.; et al. In Situ Cell for Combined XRD and On-line Catalysis Tests: Studies of Cu-based Water Gas Shift and Methanol Catalysts. *J. Catal.* **1991**, *132*, 524-535.
- [14] Bazin D.; Guzzi L. Soft X-Ray Absorption Spectroscopy in Heterogeneous Catalysis. *Appl. Catal.* **2001**, *213*, 147-162.
- [15] Niemantsverdriet J. W. *Spectroscopy in Catalysis*, chapter 5 - Mössbauer Spectroscopy, pages 113-135. Wiley-VCH, Weinheim, 2nd edition, 2000.
- [16] Ryczkowski J. IR Spectroscopy in Catalysis. *Catal. Today* **2001**, *68*, 263-381.
- [17] Hunger M.; Weitkamp J. In situ IR, NMR, EPR and UV/Vis Spectroscopy: Tools for New Insight into the Mechanisms of Heterogeneous Catalysis. *Angew. Chem. Int. Edit.* **2001**, *40*, 2954-2971.
- [18] Wachs I. E. In Situ Raman Spectroscopy Studies of Catalysts. *Top. Catal.* **1999**, *8*, 57-63.
- [19] Somorjai G. A.; Rupprechter G. Molecular Studies of Catalytic Reactions on Crystal Surfaces at High Pressures and High Temperatures by Infrared-Visible Sum Frequency Generation (SFG) Surface Vibrational Spectroscopy. *J. Phys. Chem. B* **1999**, *103*, 1623-1638.
- [20] Cavani F.; Trifirò F. Selective Oxidation of Light Alkanes: Interaction Between the Catalyst and the Gas Phase on Different Classes of Catalytic Materials. *Catal. Today* **1999**, *51* (4), 561-580.
- [21] Lunsford J. H. The Catalytic Oxidative Coupling of Methane. *Angew. Chem. Int. Edit. Engl.* **1995**, *34*, 970-980.

- [22] Martir W.; Lunsford J. H. The Formation of Gas-Phase π -Allyl Radicals from Propylene over Bismuth Oxide and γ -Bismuth Molybdate Catalysts. *J. Am. Chem. Soc.* **1981**, *103*, 3728-3732.
- [23] Burch R.; Crabb E. M. Homogeneous and Heterogeneous Contributions to the Oxidative Dehydrogenation of Propane on Oxide Catalysts. *Appl. Catal. A* **1993**, *100* (1), 111-130.
- [24] Kim Y-C.; Ueda W.; Moro-oka Y. Selective Oxidation of Propane Involving Homogeneous and Heterogeneous Steps over Multicomponent Metal Oxide Catalysts. *Appl. Catal.* **1991**, *1*, 175-187.
- [25] Davis M. B.; Pawson M. D.; Veser G.; et al. Methane Oxidation Over Noble Metal Gauzes: An LIF Study. *Combust. Flame* **2000**, *123* (1-2), 159-174.
- [26] Rosen A.; Ljunström S.; Wahnström T.; Kasemo B. Laser Diagnostics of Radicals in Catalytic Reactions. *J. Electron Spectrosc.* **1986**, *39*, 15-25.
- [27] Selwyn G. S.; Lin M. C. Free Radical Formation in the Catalytic Oxidation of NH_3 over a Polycrystalline *Pt* Surface at High Temperatures. *Langmuir* **1985**, *1* (2), 212-219.
- [28] Melton C. E.; Emmett P. H. Transient Species Observed in the Catalyzed Decomposition of Ammonia. *J. Phys. Chem.* **1964**, *68* (11), 3318-3324.
- [29] Melton C. E. Studies of Transient Species Formed During Catalytic Reactions of CO_2 and D_2 and 1-Butene. *J. Phys. Chem.* **1961**, *35* (5), 1751-1757.
- [30] Driscoll D. J.; Campbell K. D.; Lunsford J. H. Surface-Generated Gas-Phase Radicals: Formation, Detection, and Role in Catalysis. *Adv. Catal.* **1987**, *35*, 139-186.
- [31] Wolfrum J. Advanced Laser Spectroscopy in Combustion Chemistry: From Elementary Steps to Practical Devices. *Faraday Discuss.* **2001**, *119*, 1-26.
- [32] Crosley D. R. Laser-Induced Fluorescence in Spectroscopy, Dynamics, and Diagnostics. *J. Chem. Educ.* **1982**, *59* (6), 446-455.

- [33] Lunsford J. H. The Role of Surface-Generated Gas-Phase Radicals in Catalysis. *Langmuir* **1989**, *5*, 12-16.
- [34] Sablier M.; Fujii T. Mass Spectrometry of Free Radicals. *Chem. Rev.* **2002**, *9*, 2855-2924.
- [35] Wayner D. D. M.; Griller D. *Advances in Free Radical Chemistry* (Ed.: Tanner D.), chapter 4 - Free Radical Thermochemistry, pages 159–192. JAI Press, Irvine, 1990.
- [36] Donnelly V. M. Mass Spectrometric Measurements of Neutral Reactant and Product Densities During *Si* Etching in a High-Density Helical Resonator Cl_2 Plasma. *J. Appl. Phys.* **1996**, *79* (12), 9353-9360.
- [37] Foner S. N.; Hudson R. L. The Detection of Atoms and Free Radicals in Flames by Mass Spectrometric Techniques. *J. Chem. Phys.* **1953**, *21* (8), 1374-1382.
- [38] Slagle I. R.; Gutman D. Kinetics of Polyatomic Free Radicals Produced by Laser Photolysis. 5. Study of the Equilibrium $CH_3 + O_2 \rightleftharpoons CH_3O_2$ between 421 and 538 °C. *J. Am. Chem. Soc.* **1985**, *107*, 5342-5347.
- [39] Rosenstock H. M. The Measurement of Ionization and Appearance Potentials. *Int. J. Mass Spectrom.* **1976**, *20*, 139-190.
- [40] Clarke E. M. Ionization Probability Curves Using an Electron Selector. *Can. J. Phys.* **1954**, *32*, 764-774.
- [41] Brion C. E.; Thomas G. E. A Versatile 'Monoenergetic' Electron Impact Spectrometer for the Study of Inelastic Collision Processes. *Int. J. Mass Spectrom.* **1968**, *1*, 25-39.
- [42] Harrison A. G. *Mass Spectrometry of Organic Ions* (Ed.: McLafferty F. W.), chapter 5 - Mass Spectrometry of Organic Radicals, pages 207–253. Academic Press, New York, 1st edition, 1963.
- [43] Schmidt L. D.; Huff M.; Bharadwaj S. S. Catalytic Partial Oxidation Reactions and Reactors. *Chem. Eng. Sci.* **1994**, *49* (24A), 3981-3994.

- [44] Huff M. C.; Androulakis I. P.; Sinfelt J. H.; et al. The Contribution of Gas-Phase Reactions in the *Pt*-Catalyzed Conversion of Ethane-Oxygen Mixtures. *J. Catal.* **2000**, *191*, 46-54.
- [45] Nelson P. F.; Lukey C. A. Isotopic Evidence for Direct Methyl Coupling and Ethane to Ethylene Conversion during Partial Oxidation of Methane over Li/MgO. *J. Phys. Chem.* **1988**, *92* (22), 6176-6179.
- [46] Cavani F.; Trifirò F. The Oxidative Dehydrogenation of Ethane and Propane as an Alternative Way for the Production of Light Olefins. *Catal. Today* **1995**, *24*, 307-313.
- [47] Mims C. A.; Mauti R. Radical Chemistry in Methane Oxidative Coupling: Tracing of Ethylene Secondary Reactions with Computer Models and Isotopes. *J. Chem. Phys.* **1994**, *98* (50), 13357-13372.
- [48] Moro-oka Y.; Ueda W. Multicomponent Bismuth Molybdate Catalyst: A Highly Functionalized Catalyst System for the Selective Oxidation of Olefin. *Adv. Catal.* **1995**, *40*, 233-273.
- [49] Senkan S.; Castaldi M. *Ullmann's Encyclopedia of Industrial Chemistry*, chapter - Combustion, page <http://www.mrw.interscience.wiley.com/ueic/index.html> (accessed June 2003). Wiley-VCH, Weinheim, 2003.
- [50] Prasad R.; Kennedy L. A.; Ruckenstein E. Catalytic Combustion. *Catal. Rev.-Sci. Eng.* **1984**, *26* (1), 1-58.
- [51] Lewis G.; von Elbe G. *Combustion, Flames and Explosions of Gases*, chapter 4 - The Reaction between Hydrocarbons and Oxygen, pages 96-211. Academic Press, New York, 3rd edition, 1987.
- [52] Lissianski V. V.; Zamansky V. M.; Gardiner W. C. *Gas-Phase Combustion Chemistry* (Ed.: Gardiner W. C.), chapter 1.3 - Hydrocarbon Combustion Chemistry, pages 31-41. Springer, New York, 1st edition, 2000.
- [53] Scherer J. J.; Aniolek K. W.; Cernansky N. P.; et al. Determination of Methyl Radical Concentrations in Methane/Air Flame by Infrared Cavity Ringdown Laser Absorption Spectroscopy. *J. Chem. Phys.* **1997**, *107* (16), 6196-6203.

- [54] Holzmann H. Über die Katalytische Oxidation von Ammoniak bei der Industriellen Salpetersäure-Herstellung. *Chem.-Ing.-Tech.* **1967**, *39* (2), 89-95.
- [55] Andrussow L. Über die Katalytische Ammoniakoxidation. *Z. angew. Chem.* **1926**, *39*, 321-332.
- [56] Andrussow L. Über die Katalytische Oxydation von Ammoniak-Methan-Gemischen zu Blausäure. *Angew. Chem.* **1935**, *48* (37), 593-595.
- [57] Raschig F. Über die Ammoniakverbrennung. *Z. angew. Chem.* **1927**, *40* (37), 1183-1185.
- [58] Hofmann K. A.; Korpiun J. Über die Bildung von Hydrazin beim Oxydativen Abbau von Ammoniak und beim Aufbau in der Flamme. *Ber. Dtsch. Chem. Ges.* **1929**, *62*, 3000-3008.
- [59] Zawadzki J. The Mechanism of Ammonia Oxidation and Certain Analogous Reactions. *Discuss. Faraday Soc.* **1950**, *8*, 140-152.
- [60] Bodenstein M. Über den Mechanismus der Katalytischen Ammoniakverbrennung. *Z. Elektrochem.* **1935**, *41* (7b), 466-468.
- [61] Wendlandt R. Neuere Erfahrungen über die Katalytische Ammoniakverbrennung. *Z. Elektrochem.* **1949**, *53* (5), 307-319.
- [62] Foner Y. M.; Nadykto B. T.; Rybalko V. F.; et al. Use of Secondary Ion Emission to Study the Catalytic Oxidation of Ammonia on Platinum. *Kinetika i Kataliz* **1964**, *5* (3), 496-504.
- [63] Endter F. Die Technische Synthese von Cyanwasserstoff aus Methan und Ammoniak ohne Zusatz von Sauerstoff. *Chem.-Ing.-Tech.* **1958**, *30* (5), 305-310.
- [64] Gail E.; Gos S.; Kulzer R.; et al. *Ullmann's Encyclopedia of Industrial Chemistry*, chapter - Cyano Compounds, Inorganic, page <http://www.mrw.interscience.wiley.com/ueic/index.html> (accessed June 2003). Wiley-VCH, Weinheim, 2003.
- [65] Pfeil E.; Hoffmann P. Über die Synthese von Blausäure aus Methan und Ammoniak. *Ber. Bunsen-Ges. Phys. Chem.* **1963**, *67* (2), 229-235.

- [66] Diefenbach M.; Brönstrup M.; Aschi M.; et al. HCN Synthesis from Methane and Ammonia: Mechanisms of Pt^+ - Mediated C-N Coupling. *J. Am. Chem. Soc.* **1999**, *121* (45), 10614-10625.
- [67] Scoles G. chapter 1; Miller D. R. chapter 2; Pauly H. chapter 4. *Atomic and Molecular Beam Methods - Volume 1* (Ed.: Scoles G.), chapter 1 - Introduction; 2 - Free Jet Sources; 4 - Other Low Energy Beam Sources. Oxford University Press, Oxford, 1st edition, 1988.
- [68] Wutz M.; Adam H.; Walcher W.; Jouston K. *Handbuch Vakuumtechnik*, chapter 2 - Gasgesetze, Grundlagen der kinetischen Gastheorie und Gasdynamik, 4 - Strömungsvorgänge. Vieweg, Braunschweig, 7th edition, 2000.
- [69] Lide D. R. *CRC Handbook of Chemistry and Physics*. CRC Press, Boca Raton, 84th edition, 2003.
- [70] Kantrowitz A.; Grey J. A High Intensity Source for the Molecular Beam. Part I. Theoretical. *Rev. Sci. Instrum.* **1951**, *22* (5), 328-332.
- [71] Kistiakowsky G. B.; Slichter W. P. A High Intensity Source for the Molecular Beam. Part II. Experimental. *Rev. Sci. Instrum.* **1951**, *22* (5), 333-337.
- [72] Streeter V. L. *Fluid Dynamics* (Ed.: Hunsaker J. C.), chapter 2 - Fundamentals of Frictionless Fluid Flow. McGraw-Hill Publications in Aeronautical Science. McGraw-Hill Book Company, New York, 1st edition, 1948.
- [73] Courant R.; Friedrichs K. O. *Supersonic Flow and Shock Waves* (Ed.: Bohr H.; Courant R.; Stoker J. J.), chapter 1A - General Equations of Flow. Thermodynamic Notions. Pure and Applied Mathematics. Interscience Publishers, New York, 1st edition, 1948.
- [74] Rebrov A. K. Free Jets in Vacuum Technologies. *J. Vac. Sci. Technol. A* **2001**, *19* (4), 1679-1687.
- [75] Bier K. Zur Wirkung von Verdichtungsstößen im Übergangsbereich zwischen Gasdynamischer und Molekularer Strömungsform. *Fortschr. Physik* **1963**, *11*, 325-356.

- [76] Campargue R. Progress in Overexpanded Supersonic Jets and Skimmed Molecular Beams in Free-Jet Zones of Silence. *J. Phys. Chem.* **1984**, *88*, 4466-4474.
- [77] Beijerinck H. C. W.; van Gerwen R. J. F.; Kerstel E. R. T.; et al. Campargue-Type Supersonic Beam Sources: Absolute Intensities, Skimmer Transmission and Scaling Laws for Mono-Atomic Gases He, Ne and Ar. *Chem. Phys.* **1985**, *96*, 153-173.
- [78] Dun H.; Mattes B. L.; Stevenson D. A. The Gas Dynamics of a Conical Nozzle Molecular Beam Sampling System. *Chem. Phys.* **1979**, *38*, 161-172.
- [79] Fenn J. B. Mass Spectrometric Implications of High-Pressure Ion Sources. *Int. J. Mass Spectrom.* **2000**, *200*, 459-478.
- [80] Brown G. R. and Pertel R. A Fast Flow Reactor Sampled by a TOF Mass Spectrometer with a Molecular Beam Inlet System. *Int. J. Mass Spectrom.* **1975**, *16*, 53-67.
- [81] Fristrom R. M. Flame Sampling for Mass Spectrometry. *Int. J. Mass Spectrom.* **1975**, *16*, 15-32.
- [82] Gersh M. E.; Silver J. A.; Zahniser M. S.; et al. Versatile High Temperature Flow Reactor for Kinetic and Spectroscopic Studies. *Rev. Sci. Instrum.* **1981**, *52* (8), 1213-1222.
- [83] Jayaraman R.; McGrath R. T.; Hebner G. A. Ion and Neutral Species in C_2F_6 and CHF_3 Dielectric Etch Discharges. *J. Vac. Sci. Technol. A* **1999**, *17* (4), 1545-1551.
- [84] Tsutsumi Y.; Ikegawa M.; Usui T.; et al. Molecular Beam Sampling to Analyze the Reaction Mechanism of Chemical Vapor Deposition. *J. Vac. Sci. Technol. A* **1996**, *14* (4), 2337-2342.
- [85] Wyatt J. R.; DeCorpo J. J.; McDowell M. V.; et al. Simple Method for Adiabatically Sampling Reactive Gaseous Systems for Mass Spectrometric Analysis. *Rev. Sci. Instrum.* **1974**, *45* (7), 916-919.
- [86] Fite W. L. Detection of Radicals and Excited Molecules in Dynamic Systems. *Int. J. Mass Spectrom.* **1975**, *16*, 109-124.

- [87] Pertel R. Molecular Beam Sampling of Dynamic Systems. *Int. J. Mass Spectrom.* **1975**, *16*, 39-52.
- [88] Wyatt J. R.; Decorpo J. J.; McDowell M. V.; et al. Sampling of Flow Systems at Atmospheric Pressure. *Int. J. Mass Spectrom.* **1975**, *16*, 33-38.
- [89] Slagle I. R.; Yamada F.; Gutman D. Kinetics of Free Radicals Produced by Infrared Multiphoton-Induced Decompositions. 1. Reactions of Allyl Radicals with Nitrogen Dioxide and Bromine. *J. Am. Chem. Soc.* **1981**, *103* (1), 149-153.
- [90] Vestal M. L. Methods of Ion Generation. *Chem. Rev.* **2001**, *101* (2), 361-375.
- [91] Hiden Analytical Ltd. Ion Source of the HAL4 EPIC Low Energy - Constructional Drawing. personal communication, **2002**.
- [92] Hiden Analytical Ltd. *EPIC and IDP Analysers; Operator's Manual*. Document Number: HA-085-013, Warrington England, **1998**.
- [93] von Ardenne M. *Tabellen zur Angewandten Physik - Band I* (Ed.: von Ardenne M.), chapter 3 - Erzeugung von Elektronen. VEB Deutscher Verlag der Wissenschaften, Berlin, 4th edition, 1979.
- [94] Fan H. Y. Thermionic Emission from Sintered Cathode of Thoria and Tungsten Mixture. *J. Appl. Phys.* **1949**, *20* (2), 682-690.
- [95] Campana J. E. Elementary Theory of the Quadrupol Mass Filter. *Int. J. Mass Spectrom.* **1980**, *33*, 101-117.
- [96] Dawson P. H. *Quadrupol Mass Spectrometry and its Applications* (Ed.: Dawson P. H.), chapter 2 - Principles of Operation; 3 - Analytical Theory. Elsevier Scientific Publishing Company, Amsterdam, 1st edition, 1976.
- [97] Brunnè C.; Voshage H. *Massenspektrometrie*, chapter 5 - Ionennachweis. Verlag Karl Thieme KG, München, 1st edition, 1964.
- [98] Inc. Burle Technologies. *Channeltron[®] Electron Multiplier Handbook for Mass Spectrometry Applications*, pages <http://www.burle.com/cgi-bin/byteserver.pl/pdf/ChannelBook.pdf> (accessed June 2003). Burle Technologies, Inc., Sturbridge, 2001.

- [99] Foner S. N.; Hudson R. L. Ionization Potential of the *OH* Free Radical by Mass Spectrometry. *J. Chem. Phys.* **1956**, *25*, 602-603.
- [100] Morrison J. D.; Traeger J. C. Ionization and Dissociation by Electron Impact I. *H₂O* and *H₂S*. *Int. J. Mass Spectrom.* **1973**, *11*, 77-88.
- [101] Field F. H.; Franklin J. L. *Electron Impact Phenomena and the Properties of Gaseous Ions* (Ed.: Massey H. S. W.), volume *I* of *Pure and Applied Physics - A Series of Monographs and Textbooks*, chapter II C - Ionization Efficiency Curves, III C - Franck-Condon Principle. Academic Press Inc., New York, 1st edition, 1957.
- [102] Younger S. M. *Electron Impact Ionization* (Ed.: Märk T. D.; Dunn G. H.), chapter 1 - Quantum Theoretical Methods for Calculating Ionization Cross Sections. Springer, Wien, 1st edition, 1985.
- [103] Wigner E. P. On the Behavior of Cross Sections Near Thresholds. *Phys. Rev.* **1948**, *73* (9), 1002-1009.
- [104] Wannier G. H. The Threshold Law for Single Ionization of Atoms or Ions by Electrons. *Phys. Rev.* **1953**, *90* (5), 817-825.
- [105] Donahue J. B.; Gram P. A. M.; Hynes M. V.; et al. Observation of Two-Electron Photoionization of the *H⁻* Ion near Threshold. *Phys. Rev. Lett.* **1982**, *48* (22), 1538-1541.
- [106] Donahue J. B.; Gram P. A. M.; Hynes M. V.; et al. Observation of Two-Electron Photoionization of the *H⁻* Ion near Threshold - Erratum. *Phys. Rev. Lett.* **1984**, *52* (2), 164.
- [107] McGowan J. W.; Clarke E. M. Ionization of *H(1s)* near Threshold. *Phys. Rev.* **1968**, *167* (1), 43-51.
- [108] Moore C. E. *Atomic Energy Levels as Derived from the Analysis of Optical Spectra*, volume *1*. U. S. Gov. Print. Off., Washington D.C., 1949.
- [109] Krige G. J.; Gordon S. M.; Haarhoff P. C. Ionization of Helium Near Threshold by Electron Impact. *Z. Naturforsch.* **1968**, *23a*, 1383-1385.

- [110] Marchand P.; Paquet C.; Marmet P. Threshold Behavior of the Cross Section for Ionization of *He* and *Ar* by Mono-Energetic Electrons. *Phys. Rev.* **1969**, *180* (1), 123-132.
- [111] Lebius H.; Koslowski H. R.; Wiesemann K.; et al. Threshold Behaviour of Electron Impact Ionisation Cross Sections for Rare Gas Atoms. *Ann. Phys.-Leipzig* **1991**, *48*, 103-114.
- [112] Brion C. E.; Thomas G. E. Cross Section for the Production of Singly Ionized Helium by Electron Impact at Low Energies. *Phys. Rev. Lett.* **1967**, *20* (6), 241-243.
- [113] Hickam W. M.; Fox R. E.; Kjeldaas T. Probability Curves Near Threshold for the Formation of He^+ , Ne^{++} , A^{++} , Kr^{++} and Xe^{++} by Electron Impact. *Phys. Rev.* **1954**, *96* (1), 63-65.
- [114] Winkler C.; Märk T. D. Experimental Investigation of the Electron Impact Ionization Cross-Section Behaviour near Threshold. *Int. J. Mass Spectrom.* **1994**, *133*, 157-164.
- [115] Wannier G. H. Threshold Law for Multiple Ionization. *Phys. Rev.* **1955**, *100* (4), 80.
- [116] Geltman S. Theory of Ionization Probability Near Threshold. *Phys. Rev.* **1956**, *102* (1), 171-178.
- [117] Klar H.; Schlecht W. Threshold Multiple Ionization of Atoms. Energy Dependence for Double and Triple Escape. *J. Phys. B - At. Mol. Opt.* **1976**, *9* (10), 1699-1711.
- [118] Grujic P. The Threshold Law for Double Ionisation in Electron-Atom Collisions. *J. Phys. B - At. Mol. Opt.* **1983**, *16* (14), 2567-2576.
- [119] Gerdom K.; Puerta J.; Wiesemann K. State-Selective Study of Ar^{2+} , Ar^{3+} , N_2^{2+} Formation by Electron-Impact Ionization Near Threshold. *J. Phys. B - At. Mol. Opt.* **1994**, *27*, 747-758.
- [120] Morrison J. D.; Nicholson A. J. C. Probability of Double Ionization by Electron Impact for Neon, Argon, and Xenon. *J. Chem. Phys.* **1959**, *31* (5), 1320-1323.

- [121] Gstir B.; Denifl S.; Hanel G. Electron Impact Multiple Ionization of Neon, Argon and Xenon Atoms Close to Threshold: Appearance Energies and Wannier Exponents. *J. Phys. B - At. Mol. Opt.* **2002**, *35*, 2993-3007.
- [122] Winters R. E.; Collins J. H.; Courchene W. L. Resolution of Fine Structure in Ionization-Efficiency Curves. *J. Chem. Phys.* **1966**, *45* (6), 1931-1937.
- [123] Dorman F. H.; Morrison J. D.; Nicholson A. J. C. Threshold Law for the Probability of Excitation by Electron Impact. *J. Chem. Phys.* **1960**, *32* (2), 378-384.
- [124] Dorman F. H.; Morrison J. D.; Nicholson A. J. C. Probability of Multiple Ionization by Electron Impact. *J. Chem. Phys.* **1959**, *31* (5), 1335-1337.
- [125] McDowell C. A. *Mass Spectrometry* (Ed.: McDowell C. A.), chapter 12 - The Ionization and Dissociation of Molecules. McGraw-Hill Series in Advanced Chemistry. McGraw-Hill Book Company, New York, 1st edition, 1963.
- [126] Hagstrum H. D.; Tate J. T. Ionization and Dissociation of Diatomic Molecules by Electron Impact. *Phys. Rev.* **1940**, *59*, 354-370.
- [127] Schaeffer O. A.; Hastings J. M. Isotope Effect on Bond Rupture by Electron Impact on Hydrogen, Deuterium, and Tritium. *J. Chem. Phys.* **1950**, *18* (8), 1048-1050.
- [128] Wigner E.; Witmer E. E. Über die Struktur der zweiatomigen Molekelspektren nach der Quantenmechanik. *Z. Phys.* **1928**, *51*, 859-886.
- [129] McDowell C. A. Adiabatic Correlations for the Formation of Methyl Ions from Methane and its Derivatives by Electron Impact. *T. Faraday Soc.* **1954**, *50*, 423-430.
- [130] Rosenstock H. M.; Wallenstein M. B.; Wahrhaftig A. L.; Eyring H. Absolute Rate Theory for Isolated Systems and the Mass Spectra of Polyatomic Molecules. *P. Natl. Acad. Sci. USA* **1952**, *38*, 667-678.
- [131] Chupka W. A. Effect of Unimolecular Decay Kinetics on the Interpretation of Appearance Potentials. *J. Chem. Phys.* **1959**, *30* (1), 191-211.

- [132] Morrison J. D. Studies of Ionization Efficiency. I. The Determination of Molecular Appearance Potentials Using the Mass Spectrometer. *J. Chem. Phys.* **1951**, *19* (10), 1305-1308.
- [133] Koffel M. B.; Lad R. A. Ionization and Dissociation of Paraffin Hydrocarbons by Electron Bombardment. *J. Chem. Phys.* **1948**, *16* (4), 420-422.
- [134] Honig R. E. Ionization Potentials of Some Hydrocarbon Series. *J. Chem. Phys.* **1948**, *16* (2), 105-112.
- [135] Morrison J. D.; Nicholson A. J. C. Studies of Ionization Efficiency. II. The Ionization Potentials of Some Organic Molecules. *J. Chem. Phys.* **1952**, *20* (6), 1021-1023.
- [136] Smith L. G. Ionization and Dissociation of Polyatomic Molecules by Electron Impact. I. Methane. *Phys. Rev.* **1937**, *51*, 263-275.
- [137] Morrison J. D. Studies of Ionization Efficiency. Part III. The Detection and Interpretation of Fine Structure. *J. Chem. Phys.* **1953**, *21* (10), 1767-1772.
- [138] Wetzel R. C.; Baiocchi F. A.; Hayes T. R.; et al. Absolute Cross Sections for Electron-Impact Ionization of Rare-Gas Atoms by the Fast-Neutral-Beam Method. *Phys. Rev. A* **1987**, *35* (2), 559-577.
- [139] Morrison J. D. On the Optimum Use of Ionization-Efficiency Data. *J. Chem. Phys.* **1963**, *39* (1), 200-207.
- [140] Jansson P. A. *Deconvolution of Images and Spectra*. Academic Press, San Diego, 2nd edition, 1997.
- [141] Eltenton G. C. The Study of Reaction Intermediates by Means of a Mass Spectrometer. *J. Chem. Phys.* **1947**, *15* (7), 455-481.
- [142] Hiden Analytical Limited, 420 Europa Boulevard, Warrington, England. *EPIC and IDP Analysers; Operator's Manual*, Doc.-Nr. HA-085-013 edition, 1998.
- [143] Hiden Analytical Limited, 420 Europa Boulevard, Warrington, England. *MAS-soft User Manual*, Doc.-Nr. HA-085-004 edition, 2000.

- [144] Singh H.; Coburn J. W.; Graves D. B. Mass Spectrometric Detection of Reactive Neutral Species: Beam-to-Background Ratio. *J. Vac. Sci. Technol. A* **1999**, *17* (5), 2447-2455.
- [145] Rego C. A.; Tsang R. S.; May P.W.; et al. Gas-Phase Composition Measurements During Chlorine Assisted Chemical Vapor Deposition of Diamond: A Molecular Beam Mass Spectrometric Study. *J. Appl. Phys.* **1996**, *79* (9), 7264-7273.
- [146] Schwarz-Selinger T.; Dose V.; Jacob W.; et al. Quantification of a Radical Beam Source for Methyl Radicals. *J. Vac. Sci. Technol. A* **2001**, *19* (1), 101-107.
- [147] Trevino C. Analysis for the Catalytic Ignition of Methane in a Stagnation-Point Flow. *AIChE J.* **1999**, *45* (3), 567-573.
- [148] Vesper G.; Ziauddin M.; Schmidt L. D. Ignition in Alkane Oxidation on Noble-Metal Catalysts. *Catal. Today* **1999**, *47*, 219-228.
- [149] Vesper G.; Frauhammer J.; Schmidt L. D.; et al. Catalytic Ignition during Methane Oxidation on Platinum: Experiments and Modeling. *Stud. Surf. Sci. Catal.* **1997**, *109*, 273-284.
- [150] Williams W. R.; Zhao J.; Schmidt L. D. Ignition and Extinction of Surface and Homogeneous Oxidation of NH_3 and CH_4 . *AIChE J.* **1991**, *37* (5), 641-649.
- [151] Cowen M. C.; Allison W. Nonlinearities in Sensitivity of Quadrupole Partial Pressure Analyzers Operating at Higher Gas Pressures. *J. Vac. Sci. Technol. A* **1994**, *12* (1), 228-234.
- [152] Searcy J. Q.; Fenn J. B. Clustering of Water on Hydrated Protons in a Supersonic Free Jet Expansion. *J. Chem. Phys.* **1974**, *61* (12), 5282-5288.
- [153] Shinohara H.; Nishi N. Photoionization of Water Clusters at 11.83 eV: Observation of Unprotonated Cluster Ions ($H_2O_n^+$) ($2 \leq n \leq 10$). *J. Chem. Phys.* **1986**, *84* (10), 5561-5567.
- [154] Lossing F. P.; Semeluk G. P. Free Radicals by Mass Spectrometry. XLII. Ionization Potentials and Ionic Heats of Formation for $C_1 - C_4$ Alkyl Radicals. *Can. J. Chemistry* **1970**, *48*, 955-965.

- [155] Plessis P.; Marmet P.; Dutil R. Ionization and Appearance Potentials of CH_4 by Electron Impact. *J. Phys. B* **1983**, *16* (7), 1283-1294.
- [156] Nutt C. W.; Kapur S. Mechanism of Oxidation of Ammonia on Platinum. *Nature* **1968**, *220*, 697-698.
- [157] Rebrov E. V.; de Croon M. H. J. M.; Schouten J. C. Development of the Kinetic Model of Platinum Catalyzed Ammonia Oxidation in a Microreactor. *Chem. Eng. J.* **2002**, *90*, 61-76.
- [158] Pignet T.; Schmidt L. D. Kinetics of NH_3 Oxidation on *Pt*, *Rh*, and *Pd*. *J. Catal.* **1975**, *48*, 212-225.
- [159] Locht R.; Servais Ch.; Ligot M.; et al. The Dissociative Electroionization of Ammonia and Ammonia- d_3 . I. The NH^+ and NH_2^+ Dissociation Channels. *Chem. Phys.* **1988**, *123*, 443-454.
- [160] Foner S. N.; Hudson R. L. Mass Spectrometry of Free Radicals and Vibronically Excited Molecules Produced by Pulsed Electrical Discharges. *J. Chem. Phys.* **1966**, *45* (1), 40-48.
- [161] Foner S. N.; Hudson R. L. Mass Spectrometric Studies of Metastable Nitrogen Atoms and Molecules in Active Nitrogen. *J. Chem. Phys.* **1962**, *37* (8), 1662-1667.
- [162] Reed R. I.; Snedden W. The Ionization Potential of NH . *J. Chem. Soc.* **1959**, 4132-4133.
- [163] Locht R.; Schopman J.; Wankenne H.; et al. The Dissociative Ionization of Nitrogen. *Chem. Phys.* **1975**, *7*, 393-404.
- [164] Manner R.; Sperka G.; Witzel M. Weiterentwicklung des BMA-Verfahrens. *Stets geforscht: Chemieforschung im Degussa-Forschungszentrum Wolfgang* **1988**, *2*, 7-14.
- [165] National Institute of Standards and Technology. *NIST Chemistry Webbook*, chapter NIST Standard Reference Database 69, page <http://webbook.nist.gov/chemistry> (accessed august 2003). U. S. Commerce Department's Technology Administration, 2003.

- [166] Kusch P.; Hustrulid A.; Tate J. T. The Dissociation of HCN , C_2H_2 , C_2N_2 and C_2H_4 by Electron Impact. *Phys. Rev.* **1937**, *52*, 843-854.
- [167] Frost D. C.; Lee S. T.; McDowell C. A.; et al. A Versatile Fast Pumping Ultraviolet Photoelectron Spectrometer for the Study of Transient and Unstable Species. *J. Electron. Spectrosc.* **1977**, *12*, 95-109.
- [168] Lossing F. P.; Lam Y-T.; Maccoll A. Gas Phase Heats of Formation of Alkyl Immonium Ions. *Can. J. Chemistry* **1981**, *59*, 2228-2231.
- [169] Harland P. W.; McIntosh B. J. Enthalpies of Formation for the Isomeric Ions H_xCCN^+ and H_xCNC^+ by 'Monochromatic' Electron Impact on C_2N_2 , CH_3CN and CH_3NC . *Int. J. Mass Spectrom.* **1985**, *67*, 29-46.
- [170] Flesch G. D.; Svec H. J. Fragmentation Reactions in the Mass Spectrometer for $C_2 - C_5$ Alkanes. *J. Chem. Soc. Farad. T. 2* **1973**, *69*, 1187-1199.
- [171] Plessis P.; Marmet P. Electroionization Study of Ethane: Ionization and Appearance Energies, Ion-Pair Formations and Negative Ions. *Can. J. Chemistry* **1987**, *65*, 1424-1432.
- [172] Williams J. M.; Hamill W. H. Ionization Potentials of Molecules and Free Radicals and Appearance Potentials by Electron Impact in the Mass Spectrometer. *J. Chem. Phys.* **1968**, *49* (10), 4467-4477.
- [173] Stephan K.; Märk T. D.; Futrell J. H.; et. al. Electron Impact Ionization of $(N_2)_2$: Appearance Energies of N_3^+ and N_4^+ . *J. Chem. Phys.* **1984**, *80* (7), 3185-3188.
- [174] Peel J. B.; Willett G. D. Photoelectron Spectrum of Methylenimine by Spectrum Stripping. *J. Chem. Soc. Farad. T. 2* **1975**, *71*, 1799-1804.
- [175] Wedler G. *Lehrbuch der Physikalischen Chemie*, chapter 5 - Transporterscheinungen. Wiley VCH, Weinheim, 4th edition, 1997.

I express my gratitude to ...

- .. the Fonds der Chemischen Industrie for the financial support by awarding the Kekulé scholarship for the period from 01.09.2000 to 31.08.2002
- .. Prof. Dr. Robert Schlögl for giving me the opportunity to prepare this work in an excellent scientific surrounding
- .. Prof. Dr. Reinhard Schomäcker for taking over the second opinion
- .. Prof. Dr. Christoph van Wüllen for taking the chair of the examination board
- .. Dr. Gerhard Mestl who had the original idea to apply threshold ionization mass spectrometry to heterogeneously catalyzed reactions and advised me during the first half of this work
- .. Dr. Friederike Jentoft for her supervision during the second half of this work, her helpful discussions and the revision of the manuscript
- .. Manfred Thiede for his engineering support with the experimental setup
- .. Klaus Ihmann for his creativity in the realization of the new apparatus and for the three-dimensional drawings shown in Part III of this work
- .. Philipp Martin Schmidt for his excellent work as a student trainee
- .. Ute Wild for keeping me in form by our jogging sessions in the lunch break
- .. all other colleagues in the Department of Inorganic Chemistry and the staff members of the different service groups at the Fritz-Haber-Institute of the Max-Planck-Society
- .. my parents Irmgard and Herbert and my sister Sigrun for their ongoing support and motivation

Curriculum Vitae

Personal Data

Name: Raimund Horn
Date of Birth: July 9, 1976
Place of Birth: Schmalkalden, Thüringen, Germany
Nationality: German
Parents: Irmgard and Herbert Horn

School

1983-1991: Polytechnische Oberschule
‘Dr. Theodor Neubauer’ Brotterode
1991-1993: Staatliches Gymnasium Schmalkalden
1993-1995: Goethe-Gymnasium Ilmenau
1995: Abitur

University

1995-2000: Study of Chemistry at the Friedrich-Schiller-Universität Jena
Intermediate exam in October 1997
Final exam for degree ‘Diplom-Chemiker’ in August 2000
Thesis in Analytical Chemistry under the supervision of
Prof. Dr. Klaus Danzer
Title: “Kopplung einer elektrothermischen Verdampfungseinheit
mit einem ICP-Massenspektrometer
zur Verbesserung der Nachweisgrenze und der Spezifität”

since September 2000: Ph.D. student at the Department of Inorganic Chemistry,
Fritz-Haber-Institute of the Max-Planck-Society in Berlin,
under the supervision of Prof. Dr. Robert Schlögl

Grants

09/00-08/02: Kekulé scholarship of the Stipendienfonds
des Verbandes der Chemischen Industrie